THE UNIVERSITY *of* EDINBURGH

AC Susceptibility Studies under Hydrostatic Pressure

Duncan Michael McCann

Doctor of Philosophy
The University of Edinburgh
September 2016

Abstract

AC susceptibility is an important characterisation technique measuring the time dependent magnetisation and dynamics of a magnetic system. It is capable of yielding information on thermodynamic phase transitions, relaxation processes and losses in a variety of interesting magnetic and superconducting materials. In particular it is a powerful probe of the mixed state of superconductivity providing insight into the flux dynamics at play and determination of a number of physical properties such as the critical temperature T_c, field H_c and characteristic length scales.

Application of pressure can tune materials through multiple phases and interesting phenomena. The thesis describes the design of a calibratable susceptometer in a piston cylinder pressure cell, achieving AC susceptibility measurements of the same accuracy as a SQUID magnetometer but under pressure. This is used to make measurements on an electrostatically doped capacitance device, a single chain magnet and a heavy fermion superconductor. These studies are summarised below.

Electric double layer (EDL) devices provide a means of continuous tuning through a materials phase diagram by applying an electric field, including inducing superconductivity. Application of pressure in tandem with electrostatic doping could improve the efficiency of these devices and provide a second tuning parameter. An EDL capacitor was constructed and measured with the above susceptometer aiming to shift the T_c of a doped high temperature superconducting cuprate $La_{1.9}Sr_{0.1}CuO_4$. The T_c shifts proved irreproducible already at ambient conditions. Indeed during the course of this research further experimental evidence emerged in the literature indicating EDL devices may very well work due to electrochemical doping rather than electrostatic, possibly accounting for the lack of repeatability. Work therefore focused on mapping the ionic liquid DEME-TFSI's glass-liquid phase diagram over the 1 GPa pressure range, rather

than extending the study of the EDLC device to high pressure.

Single chain magnets (SCM) are an interesting class of material consisting of a one-dimensional molecular magnet chain manifesting magnetic hysteresis and slow relaxation best characterised by AC susceptibility. The susceptometer was used to study the SCM $[Co(NCS)_2(pyridine)_2]_n$ to investigate the effect of pressure on its characteristic magnetic relaxation time and energy barrier. A secondary signal appears at ∼0.44 GPa which is attributed to the development of an additional structural phase that has been independently observed in X-ray crystallographic measurements.

The heavy fermion superconductor U_6Fe has the highest T_c ∼4 K of all the U-based compounds and large critical fields of ∼10-12.5 T, depending on direction, which increase on initial application of pressure. It exhibits a coexisting charge density wave (CDW) below 10 K making it a promising candidate for the modulated superconductivity of the theorised Fulde-Ferrel-Larkin-Ovchinnikov (FFLO) state. A feature at 110 K is also evident in Mössbauer, resistivity and specific heat measurements, the origin of which has not yet been clearly identified. Evidence for the FFLO state was sought by mapping the upper critical field H_{c2} along with the peak effect through AC susceptibility measurements up to pressures of 1 GPa. The data is accounted for by an evolution of collective pinning and superconducting parameters, with no clear evidence for an FFLO state although an enhancement of the reduced field is observed.

Lay Summary

Materials subjected to high pressures and low temperatures often display exotic behaviour and properties which can be useful in a variety of applications. A common tool for identifying and yielding information on such emergent behaviour is the measurement of a material's response to a time varying magnetic field, known as alternating current (AC) susceptibility. However if a sample is under pressure inside a piston cylinder cell it is often difficult to separate its response from the cells. Thus in this thesis we detail the design of coils for insertion into such cells capable of measuring a material's AC susceptibility with minimal signal from the cell.

In $[Co(NCS)_2(pyridine)_2]_n$ molecules connected in a chain are capable of aligning their magnetic response with an applied field, however in absence of this field the alignment is lost over a certain relaxation time. Such behaviour is investigated under pressure with AC susceptibility yet does not appear to improve for this particular compound. An additional response is detected however which is attributed to development of an alternate configuration of the compound confirmed by independent measurements. In U_6Fe all of the magnetic field is expelled from the sample below a certain temperature T_c in what is known as superconductivity. Development of this behaviour is investigated with AC susceptibility under pressure to determine if it exhibits a theorised state where field expulsion varies across the sample. No clear evidence for this is found.

Subjecting materials to large electric fields provides a further method for inducing exotic behaviour especially when coupled with pressure. Implementing our coils in devices capable of applying large electric fields allowed detection of the altered superconducting T_c in $La_{1.9}Sr_{0.1}CuO_4$. However due to lack of repeatable results we were unable to investigate whether pressure improved this effect. Such devices rely on a liquid of charged molecules in order to operate, thus to ensure their potential use under pressure the freezing temperature of this liquid is determined.

Declaration

I declare that this thesis was composed by myself, that the work contained herein is my own except where explicitly stated otherwise in the text, and that this work has not been submitted for any other degree or professional qualification except as specified.

Parts of this work have been published in [1].

(*Duncan Michael McCann, September 2016*)

Acknowledgements

First and foremost, I would like to thank my principal supervisor Andrew Huxley for his support throughout my PhD. In particular his guidance, experimental expertise and discussions regarding superconductivity. I would also like to thank my second supervisor Konstantin Kamenev for his technical expertise and assistance with all pressure related experimental work.

Furthermore I would like to thank William Whitley, Jean-Phillipe Reid, Julian Schmehr and Chris O'Neill for all their assistance in experimental and computational work. In particular I would like to thank Michal Kepa and Oliver Entwisle for all their advice, help in the lab and many discussions on all manner of topics. Completion of this project would not have been possible without the help of; Martin Misek, for assistance in pressure experiments; Angel Lopez, for sample synthesis and characterisation advice; Andrew Downie, for engineering and equipment design; Xiao Wang, for design and assistance with high pressure cells; and Chris Woodall, for pressure cell work and material discussions. Additionally, I would like to thank Gavin Craig and the Murrie Group from the University of Glasgow for provision of the single chain magnet sample and discussions of experimental results.

I would also like to thank all of my friends and colleagues for their support, reassurance and all the fun throughout the years. In particular my office mates Charlotte de Grouchy, Martin Gorman, Mary-Ellen Donnelly, Keith Munro, Veronika Afonina and Amy Coleman.

Finally I would like to thank my parents and brother for all their love and support over the years which helped make me the person I am today. And most importantly my wife Melanie who has always been there for me throughout this project providing love, support and encouragement, especially during the difficult times.

Contents

List of Figures

List of Tables

Chapter 1

Introduction & Background

1.1 Introduction

AC susceptibility measures the magnetisation of a material in response to a time varying magnetic field, and as such it is capable of yielding information on the dynamic behaviour within magnetic systems. Indeed, measurement of the time dependent magnetisation allows determination of the relaxation times for magnetic moments, onset of thermodynamic phase transitions and losses in a wide variety of materials[2, 3]. In particular it provides an indication of the flux behaviour and physical properties of superconducting materials[4].

Superconductivity is a fascinating phenomenon of completely zero electrical resistance exhibited by several materials when cooled below a certain critical temperature T_c. The precise mechanism of superconductivity remained a great mystery since its discovery by Onnes' in 1911[5] until Bardeen, Cooper, and Schrieffer published their theory of superconductivity in 1957, which accurately predicted experimental observations[6]. BCS theory, as it was termed, described how electrons exchanged momenta by coupling via phonons within the crystal lattice to form Cooper pairs. These Cooper pairs, being comprised of two fermions, were bosons and so no longer obeyed the Pauli exclusion principle; thus enabling them to condense into a single macroscopic coherent state allowing for zero resistance conduction across a sample[5]. Superconductors are also characterised by the Meissner effect where they expel all magnetic fields and exhibit perfect diamagnetism; magnetised perfectly in opposition to an applied

field[7]. While a fascinating phenomenon, the critical operating temperatures for superconductivity were very low thus limiting their use to specialised and difficult experimental setups. It was not until the discovery of superconductivity in ceramics in 1986 by Bednorz and Müller[8] which exceeded theoretical limits that widespread applications for superconductivity became a feasible goal. As superconducting materials conduct with zero resistance they have many promising applications. They are capable of carrying large currents and can generate powerful magnetic fields for use in particle accelerators, material characterisation equipment, Maglev trains and medical scanning devices such as MRI machines. Although most importantly superconductors could revolutionise the energy industry. The chief losses in power generation and transmission are due to the resistive heating in wires as they carry current. As superconductors exhibit zero resistance conduction, they are capable of completely removing these losses and increasing the efficiency and yield of power generation and transmission. Widespread application of superconductivity in energy technologies would help to combat the impending global energy crisis as consumption continues to rise.

In order to allow for extensive application of such technologies, much research has been conducted over the past several decades towards understanding and improving these new high temperature superconductors as well as other novel examples such as heavy fermion superconductors. BCS theory does not adequately explain nor predict such unconventional superconductivity and thus much work has been conducted in an effort to formulate a full theory describing them. While much progress has been made to date there is still no universally accepted theory on the precise mechanism behind their behaviour, although our understanding has greatly improved. Superconductors with much higher critical temperatures have been discovered and can be further improved by either chemical doping to increase the concentration of charge carriers[9, 10], or subjecting them to high pressures to alter their electronic structure[7]. These two methods effectively allow the superconducting state to form more readily at higher temperatures. Doping however, while generally the most common method, is not readily possible for certain materials and also introduces structural disorder complicating the physical phenomenon[9, 11]. It is possible to entirely avoid these issues by instead utilising electrostatic doping; increasing the charge carrier density by application of extremely strong electric fields. Electrostatic doping has been shown to induce superconductivity in thin films as early as 1960[12]. Initially this was implemented using field effect transistors (FET) yet has been limited due to charge recombination as a result of dielectric breakdown[9, 13, 14].

A more effective method involves the electric double layer (EDL) arrangement wherein there exists an interface between the charged material in question and an electrolyte dielectric. An electrolytic dielectric is less susceptible to breakdown from sustained charge recombination at the interface due to mobility of the ions[13]. A double layer of oppositely charged carriers are arrayed either side of such an interface, creating a capacitor with nanometre separation and hence an extremely large electric field. Such an arrangement can increase the carrier density sufficiently to induce superconductivity[13].

In recent years more success has been had with electric double layer capacitor (EDLC) and transistor (EDLT) arrangements. An EDLC is comprised of a capacitor with one electrode of the material in question and an electrolyte as the dielectric; application of a voltage forms EDLs at the electrodes and can induce superconductivity. An EDLT is based on the same principle yet the electrode of interest has a source and drain patterned onto it. Such a setup has been shown to induce superconductivity in $SrTiO_3$ at temperatures comparable to the maximum value achieved through chemical doping[9]. Further improvements by substituting electrolyte dielectrics for ionic liquids allows for stronger electric fields to be created at the EDL interface and hence a greater chance for superconductivity to arise. Ionic liquid EDL arrangements have been shown to induce superconductivity in ZrNCl[15, 16] and also in $KTaO_3$, a material which exhibited no superconducting behaviour previously under chemical doping[11]. EDL arrangements are thus potentially capable of inducing superconductivity in a variety of materials far more easily than by chemical doping. Not only this, but without the usual corresponding structural disorder the fundamental mechanism behind the superconductivity will likely be easier to discern. The efficiency and operating conditions of many superconductors, particularly high temperature superconductors, could likely be improved utilising these arrangements; as well as providing an electrically controlled switch between insulating/superconducting behaviour.

EDLC devices detect the perfect diamagnetism associated with superconductivity through AC susceptibility measurements, by utilising mutual induction of a two-coil susceptometer. Detection of this diamagnetic onset enables tracking of altered superconducting behaviour due to electrostatic doping. Such susceptometers also enable similar AC susceptibility measurements to further probe superconductivity behaviour, as well as additional magnetic phenomena, in a number of systems.

1.2 Superconductivity

After Onnes' initial discovery of superconductivity in Mercury in 1911[5] investigation into this phenomenon over the years unearthed its occurrence in many other elements and alloys. The culmination of this research led to the renowned BCS theory which accurately predicted experimental observations[6] and determined the mechanism for superconductivity.

Superconductivity arises in these materials due to Cooper pairs forming via electron-phonon coupling and condensing into a single macroscopic quantum state across the sample[5]. Thus for many years the field of study focused primarily on certain theoretical eccentricities and interesting examples of superconductivity. Yet the discovery of superconductivity in a ceramic material in 1986[8] signalled the advent of high temperature superconductivity. BCS theory did not adequately explain nor predict this form of superconductivity; ceramic materials were not obvious superconductors under it, transition temperatures were higher than the theoretical limit and the pairing mechanism could not be identified[10]. Such a revelation led to a flurry of activity over the years to further explore high temperature superconductivity and determine a comprehensive theory behind this phenomenon. Over the decades many more examples of superconducting ceramics have been discovered and much progress has been made towards its theoretical development, yet several issues still remain unresolved. So far no universally accepted theory of superconductivity has been formulated, and the pairing mechanism remains unidentified. Thus, it remains difficult to predict which materials will exhibit superconductivity. Indeed novel forms of superconductivity are continually being discovered, such as heavy fermion superconductors[7] and more recently the FeAs/FeSe class of high T_c superconductors[10]. Whilst a fully conclusive theory has yet to emerge, research into this area has helped to improve known superconductors and their operating conditions. For the race is not only to uncover the theory behind unconventional superconductors but also develop them to the point where they are capable of being employed effectively and economically in a range of technological applications. Superconductivity research has led to improvements in the synthesis of high-purity defect free wire, increases in T_c, maximisation of the current density J_c which can flow through them and the limiting fields H_c they can operate in[10].

The high T_c cuprate superconductors in particular have been improved significantly over the years ever since the first member of this family was discovered

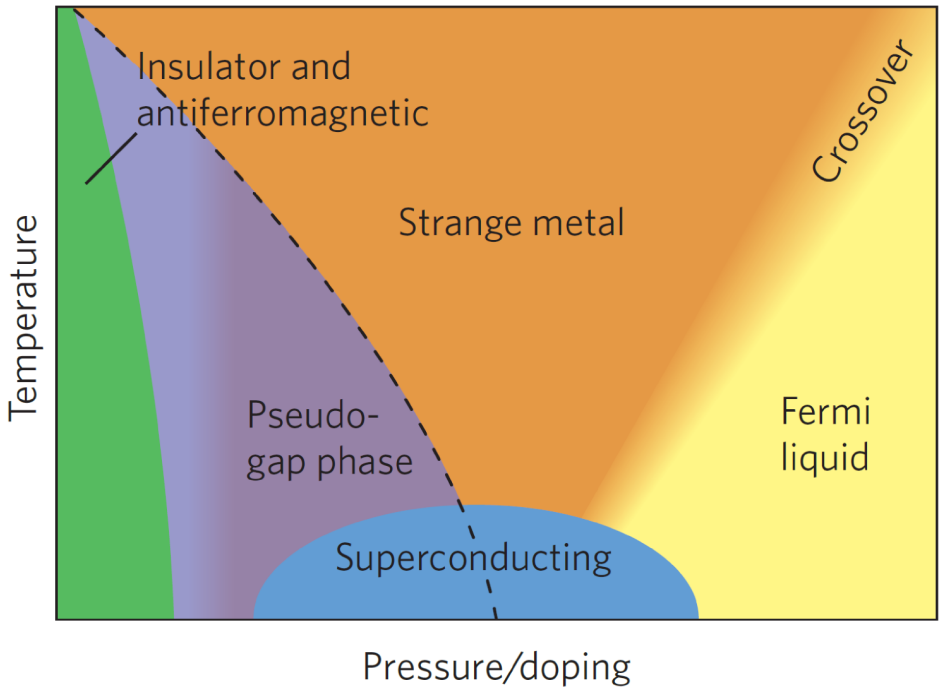

Figure 1.1 *General phase diagram for cuprate superconductors indicating superconductivity can be induced from the insulating parent compound either through pressure or doping[10].*

by Bednorz and Müller[8]. Such heavy investigation into them has resulted in discovery of many more compounds in this family with much higher T_c's and are thus among the most likely candidates for practical applications. Cuprates in general have a perovskite crystal structure with layered copper-oxide planes in which the superconductivity arises[17]. The parent compound is an antiferromagnetic, Mott insulator which itself does not exhibit superconductivity, yet this can be induced either by chemical doping or through the application of pressure as seen in Figure 1.1. Substitutional doping involves altering the conductivity of an insulator by replacing atoms with those of a different valency, whereas interstitial doping inserts these into vacancies within the structure. Such doping alters the carrier density within the copper oxide layers sufficiently to suppress the antiferromagnetism and induce superconductivity[7, 10, 17]. Pressure can similarly induce such phase transitions by altering the materials lattice and its electronic structure[7, 13]. Figure 1.1 illustrates how by utilising either of these methods we may tune a material to a point where T_c is maximum and hence superconductivity most easily attainable experimentally.

Doping is often the most common method for creating superconducting materials as it does not require any equipment to maintain such a state unlike the pressure method. However there are associated complications with chemical doping of a

compound. Certain materials exhibit a lack of chemical solubility and so are incapable of being doped to any large degree, thus precluding this method of increasing their carrier density[11]. Even if a material does not suffer from such a doping insolubility it is still difficult to ensure the precise doping concentration desired has been achieved from any given manufacturing process. Not only this, but doping by its very nature is liable to distort the crystal structure itself and introduce disorder. Such distortions can introduce complications to the physics occurring in a material and obscure accurate determination of the desired superconducting mechanism[9, 11]. Superconductivity also relies on homogeneous crystalline structures and can very easily be disrupted or destroyed completely by defects. Attempting to chemically dope any significant amount of material runs the risk of inhomogeneities occurring and increases the chances of disruption to the superconducting state. It is for this reason that large-scale fabrication of superconductor wire for practical applications is such a difficulty as high quality, expensive manufacturing is necessary to help minimise such defects. Thus, whilst doping is among the most achievable methods for inducing superconductivity in such materials, it is a difficult process and has several drawbacks.

1.2.1 Type I and II Superconductivity

Superconductivity can generally be classified into two distinct types, I & II. A type I superconductor cooled below T_c and in fields less than the critical field H_c expels all magnetic flux from the bulk in what is known as the Meissner effect. The Meissner effect occurs where persistent screening currents form within a characteristic penetration depth, λ, of the superconductor surface to expel flux and thus exhibit perfect diamagnetism. The Meissner effect distinguishes superconductors from perfect conductors in that it is independent of a material's magnetic history and is thus a true thermodynamic state[18]. As shown in Figure 1.2 (a) if an applied field is increased above a certain value known as the critical field H_c the superconductivity is quenched and full flux penetration occurs in the normal state. At the critical field the difference between the normal and superconducting state free energy is exceeded and thus the normal state is more energetically favourable where[19]

$$\Delta F_{NS} = \mu_0 \frac{H_c(T)^2}{2} \tag{1.1}$$

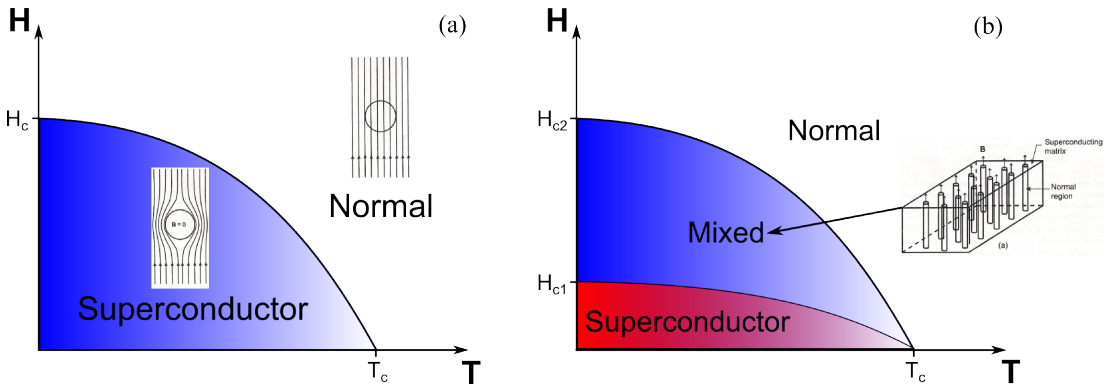

Figure 1.2 *Temperature-field phase diagrams for (a) Type I and (b) Type II superconductors illustrating relative critical fields. Insets illustrate flux behaviour within all three distinct states[18].*

Type II superconductors however only expel all magnetic flux with the Meissner effect up to a lower critical field H_{c1}, above which there is partial permeation of flux into the sample in what is known as the mixed state. In the mixed state filaments of quantised flux thread the sample, allowing the magnetic field to penetrate through as shown in Figure 1.2 (b). These filaments, known as Abrikosov vortices, are regions of normal state within the superconductor maintained by a vortex of persistent current flowing around them. Such a mixed state arises in type II superconductors as it is more energetically favourable to have multiple normal/superconducting state boundaries as opposed to full flux exclusion. A type II superconductor still exhibits zero resistance through the superconducting state and diamagnetism, although reduced from the full exclusion case. At an upper critical field H_{c2} this lattice of quantised vortices overlap and the superconducting state is entirely suppressed as full flux penetration occurs[17]. The upper critical field can thus be characterised by the flux density such that

$$\mu_0 H_{c2} = \frac{\phi_0}{2\pi\xi^2} \tag{1.2}$$

where μ_0 is the vacuum permeability, ϕ_0 is one quantum of flux and ξ is the superconducting coherence length, the effective size of a vortex core. This value of H_{c2} is known as the orbital limit and can also be determined from the slope of critical field curves in the vicinity of T_c using

$$H_{c2} = -C \left.\frac{dH_{c2}}{dT}\right|_{T_c} T_c \tag{1.3}$$

Where C is a parameter determined by the scattering length in a material, which may be taken in either the clean or dirty limit of BCS superconductivity. In a clean superconductor the scattering mean free path is much greater than ξ

and much less in the dirty limit[20]. If the field dependence of the normal state is considered however the value of H_{c2} is reduced even further, due to Pauli paramagnetic effects lowering the normal state energy. The corresponding Pauli limiting field, utilising BCS parameters, is given by[21]

$$H_{c2}^{P} = 1.24\frac{k_B T_c}{\mu_B} \tag{1.4}$$

Where k_B is the Boltzmann constant and μ_B the Bohr magneton. The relative size of the orbital and Pauli limiting fields can be used to determine which effect is dominant through use of the Maki parameter $\alpha_M = \sqrt{2}H_{c2}/H_{c2}^{P}$. A Maki parameter greater than one indicates a material in the Pauli limit[22].

1.3 Electrostatic Doping

Electrostatic doping provides the means to investigate superconductivity in materials without the complications associated with chemical doping. Strong electric fields are used to increase the charge carrier concentration to a point where superconductivity arises[13] and has been exhibited in thin film interfaces as early as 1960[12]. Utilising this technique it is possible to accurately tune along a materials phase diagram and hence control the onset of superconductivity without altering the structure itself[23].

1.3.1 Field Effect Transistors

Initially electrostatic doping was primarily carried out using a field effect transistor (FET). Figure 1.3 illustrates how in FETs an external electric field is applied through the gate electrode which accumulates charge either side of a dielectric. The thin charge layer forming along the surface of the oxide channel in general alters the conductivity between the source and drain contacts. Thus, using this same field effect, it is possible to form a two-dimensional electron gas with sufficient charge carrier density to induce superconductivity in the oxide channel[24]. FET arrangements such as this are even capable of altering the onset T_c in high temperature superconducting cuprates[23].

However FETs have proven somewhat limited in their ability to electrostatically dope materials. As the gate voltage is ramped up the electric field increases

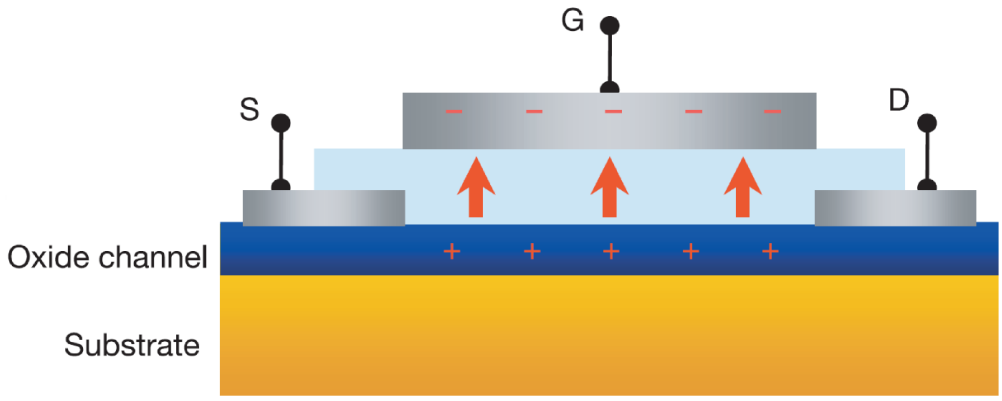

Figure 1.3 *Schematic of generic FET illustrating charge build up either side of dielectric due to the electric field from an applied gate (G) voltage. Charge accumulation in the oxide layer affects the conductivity measured between the source (S) and drain (D) contacts[23].*

along with it until the dielectric breaks down. At this point it ceases to act solely as a dielectric and allows charge recombination to occur at the interfaces, thus preventing any further charges from accumulating. Given the conventional gate dielectrics of SiO_2 or Al_2O_3, breakdown electric fields are seldom much greater than 1 MV cm^{-1}[11, 13], corresponding to a limiting carrier density of 10^{13} cm^{-2} which is not necessarily sufficient for inducing or maximising superconductivity[9, 14, 25]. Thus conventional FETs have primarily allowed tuning of the T_c in many already chemically doped materials rather than inducing superconductivity itself[25]. Yet this limiting breakdown voltage of conventional FETs has been improved on through use of the electric double layer concept. Several different arrangements utilising the electric double layer have been implemented over the years with the ability to induce superconductivity in materials to the same degree as chemical doping[9], and even in those which have previously exhibited none before[11].

1.3.2 Electric Double Layer

The electric double layer (EDL) is a concept considered as early as 1947[26] yet has only been employed in more recent years due to the sufficient development of manufacturing processes. An EDL consists of an interface between a conducting material and an electrolyte where a layer of charges accumulates at the material surface, while a corresponding layer of ions organises within the electrolyte. The layers are arrayed either side of the interface and thus form a capacitor with nanometre separation and hence an extremely large electric field. Such

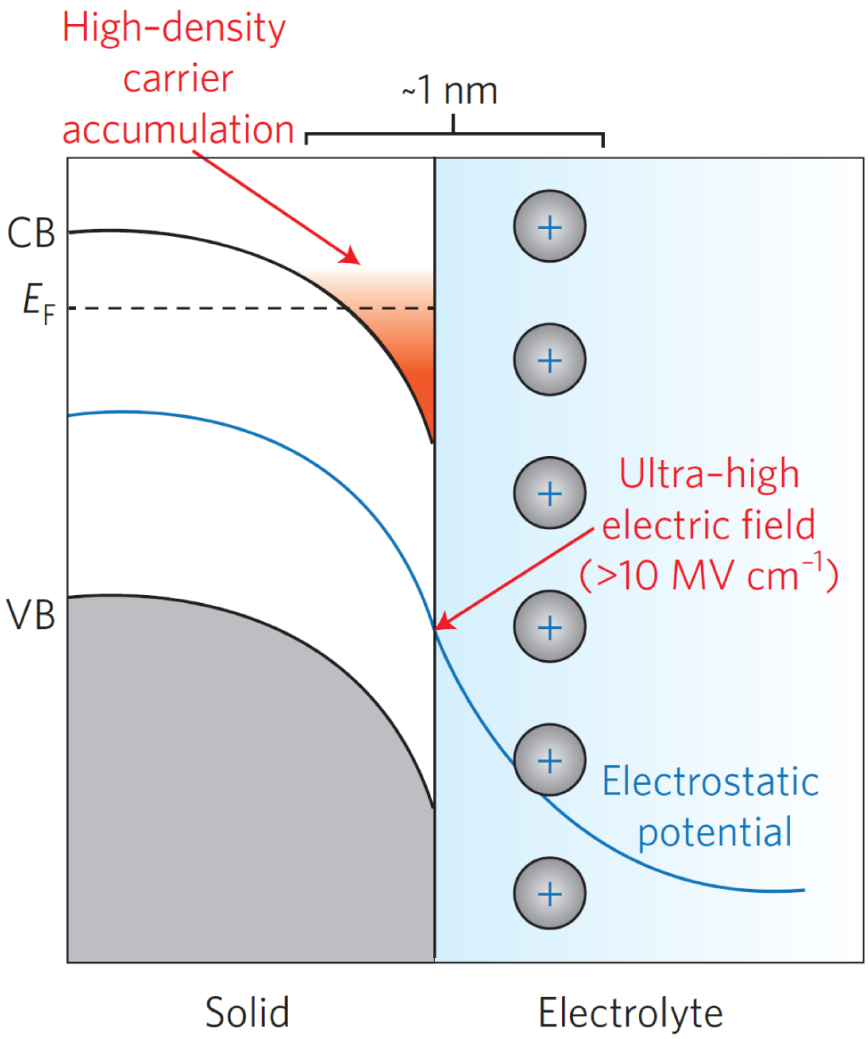

Figure 1.4 *EDL formed between a semiconductor and electrolyte illustrating how the high electric field created bends the valence (VB) and conduction bands (CB) allowing for high density carrier accumulation near the interface[13].*

an arrangement is resistant to dielectric breakdown due to the fact that even if charges do recombine at the interface more ions from the electrolyte are capable of replacing them. Thus EDL devices are capable of sustaining higher electric fields than conventional FETs[9, 11].

Figure 1.4 illustrates how the high electric fields created at the interface bend the valence and conduction bands of a semiconductor (or insulator) thus allowing for carriers to easily promote themselves. The high carrier density formed near the interface gives rise to a 2D electron gas which can induce a superconducting state[13, 24]. Of course atomically flat surfaces are required in order for the necessary EDL to form, hence why these arrangements are only being implemented now with the advanced manufacturing processes available[13].

1.3.3 Electric Double Layer Transistors

EDLs have been implemented in electric double layer transistor (EDLT) devices where the gate dielectric of a conventional FET, such as in Figure 1.3, is replaced by an electrolyte. As voltage is applied to the gate electrode, charged particles within the electrolyte move to align along this plate; thereby accumulating oppositely charged electrolyte particles at the oxide channel, which draws charge carriers to its surface. Thus EDLs are formed at each interface as can be seen in Figure 1.5.

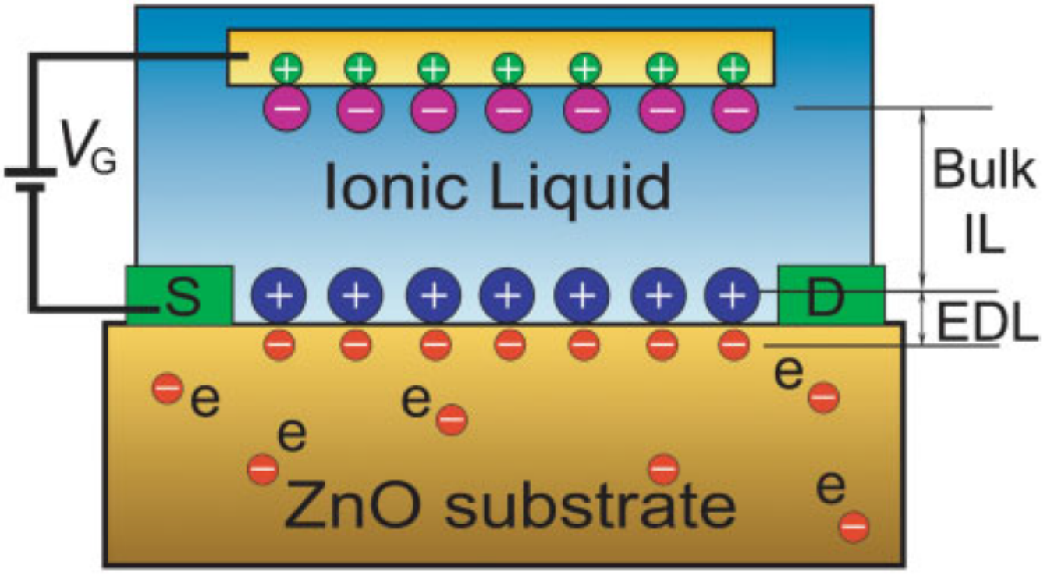

Figure 1.5 *An EDLT arrangement illustrating charge accumulation from the applied gate voltage forming EDLs at each interface and thus increasing the charge carrier density at the surface of the ZnO substrate[25].*

The primary means for determining if there is an onset of superconductivity in EDLTs are resistance measurements of the oxide channels. In general a gate voltage is applied and the resistance measured as the device is cooled in order to monitor its conductivity. A sudden drop in resistance to zero would indicate the onset of superconductivity for the corresponding gate voltage. Dhoot and Panzer were able use such EDLT devices with polymer electrolytes to increase carrier densities in polymer films as high as 10^{15} cm^{-2} and induce metallic conductivity[27, 28]. Shimotani then illustrated how an EDLT device could raise the carrier density sufficiently high to induce a metal transition in an insulating ZnO single crystalline film[29]. Whilst metal-insulator transitions are indeed useful, it was the prospect of inducing superconductivity in oxides with EDLTs which was most alluring. Thus Ueno focused on creating an EDLT with $SrTiO_3$, a

material which required relatively low carrier density to induce superconductivity when chemically doped. Conventional FETs had failed to raise the carrier density high enough in $SrTiO_3$, yet when implemented in the EDLT arrangement Ueno not only achieved field induced superconductivity but also to the same degree capable through optimal chemical doping[9].

Thus superconductivity can be brought about in undoped materials with EDLT devices. However, $SrTiO_3$ only required a relatively low density to exhibit superconductivity; thus the ability to raise carrier density would need to be improved for these devices to be of use with other materials. There are also potential issues of irreversible chemical reactions between electrolytes and some oxide materials, degrading them to the point where the device is irreparably compromised[25]. These issues were jointly dealt with by replacing the electrolyte in EDLTs with an ionic liquid, a highly polar binary salt with a low melting point. Ionic liquids exhibit higher dielectric constants than most electrolytes and are chemically compatible with many materials, making them less likely to suffer from degradation[30]. Yuan illustrated how ionic liquids can allow higher carrier densities to be achieved in ZnO films with EDLTs[25] than other dielectrics as seen in Figure 1.6[13]. Ye was among the first to use an ionic liquid gated EDLT to electrostatically dope ZrNCl films, a parent phase for superconductors, inducing superconductivity and maximising their T_c[15]. Yet the true power of these enhanced EDLTs was illustrated when Ueno managed to induce superconductivity in $KTaO_3$, a material that had never previously exhibited it[11]. $KTaO_3$ has a low chemical solubility and so is unable to be chemically doped in order to raise its carrier density sufficiently to superconduct.

Ueno's success in raising the carrier density through electrostatic doping has opened a world of possibilities for superconductivity. Entirely new superconductors, whose parent compounds are resistant to chemical doping, could be discovered by employing these new EDLT arrangements; superconductors which could potentially have greater beneficial properties for applications than existing ones. Indeed Bollinger has already used ionic liquid gated EDLTs with one of the high temperature superconducting cuprates, $La_{2-x}Sr_xCuO_4$, to alter its T_c by up to 30 K[31]. Not only this, but cleaner superconducting phases can also be established in materials without structural disorder allowing for better understanding of the fundamental physics underlying the phenomena. Of course in all of these devices, for an effective EDL to form it is necessary to have atomically thin oxide layers with appropriate contacts for the EDLT patterned

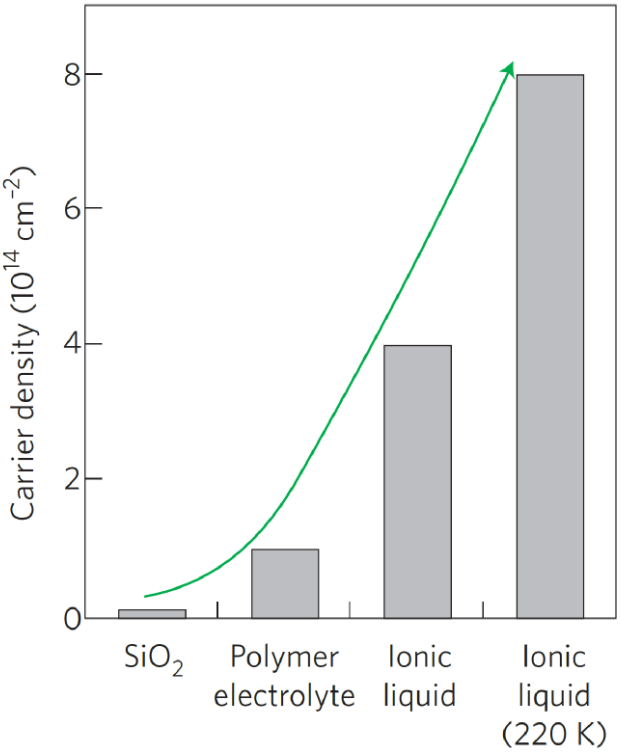

Figure 1.6 *Carrier densities achieved in transistor devices with solid SiO_2, polymer electrolyte and ionic liquid dielectrics. Ionic liquid performance can be further improved by lowering the temperature of the device[13].*

onto them; generally high-quality thin films[27–29] or individual single crystal flakes[15].

1.3.4 Electric Double Layer Capacitors

EDLT devices however can be difficult to fabricate precisely because they require high-quality thin films for oxide channels and precision patterning of contacts. Kasahara attempted to overcome these difficulties through use of an electric double layer capacitor (EDLC) instead[16].

The core design of an EDLC is essentially the same as an EDLT except that there are no source or drain contacts on the oxide surface, thus creating a simple capacitor. The ionic liquid dielectric still allows mobile ions to form EDLs at each electrode when an applied voltage charges this capacitor, see Figure 1.7 (b). Instead of measuring the resistance of an oxide channel, the EDLC arrangement would rely on magnetisation measurements to observe the perfect diamagnetism which is associated with the onset of superconductivity, known as the Meissner

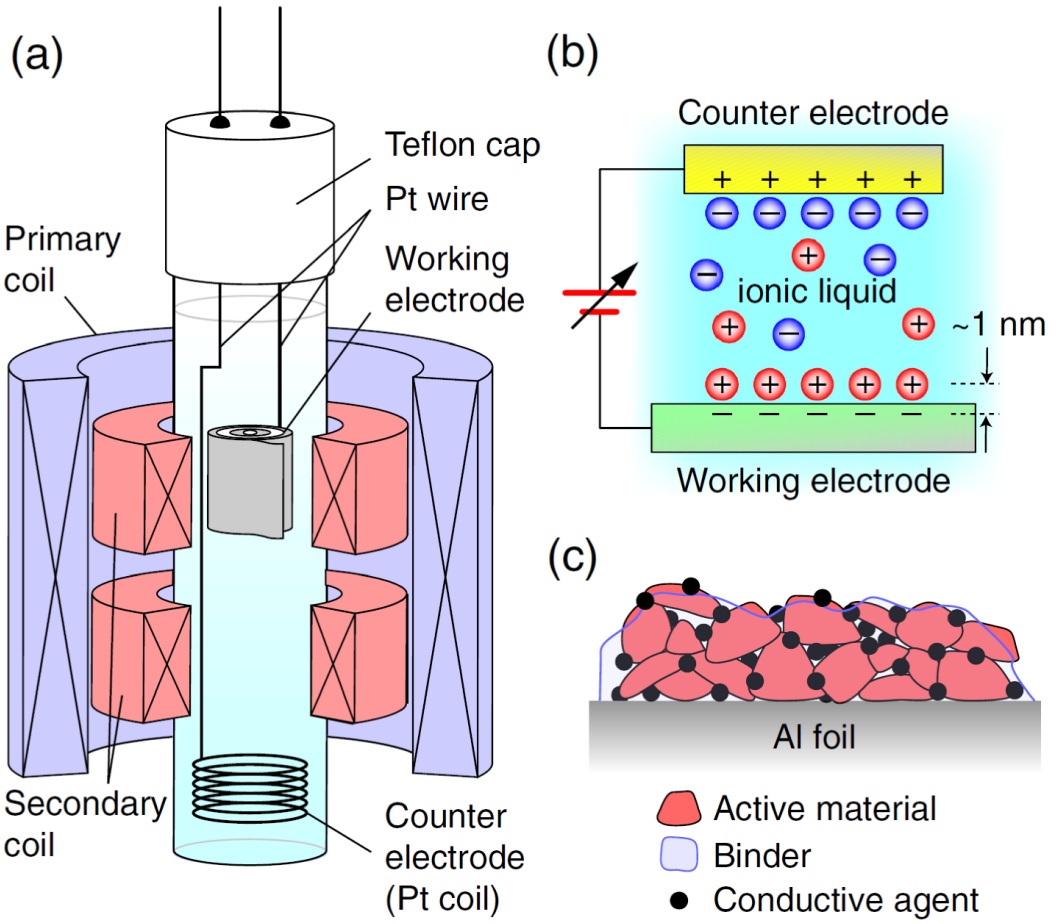

Figure 1.7 *Kasahara's EDLC in (a) its experimental setup for measurement of the magnetisation, (b) schematic illustrating EDL formation and (c) the composition of the working electrode[16].*

effect[7]. Kasahara employed a two-coil mutual inductance technique in order to monitor the AC magnetisation of an EDLC device, as can be seen in Figure 1.7 (a). The working electrode of an EDLC is not comprised of an atomically-flat film such as those used by EDLTs. Figure 1.7 (c) illustrates how instead powdered material is mixed with conductive and binding agents before being adhered to metallic foil in order to form this electrode. This is a commonly used industrial technique to ensure consistent electrical conduction and charge accumulation in the production of batteries and supercapacitors[32, 33]. Thus even though the surface of the electrode is not atomically flat, the ions arranged at the interface are sufficient to draw charge carriers to the surface of individual material flakes and form a cohesive superconducting state across all of them.

Kasahara constructs an EDLC using ZrNCl as the active material on the working electrode and the same ionic liquid N,N-diethyl-N-(2-methoxyethyl)-N-methylammonium bis(trifluoromethylsulfonyl)imide (DEME-TFSI) as used by

Ye[15]. This is purposefully done in order to provide a means of comparison between the effectiveness of his EDLC and Ye's EDLT at inducing superconductivity in ZrNCl. DEME-TFSI is a very suitable ionic liquid for EDL devices as it exhibits a large ionic conductivity and is capable of operating effectively over a wide range of voltages[34]. Temperature dependent magnetisation measurements at various gate voltages were performed on the EDLC arrangement to search for the onset of perfect diamagnetism associated with the superconducting state. These measurements confirmed the successful establishment of superconductivity in ZrNCl at gate voltages and temperatures consistent with those measured by Ye's EDLT, as shown in Figure 1.8[16]. Thus the EDLC arrangement is capable of performing as effectively as EDLTs yet does not require high-quality atomically flat single crystals, nor are magnetisation measurements as difficult to setup as transport ones.

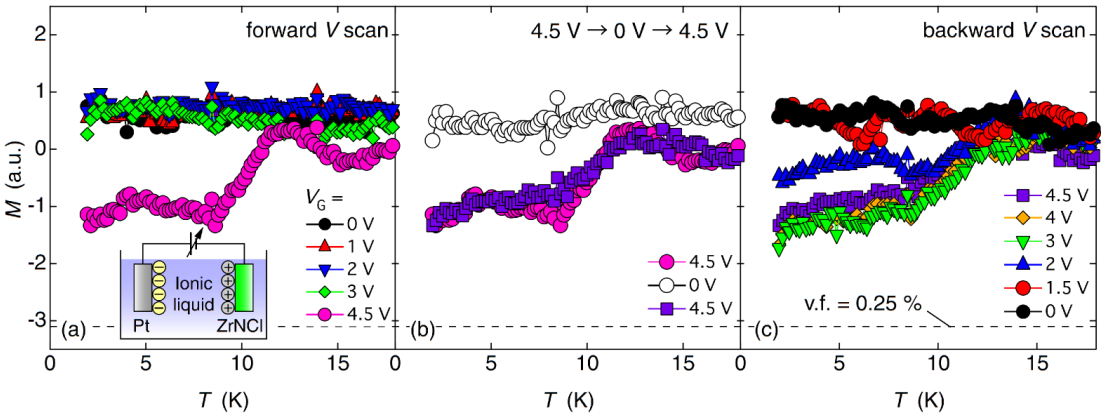

Figure 1.8 *Results of Kasahara's EDLC illustrating successful electrostatic doping of ZrNCl to induce superconductivity with (a) forward voltage scans, (b) recovery after voltage removal and (c) backward voltage scans[16].*

1.3.5 Pressure

Application of high pressures is also a common method by which superconductivity is induced or altered in various insulating materials. Under pressure a materials crystal lattice is subtly altered along with its corresponding electronic structure, thus allowing it to be tuned into other states such as superconductivity, see Figure 1.1[7, 13].

The effectiveness of electrostatic doping in EDL devices could also potentially be improved through application of pressure. Pressure can either provide rough tuning toward a particular state through the same alteration of a material's

electronic structure or possibly even increase the effectiveness of the EDL itself, by allowing more efficient arrangement of ions at the interface. Successful use of ionic liquids in EDL devices has now also enabled the possibility for its use as a medium for effective hydrostatic application of pressure. To date there has been minimal investigation into the use of electrostatic doping with pressure, with the most notable work being that carried out by Shi *et al*[35]. Shi employs an EDLT arrangement with a thin film conjugated polymer semiconductor, pBTTT-C14, gated by the ionic liquid DEME-TFSI in a piston cylinder pressure cell up to $\sim$2 GPa. Inducing metallic states in such conjugated polymers is challenging due to the high carrier densities required, and as such pressure is often employed to enhance the $\pi - \pi$ inter-chain coupling in order to achieve this. Thus Shi chose to implement pressure in conjunction with electrostatic doping in order to improve the conductivity of this polymer maximally. In doing so Shi not only enhanced the conductivity, but observed a transition from one- to three-dimensional hopping at low temperatures in transport measurements; indicative of the metallic state nearly being reached[35]. Such a result illustrates the powerful ability of pressure as a dual tuning parameter with electrostatic doping, yet its potential to improve the effectiveness of the EDL itself has not been investigated thus far.

There have also been some pressure studies on DEME-TFSI, one of the most common ionic liquids used in EDLT and EDLC devices. As the dielectric in EDL devices it is important to know what effect pressure has on it, primarily if there are any structural transitions which will inhibit its use. DEME-TFSI does have a known glass transition under ambient pressure at approximately 182 K and no known crystal phase[34], although this could potentially arise under the application of high pressures. Due to this glass transition, when DEME-TFSI is used in EDL devices a gate voltage is generally applied above this temperature, where the ions are free to move, before cooling the device and essentially freezing in the EDLs[25].

Yoshimura conducted Raman spectroscopy measurements on DEME-TFSI up to 5.5 GPa in a search for any other phase transitions under pressure[36]. Raman spectroscopy allows measurement of the vibrational frequencies of carbon-hydrogen bonds in the ionic liquid and should provide information on any structural changes. Yoshimura determined that there was no crystallisation of DEME-TFSI up to 5.5 GPa and that any pressure induced changes were completely reversible[36]. Unfortunately they did not track the pressure induced change of the glass transition temperature, and such information would be

necessary for application of gate voltages in EDL devices. Not only this, but the results from this study could very well be erroneous. Under higher pressures the peaks in the observed Raman spectrum broaden and merge into one another, Yoshimura attributes this to spatial issues of polar and non-polar sections of molecules packing together separately yet this effect is almost certainly due to non-hydrostatic application of pressure. Broadening of the Raman peaks is commonly seen when pressure has not been applied hydrostatically[37]. In all likelihood under these higher pressures DEME-TFSI exists in its glassy state and thus when pressure is applied a pressure gradient develops across the material. As such, different sections of DEME-TFSI experience different pressures and hence the broad Raman peak is merely a combination of many individually shifted Raman signals. Thus the conclusions of this study by Yoshimura must be treated with a degree of scepticism.

The investigation into electrostatic doping under pressure conducted by Shi however has shown that DEME-TFSI can be utilised as a pressure medium. Whilst the glass transition temperature was not determined for various applied pressures the leakage current across the ionic liquid between electrodes of the EDLT was measured at 300 K. Shi observed a noticeable drop in the leakage current at $\sim$0.60 GPa and a consistent value for pressures greater than this[35]. Such an observation indicates a slowing of ion mobility associated with a transition from the liquid to rubber phase which immediately precedes the glass transition[25]. Thus based on Shi's measurements for pressures $>$0.60 GPa the glass phase is likely present at room temperature. However, effective use of EDL devices relies on ion mobility; thus change of bias should be made whilst DEME-TFSI is in the liquid state[25]. Definitive mapping of the glass transition temperature of DEME-TFSI with pressure is necessary in order to ensure this.

1.4 AC Susceptibility

Fabrication of EDL devices for use under pressure will not only allow for investigation into electrostatic doping but also measurements of other material properties. Construction of EDLC devices, for instance, will result in susceptometer coil inserts for piston cylinder cells capable of pressure dependent AC susceptibility measurements. AC susceptibility is an important characterisation technique as it measures the time dependent magnetisation of a material, and thus provides information on the dynamics of a magnetic system.

1.4.1 Introduction

In the presence of a DC magnetic field H a sample will exhibit a constant magnetisation M which can be characterised by the magnetic susceptibility

$$\chi = \frac{M}{H} \tag{1.5}$$

In the case of AC susceptibility however a sample is subjected to a time varying magnetic field $H_{ac} = H_0 cos(\omega t)$ and as such exhibits a changing moment in response to this where

$$\chi = \frac{dM}{dH_{ac}} \tag{1.6}$$

As the sample moment is varying in time AC susceptibility offers an opportunity to study the dynamic magnetic behaviour of a material. Apart from superconductivity there are many other interesting magnetic phases arising in a number of systems, and AC susceptibility is capable of yielding information on thermodynamic phase transitions[2], relaxation processes[3], losses in materials, and physical properties associated with superconductivity[4]. The susceptibility is complex comprised of a real, in-phase (relative to the driving field) component χ' and an imaginary, out-of-phase component χ'' where

$$\chi = \chi' + i\chi'' \tag{1.7}$$

χ' is representative of the magnetisation of a material and χ'' the dissipative processes. The susceptibility may either be expressed in terms of these components or by the absolute magnitude χ and its phase shift ϕ in relation to the driving field as follows[2].

$$\chi = \sqrt{\chi'^2 + \chi''^2} \tag{1.8}$$

$$\phi = arctan(\chi''/\chi') \tag{1.9}$$

$$\chi' = \chi cos\phi \tag{1.10}$$

$$\chi'' = \chi sin\phi \tag{1.11}$$

AC susceptibility also provides a measurement of bulk sample properties, and thus does not exhibit the shortcomings of transport measurements which often represent only a path of least resistance through a material[4]. However it should be noted that χ depends on frequency and in metals only samples the bulk material in the low frequency limit.

1.4.2 Susceptibility Calculations

AC susceptibility measurements are generally performed with the use of SQUID and vibrating sample magnetometers. However, a sensing coil surrounding a sample can also be used to detect the flux variation caused by its time varying magnetisation (as a result of H_{ac}) via an induced voltage. Goldfarb & Minervini outlined how one may use the principle of mutual inductance to directly relate this voltage to the susceptibility[38]. If one assumes a long, uniformly magnetised cylindrical sample then it is equivalent to a solenoid coil of the same size with magnetisation $M = NI/l$ where N is the number of turns, I the current and l the length of this solenoid. The magnetic flux from this equivalent solenoid can be calculated from integration of the vector potential around the sensing coil, as it is equivalent to the double integral of the contained flux density.

$$\Phi = \iint B \cdot da = \oint A \cdot ds \tag{1.12}$$

Where da and ds are the incremental area and contour respectively. The mutual inductance between the equivalent solenoid and sensing coil, L_{sp}, per turn is thus given by

$$L_{sp}/N = \Phi/NI = \frac{1}{NI} \oint A \cdot ds \tag{1.13}$$

The induced voltage, v, in the sensing coil from the flux variation can then be expressed as follows

$$v = -\frac{d\Phi}{dt} \tag{1.14}$$

$$= -L_{sp}\frac{dI}{dt} \tag{1.15}$$

$$= \frac{-L_{sp}l}{N}\frac{dM}{dt} \tag{1.16}$$

Where the expression for magnetisation of our equivalent solenoid has been used. Relating the magnetisation back to the volume susceptibility with $M = \chi H$ and the applied field H_{ac} we can derive the expression for the susceptibility

$$\chi = \frac{v_{rms}}{2\pi L_{sp} l f H_{rms}/N} \tag{1.17}$$

Where f is the frequency and denoted values are the root mean square. The mutual inductance L_{sp} is then computationally calculated modelling the sample

as an equivalent solenoid coaxial with the sensing solenoid, as detailed by Goldfarb & Minervini[38].

In the above calculation the voltage induced in the sensing coil from the driving field H_{ac} has been neglected. In practice this is achieved in a constructed susceptometer by having two identical, yet oppositely wound, sensing/secondary coils housed symmetrically within a primary coil, see Figure 1.9. Opposite windings of these connected sensing coils ensure cancellation of any induced voltages within them from the H_{ac} field, which is provided by an alternating current in the primary coil.

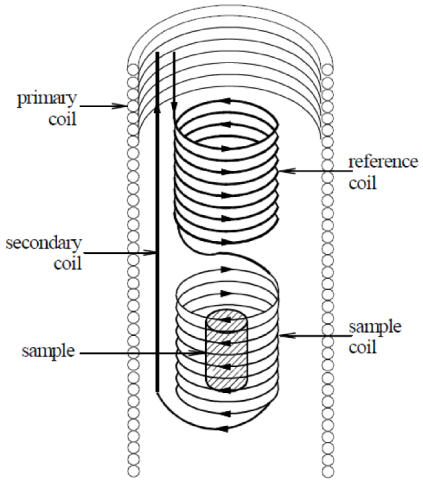

Figure 1.9 *Basic arrangement of a susceptometer with a counter wound reference coil identical to the sensing coil containing the sample, symmetrically positioned within the primary coil[39].*

Whilst the mutual inductance L_{sp} can be calculated computationally it is often more straightforward to use a calibration constant α which represents the geometry of a given coil. This calibration can be either calculated or determined experimentally as discussed in 2.2.3. Thus the induced voltage from a susceptometer is related to the susceptibility by

$$v = (1/\alpha)\mu_0 V f H \chi \tag{1.18}$$

for a given sample volume V[4]. As α reflects a coils geometry it is possible to extract the sensing coil volume from it, and thus the above equation is sometimes expressed for practical considerations in terms of the filling factor; ratio of sample volume to coil volume[40]. Thus, maximising the filling factor with as large a sample as possible will yield the strongest response.

1.4.3 AC Susceptibility of Superconductors

For a superconductor the real and imaginary susceptibilities can be expressed in terms of the average local flux density $\langle B(t) \rangle$ in the sample[4, 41]

$$\chi_1' = \Big(\frac{\omega}{\pi \mu_0 H_0} \int_0^{2\pi/\omega} \langle B(t) \rangle cos(\omega t) dt \Big) - 1 \tag{1.19}$$

$$\chi_1'' = \Big(\frac{\omega}{\pi \mu_0 H_0} \int_0^{2\pi/\omega} \langle B(t) \rangle sin(\omega t) dt \Big) \tag{1.20}$$

Where ω is the angular frequency. Thus the real susceptibility represents the degree of magnetic flux penetration into the superconductor; in the Meissner state for full expulsion of the flux $\chi_1' = -1$ and in the normal state where the flux penetrates through the sample $\chi_1' = 0$. The imaginary susceptibility in the superconducting state will yield $\chi_1'' = 0$ or a small positive value for the mixed state, indicative of the AC losses[4, 39]. The partial penetration of flux into a superconductor in the mixed state can also give rise to a variety of interesting behaviour, which strongly depends on the pinning within a particular material.

Collective Pinning

In real superconductors the Abrikosov flux line lattice of the mixed state can be pinned by defects and dislocations within a crystal, preventing their movement when subjected to a Lorentz force $\mathbf{F}_L = \mathbf{J} \times \mathbf{B}$. Such a flux line lattice however cannot be perfectly rigid as pinning sites are randomly distributed throughout a sample, and pinning forces across an entire volume would then average out to zero. Thus in order for pinning to occur the flux line lattice must be elastically deformable, allowing flux lines to shift to pinning sites and result in a collective pinning force overall. Flux lines which deviate from the rigid case are able to lower their energy by occupying the potential minima of these pinning sites. Deformation of the flux lattice however also results in an increase in energy due to the mutual magnetostatic repulsion between flux lines, thus the equilibrium state arises from the balance of these two contributions and forms the basis of weak collective pinning theory proposed by Larkin & Ovchinnikov[42]. This scenario is often represented in terms of correlation volumes V_c, of dimension R_c and L_c, within which the lattice is uniform and distortions occur between such volumes, as shown in Figure 1.10 (b). Shear and tilt distortions, characterised by elastic

moduli C_{66} and C_{44}, describe this lattice deformation and can be balanced against the pinning energy to give the free energy change per unit volume caused by pinning[43]

$$\delta F = F_{elastic} - F_{pinning} \tag{1.21}$$

$$= \frac{C_{66}}{2}\left(\frac{\xi}{R_c}\right)^2 + \frac{C_{44}}{2}\left(\frac{\xi}{L_c}\right)^2 - f\xi\frac{n^{1/2}}{V_c^{1/2}} \tag{1.22}$$

Where ξ is the coherence length, f the pinning force per site and n the density of pinning sites. Minimising Equation 1.22 with respect to the correlation volume dimensions and taking $V_c = R_c^2 L_c$ it is found that

$$L_c = \frac{2C_{44}C_{66}\xi^2}{nf^2} \tag{1.23}$$

$$R_c = \frac{2^{1/2}C_{44}^{1/2}C_{66}^{3/2}\xi^2}{nf^2} \tag{1.24}$$

$$V_c = \frac{4C_{44}^2C_{66}^4\xi^6}{n^3f^6} \tag{1.25}$$

Yielding a minimum pinning energy for the correlation volumes

$$\delta F_{min} = \frac{-n^2f^4}{8C_{44}C_{66}^2\xi^2} \tag{1.26}$$

The pinning force per unit volume $f(n/V_c)^{1/2}$ also defines the threshold Lorentz force at which flux lines are able to flow and can be used to determine the critical current density J_c

$$J_cB/c = \frac{n^2f^4}{2C_{44}C_{66}^2\xi^3} \tag{1.27}$$

Thus greater pinning energy and critical currents are achieved through either increased pinning strength, $w = nf^2$, or lower elastic moduli (resulting in a softer lattice and smaller correlation volumes) yielding an improvement in the pinning[43, 44]. The magnetic field dependencies of the elastic moduli for much of the range are given by[43]

$$C_{66} \approx \frac{BH_{c1}}{16\pi}\left(1 - \frac{B}{H_{c2}}\right)^2 \tag{1.28}$$

$$C_{44} \approx \frac{B^2}{4\pi} \tag{1.29}$$

Where H_{c1} is the lower critical field. Comparison of the moduli also shows $C_{66} \ll C_{44}$, indicating that the flux line lattice is far more susceptible to

shear deformations[44]. Indeed this predominant dependence on the shear elastic moduli has been attributed as the source for the peak effect[42–44]. As the field approaches H_{c2} the C_{66} modulus rapidly goes to zero allowing for greater shear deformations of the lattice, in turn the correlation volume shrinks even more rapidly due to the quartic dependence on C_{66} seen in Equation 1.25. In the limit of $nV_c \to 1$ the correlation volume has shrunk to such an extent that the flux line lattice can deform maximally allowing for individual pinning of flux lines. Thus, as H_{c2} is approached a sudden increase of pinning occurs and a corresponding diamagnetic signal can be observed in AC susceptibility data, as seen in Figure 1.10 (c). A hysteretic behaviour is also observable in such data indicative of the pinning remaining to lower fields[45].

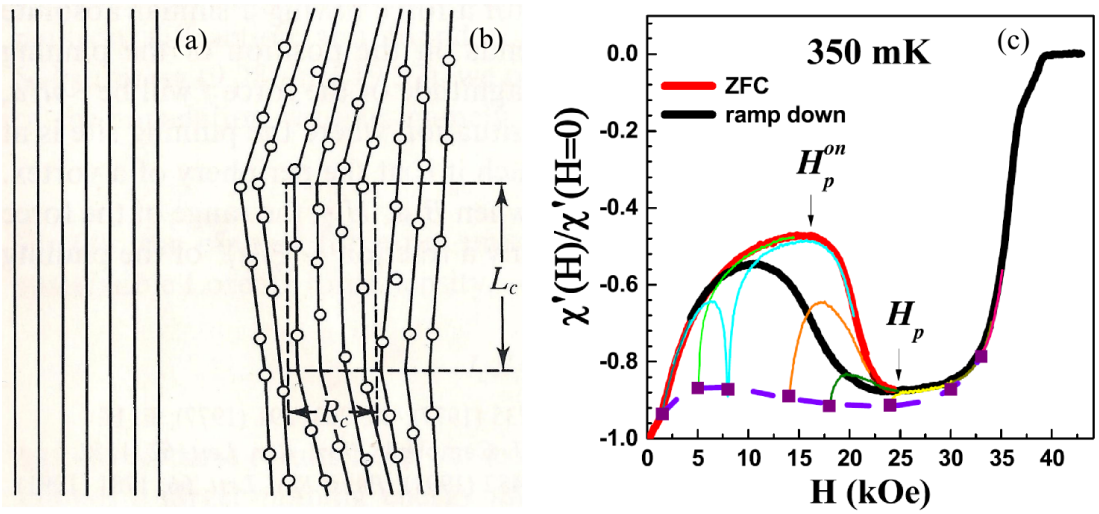

Figure 1.10 *(a) A rigid flux line lattice in the absence of pinning and (b) a distorted lattice in the presence of pinning sites giving rise to correlation volumes of dimensions R_c and L_c[43]. (c) Experimental evidence for the peak effect at H_p in field dependent AC susceptibility measurements illustrating the onset of increased diamagnetism at H_p^{ON} on approach of H_{c2}[45].*

Penetration Depth

In the presence of an AC oscillating field the motion of flux lines in a superconducting material with bulk pinning can be expressed in terms of the complex penetration depth[43, 46]

$$\frac{1}{\lambda_{AC}^2} = \frac{1}{\lambda_C^2} - \frac{2i}{\delta_f^2} \tag{1.30}$$

Where λ_C is the Campbell penetration depth and δ_f the flux-flow skin depth. λ_C defines the characteristic length scale over which oscillation of flux lines within pinning sites (due to the AC field) decays into a sample, and δ_f is the skin depth for flow of the flux line lattice given by

$$\delta_f = \sqrt{\frac{2\rho_f}{\mu_0 \omega}} \tag{1.31}$$

Where ρ_f is the resistivity due to flux flow. At very large frequencies (typically GHz in type II superconductors[43]) δ_f dominates the penetration depth and the pinning force is ineffective allowing for flux flow. In the low frequency regime however λ_C dominates and flux oscillation within pinning sites defines the behaviour[43, 47, 48]. A typical AC response for superconductors can be represented in terms of this complex penetration depth where for a cylindrical sample of radius R

$$\chi' = Re\left(\frac{2\lambda_{AC} J_1(R/\lambda_{AC})}{R J_0(R/\lambda_{AC})}\right) - 1 \tag{1.32}$$

$$\chi'' = Im\left(\frac{2\lambda_{AC} J_1(R/\lambda_{AC})}{R J_0(R/\lambda_{AC})}\right) \tag{1.33}$$

Where J_0 & J_1 are Bessel functions of the first kind and Re/Im refer to taking the real or imaginary part respectively. The ratio of the complex penetration depth to sample size is a key parameter in these susceptibilities and indeed the dissipative χ'' peaks when they are approximately equivalent[49].

Chapter 2

Experimental Methods and Considerations

In this chapter we detail the various experimental methods and considerations which are taken into account throughout the work presented in this thesis. An overview of the practical measurement of AC susceptibility is presented along with its use under pressure; including discussion of pressure cells and equipment used. In addition the design of susceptometers, balancing of considerations for greater sensitivity, and experimental restrictions are discussed along with methods for calibration. Additional aspects of AC measurements to be taken into account are also detailed.

2.1 Pressure

2.1.1 Piston Cylinder Cells

Measurements under pressure throughout this thesis were carried out with piston cylinder pressures cells; primarily a standard 1.1 GPa cell comprised of a beryllium-copper alloy (BeCu), shown in Figure 2.1 (a). The low magnetic background and high tensile strength of BeCu make it ideal for magnetic measurements under pressure. This cell has an internal diameter of 7 mm allowing for a large sample volume space which, as will be seen later in this chapter, is highly beneficial for our purposes. Samples are mounted and wired onto the cell

plug which is then firmly screwed into the base of the cell body thereby crushing the copper ring and forming a tight seal. The central bore of the cell is filled with a fluid transmitting medium to allow hydrostatic application of pressure to our sample. Daphne oil is used for our cell as a common chemically inert pressure transmitting medium[50, 51], except for the experiments discussed in Chapter 3. The cells piston is then inserted into the top of central bore firmly to seal it with a rubber o-ring, a CuBe anvil is placed on top of it and the locking nut wound into the top of the cell. Firmly engaging the locking nut will also crush the copper ring on the piston thereby sealing the internal volume of the cell. The pushing rod is fed down the centre of the locking nut and the cell pressure is increased by applying a load to it with a hydraulic press. This causes the piston to compress the transmitting medium and apply hydrostatic pressure throughout the cell volume. Once the desired pressure has been reached the locking nut is firmly engaged in order to maintain the pistons position, and thus the pressure, allowing the load to be removed. As a cell is cooled the pressure will slowly decrease as the fluid medium contracts, even once it has solidified at low temperatures, yet this can be monitored through the use of an appropriate pressure calibrant as discussed in the following section.

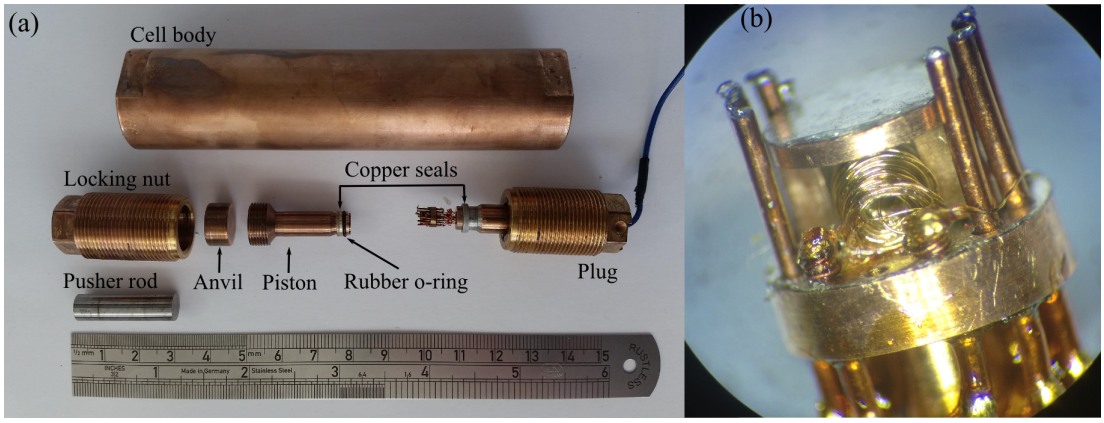

Figure 2.1 *(a) 1.1 GPa piston cylinder pressure cell dismantled into constituent parts and (b) manganin coil for pressure calibration wired under table of pressure cell plug.*

A 3 GPa piston cylinder cell was also designed and constructed by Xiao Wang specifically for AC susceptibility measurements, using coils constructed as part of this research. It is essentially the same design as the previous cell except the body is constructed of two concentric cylinders, the outer being comprised of BeCu and the inner a NiCrAl alloy, to provide greater strength and a higher maximum pressure[52]. The inner bore also makes use of a teflon tube to seal in the pressure medium and has a smaller internal diameter of 4 mm.

2.1.2 Pressure Calibration

Manganin wire, comprised approximately of 85% Copper, 12% Manganese and 2% Nickel, is often used as a pressure calibrant due to the consistent linear change of its resistance with pressure as seen in Figure 2.2 (a). The pressure coefficient of a manganin sensors resistance at a fixed temperature is given by

$$\alpha_P = \frac{1}{R_0}\frac{dR}{dP} \tag{2.1}$$

where R_0 is the resistance of the manganin wire at ambient pressure. Determination of pressure at room temperature thus only requires measurement of the resistance change in relation to the ambient pressure value, and the established room temperature pressure coefficient, $\alpha_P(298K) = 0.0234$ GPa^{-1}, for commercially available manganin wire[53].

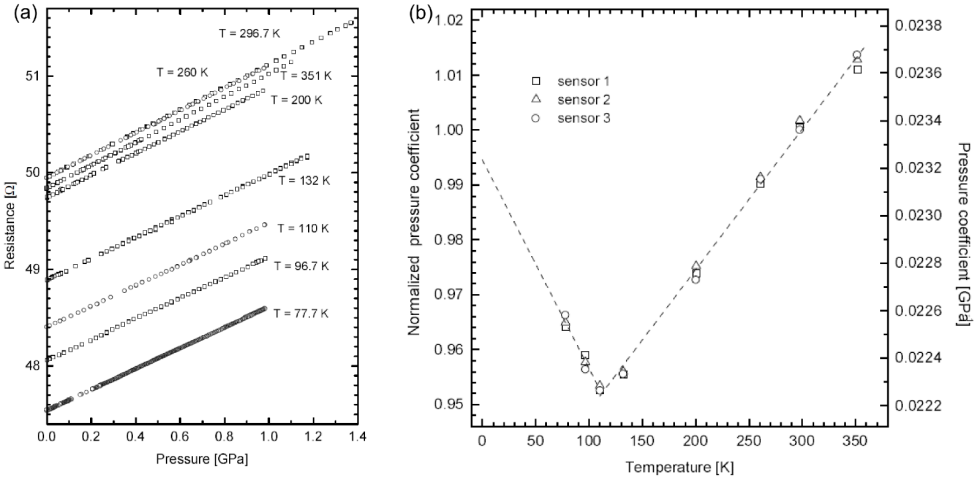

Figure 2.2 *Studies carried out by Dmowski et al illustrating (a) the linearity of manganin sensors resistance with pressure at constant temperature and (b) the temperature dependence of the pressure coefficient for several manganin sensors[53].*

Calculation of the pressure at any given temperature is more complex however, as Dmowski determined that the pressure coefficient changes with temperature as can be seen in Figure 2.2 (b). The rate of change for α_P can be linearly approximated by

$$R_\alpha = \frac{1}{\alpha_P(298K)}\frac{d\alpha(T)}{dT} \tag{2.2}$$

with values of 2.56 x 10^{-4} K^{-1} and -3.80 x 10^{-4} K^{-1} above and below 110 K respectively[53]. Combining Equations 2.1 and 2.2 the pressure in GPa for a

given manganin gauge at any temperature can be calculated as follows

$$\begin{aligned} P(T) &= \frac{R(P,T)/R(P_{Amb},T)-1}{\alpha_P(T)} \\ &= \frac{R(P,T)/R(P_{Amb},T)-1}{\alpha_P(298K)(1-\Delta T R_\alpha)} \end{aligned} \tag{2.3}$$

Provided that the manganin sensors resistance has been measured at each required temperature at ambient pressure.

Manganin sensors for our pressure cells have been created by loosely winding many turns of manganin wire in a loose 'birds nest' configuration, as shown in Figure 2.1 (b), such that the total resistance of the sensor exceeds 100 Ω to ensure sufficient measurement accuracy. Manganin sensors formed from coils of wire are susceptible to internal strain impeding the reproducibility of their resistance, unless they are heat and pressure trained[54]. As such all manganin sensors were annealed at ≈ 100℃ for 24 hours and rapidly cooled with liquid nitrogen several times to provide appropriate heat treatment, as well as being subjected to the maximum pressures achievable by our cells several times. Such heat and pressure trained manganin sensors yield reproduceable resistances across the temperature and pressure ranges under four terminal measurements[54, 55].

2.2 AC Susceptibility & Coil Design

2.2.1 AC Susceptibility Measurement

A sample inserted into one sensing coil of a susceptometer (see Figure 1.9) will induce a voltage which can be measured with the use of a lock-in amplifier as described by Nikolo[4]. The total magnetic flux from a sample completely filling the N_s turn sensing coil of radius r_s is given by

$$\Phi = \mu_0 \pi {r_s}^2 N_s M(t) \tag{2.4}$$

where $M(t)$ is the magnetic induction of the sample per unit volume and the flux from the applied field has cancelled due to the oppositely wound coils. Making use of Equation 1.14 the voltage is directly related to the magnetic induction by

$$v(t) = -\mu_0 \pi {r_s}^2 N_s dM(t)/dt \tag{2.5}$$

The AC magnetic susceptibility is complex comprised of real, χ'_n, and imaginary, χ''_n, components of multiple harmonics n which can be seen from a Fourier expansion of $M(t)$

$$M(t) = \sum_{n=1}^{\infty} H_0(\chi'_n cos(n\omega t) + \chi''_n sin(n\omega t)) \tag{2.6}$$

Combining this with Equation 2.5 and setting the prefactors to v_0 we have

$$v(t) = v_0 \sum_{n=1}^{\infty} n(\chi'_n sin(n\omega t) - \chi''_n cos(n\omega t)) \tag{2.7}$$

We need only consider the fundamental, $n = 1$, harmonic however as higher harmonics are the result of flux entering and exiting the sample[4]. A lock-in amplifier can be used to measure this voltage and also the phase relative to a reference signal at the same frequency; in this case the current in the primary coil generating H_{ac}. In this way it is also able to resolve this into the real and imaginary components of the susceptibility directly[39].

$$v_1 = v_0(\chi'_1 sin(\omega t) - \chi''_1 cos(\omega t)) \tag{2.8}$$

$$= v_y sin(\omega t) + v_x cos(\omega t) \tag{2.9}$$

Thus root mean square voltages v_y and v_x measured by the lock-in amplifier are related to the susceptibilities χ'_1 and χ''_1 respectively by v_0, which is equivalent to the prefactors from Equation 1.18.

It must be noted that in the above the self induced flux from the sensing coil has been neglected as the current will be negligible due to the lock-in amplifiers high impedance[39]. Also in practice no matter how careful the construction it is unlikely for two sensing coils to be identical, and as such there will always be a small voltage from the susceptometer when no sample is present representing this imbalance. This mismatch may be corrected for in several ways. One method involves cancelling it by connecting a variable ratio transformer in series or using the lock-in amplifier's internal offset, however the imbalance voltage will change based on field and temperature (due to uneven thermal expansion of components) which will require constant adjustments throughout a measurement. Alternatively the sample can be moved between the sensing coils by use of a motor to average its voltage response and cancel out this imbalance[4, 38]. However such a setup is not possible if the susceptometer is loaded in a pressure cell as

we aim to do for our measurements. The most straightforward and effective correction for this voltage imbalance is to obtain a background measure of the empty susceptometer across the temperature regime, with fixed fields and frequencies of interest. Subtraction of this background from our sample voltage should adequately account for any mismatch between the sensing coils.

2.2.2 AC susceptibility Under Pressure

AC susceptibility provides a means of investigating the dynamics of magnetisation for a number of materials, especially when combined with pressure as a tool for tuning materials through a variety of phases and phenomena. AC susceptibility has been employed with materials under pressure in a number of ways over the years.

Generally the most common method for pressure dependent measurements of susceptibility involves subjecting samples to high pressures with piston cylinder, Helium gas or anvil type pressure cells, and measuring the response from this entire apparatus utilising SQUID or vibrating sample magnetometers (VSM)[56–58]. However there are a number of limitations associated with such a method. Firstly, requiring the entire pressure cell to fit within the equipment bore restricts not only the cell size, and hence the maximum pressure attainable, but also the sample dimensions. Piston cylinder cells would allow the maximum sample size, as opposed to anvil type cells, yet relative to the equipment bore this is often still relatively small yielding a weak measurement signal[40]. Primarily the magnetic response of the cell itself is the greatest limiting factor with this method. In order to deduce a samples magnetic moment it is necessary to measure the response of the empty pressure cell and subtract this from measurements. The response of the cell can often be larger than that of the sample itself, thus making its moment difficult to determine accurately even with background subtraction[58]. AC fields subjected to an entire cell body can also produce eddy currents within the cell walls, potentially causing significant heating or stray fields depending on the frequency used. Such limitations can possibly be avoided through use of cells constructed from materials with low magnetic contributions, yet this often is at the expense of cell strength and hence pressure attainable[40]. Operation of SQUID and vibrating sample magnetometers also introduce a degree of mechanical vibrations, which at low temperatures for a pressure cell could have a noticeable effect on measurement resolution and sensitivity[40].

Construction of a susceptometer designed to fit inside a pressure cell bypasses many of these issues. Sensing coils may be wound almost directly around a sample, thereby maximising the filling factor and achieving a far greater sample response compared to the previous method, even if its size is restricted due to the internal volume of the cell. The background contribution from the pressure cell is also minimal as the field from the primary coil is concentrated within its central bore[58]. Furthermore, this minimises eddy currents in the cell walls, as well as allowing for use of stronger materials in cell design that may otherwise have had a more noticeable magnetic contribution[40]. Even if strong eddy currents are induced these do not screen the field at the sample position such as an external coil would. There have even been measurements where primary coils providing driving fields have been wound to the exterior of pressure cells to maximise the interior sample space[59], yet this again brings up a concern of induced eddy currents within cell walls thus restricting frequencies used to very low levels.

Whilst use of susceptometers is most common in helium gas, piston cylinder or uniaxial pressure cells[60] it is also possible to implement these in anvil type cells[58]. However such an implementation is far more experimentally challenging due to the restrictive size associated with these cells, and makes quantitative measurements difficult[58, 61].

2.2.3 Calibration

Calibration of the voltage signal from a susceptometer is necessary in order to extract a meaningful value for a material's absolute magnetic susceptibility. Several calibration methods are possible yet each has its associated benefits and drawbacks.

Firstly, the mutual inductance L_{sp} may be calculated computationally as a means of calibration using Equation 1.17. Goldfarb and Minervini have carried out such a calculation by modelling coaxial solenoids[38], yet this can prove to be computationally intensive and time consuming. Such modelling also presumes perfect coils which in practice is not likely to be the case.

It is more common and straightforward to make use of a calibration constant α to reflect the coil geometry as shown in Equation 1.18. It is possible to calculate α if one assumes the sample size is small compared to the radius of the sensing

coil, and thus can be simply approximated by a magnetic dipole[4].

$$\alpha = \frac{10^8}{8\pi^2 n_s} \frac{({l_s}^2 + {d_s}^2)^{1/2}}{l_s} \tag{2.10}$$

With n_s being the number of turns per centimetre, l_s the length and d_s the diameter of the sensing coil in centimetres. However, such an assumption is only valid for small samples and often it is desirable to maximise our signal by using samples that fill the entire coil volume negating this requirement. As such this method of calibration is not always the most suitable.

Empirical determination of the calibration constant more often provides the most direct and accurate estimation. Standards of a known susceptibility can be measured in a susceptometer and used to determine the required α for it. Such a method is relatively simple, yet the calibration is only valid for samples the same size and shape as the standard used[38]. An even more direct method for experimental calibration is to determine the response of a sample with the use of a SQUID magnetometer and utilise this to calibrate the measurements of the same sample within the susceptometer. Such a method removes any uncertainty between size and shape that might exist between a sample and the standard used for calibration. Whilst direct experimental determination in this manner can be time and equipment intensive if relatively few samples are to be measured (as is the case for this work) it proves to be the most beneficial. A potential issue of susceptometer calibration is the magnetoresistance of coil wires, if the primary is driven by a voltage source, altering the measured signal and introducing error. This however can be remedied with use of an empty coil background subtraction utilising consistent AC fields between measurements, a procedure which is already intended to address any potential coil imbalance as mentioned in Section 2.2.1.

2.2.4 Demagnetisation Factor

When determining the true susceptibility of a material it is important to account for the demagnetising field it generates. As can be seen in Figure 2.3, when a magnetic material is subjected to a field its magnetisation forms effective poles at either end of a sample thus setting up an internal demagnetising field, H_d, and ultimately reducing the applied field[62].

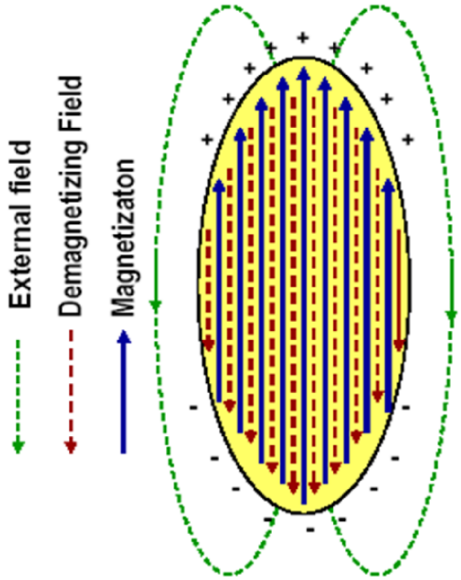

Figure 2.3 *Effective poles set up by samples magnetisation form an internal demagnetising field within the sample thereby reducing the total field[62].*

For magnetic induction within a sample

$$B = \mu_0(H + M) \tag{2.11}$$

Where the field H is the applied field H_a corrected for this demagnetising field, $H = H_a + H_d$. The demagnetising field is proportional to the magnetisation of a sample M and for an applied field along the central axis of an ellipsoid is related to it by the scalar factor D, such that $H_d = -DM$[63]. Thus in order to deduce the true internal susceptibility of a sample, χ_{int}, from the measured susceptibility, χ, one must account for this demagnetisation factor

$$\chi_{int} = \frac{\chi}{1 - D\chi} \tag{2.12}$$

The demagnetisation factor is dependent only on the sample shape and direction of the applied field. The further apart the poles the less effect demagnetisation fields have, for instance an infinitely long cylinder has a demagnetisation factor $D = 0$ as opposed to a disc where $D = 1$. Thus for relatively short samples demagnetisation can have a significant effect on the measured susceptibility as will be the case for our samples. Exact determination of demagnetisation factors is only possible for ellipsoids due to their uniform field distribution[38, 63], yet average values for such factors have been calculated for cylinders[64] and rectangular prisms[65–67] which are suitable for our samples. In general

demagnetisation factors are categorised based on the ratio of primary to secondary axis length for ellipsoids or in the case of cylinders the ratio of length to diameter, a series of such calculated factors for cylinders can be seen in Figure 2.4[38].

l/d	*D*	*l/d*	*D*	*l/d*	*D*
0.0	1.000	2.0	0.181	4.0	0.0978
0.1	0.796	2.1	0.174	4.1	0.0956
0.2	0.680	2.2	0.167	4.2	0.0935
0.3	0.594	2.3	0.161	4.3	0.0914
0.4	0.528	2.4	0.155	4.4	0.0895
0.5	0.474	2.5	0.149	4.5	0.0876
0.6	0.430	2.6	0.144	4.6	0.0858
0.7	0.393	2.7	0.140	4.7	0.0841
0.8	0.361	2.8	0.135	4.8	0.0824
0.9	0.334	2.9	0.131	4.9	0.0808
1.0	0.311	3.0	0.127	5.0	0.0793
1.1	0.291	3.1	0.123	5.5	0.0723
1.2	0.273	3.2	0.120	6.0	0.0666
1.3	0.257	3.3	0.116	6.5	0.0616
1.4	0.242	3.4	0.113	7.0	0.0573
1.5	0.230	3.5	0.110	7.5	0.0536
1.6	0.218	3.6	0.107	8.0	0.0503
1.7	0.207	3.7	0.105	8.5	0.0473
1.8	0.198	3.8	0.102	9.0	0.0447
1.9	0.189	3.9	0.100	10.0	0.0403

Figure 2.4 *Table of long axis oriented demagnetisation factors for cylinders of various length to diameter ratio (l/d)[38].*

2.2.5 Susceptometer Design

In designing a suitable susceptometer for use in pressure cells the general procedure is to construct a bobbin on which to wind the sensing and primary coils, yet there are several considerations which must be taken into account and balanced against one another to ensure optimal performance.

Material Choice

The material chosen to construct the bobbin must satisfy a number of constraints. It must be suitably robust and relatively incompressible such that it remains intact and its volume does not change significantly under the application of pressure. It should also have a low thermal expansion to ensure its dimensions remain relatively unchanged across the full temperature range. Any significant change in the bobbin's volume, with either pressure or temperature, could damage the wound coils or alter their arrangement causing inconsistencies between measurements. A suitable choice should also be easily machinable to allow

construction of consistent bobbins featuring fine and precise details. Most importantly it must be a non magnetic material to avoid introducing background signals to measurements, as well as electrically insulating to prevent shorts between coils. Thus a plastic or ceramic material is the best choice to satisfy these constraints.

Initially bobbins were constructed of teflon as an easily machinable plastic, yet this proved unsuitable as it undergoes a phase transition at ≈ 0.6 GPa with an associated volume change[68], which had a noticeable effect on our measurements. A machinable glass ceramic (MACOR) was then trialled due to its ease of machinability and low expansion properties, however it proved too fragile for the finer details required for the susceptometer. Finally a pure thermoplastic polymer PEEK (polyether ether ketone) was settled on as a suitable material, it too is highly machinable and still robust even for finely detailed bobbins. PEEK also has essentially no magnetic contribution, a low thermal expansion & compressibility[69] and has no known structural transitions under pressure; thus making it an ideal choice.

Bobbin Design

Ultimately the absolute dimensions of the bobbin are determined based on the size restrictions imposed by our pressure cells. The internal bore may only accommodate a susceptometer of a particular length as the piston intrudes further into the cell reducing the internal volume as pressure is increased; thus for both our pressure cells the bobbin length is restricted to ≈ 14 mm. The internal bore also sets an upper limit on the bobbin's diameter, however due to deformation of sealing rings under pressure it is necessary to reduce this limit even further to ensure safe extraction of susceptometers post measurement. Thus for the 1 GPa and 3 GPa pressure cells the bobbin diameters are restricted to ≈ 5 mm and ≈ 3 mm respectively.

Recessed channels on the bobbin provide a solid housing to maintain the shape and structure of coils wound into them even when subjected to pressure, as can be seen in Figure 2.5 (a). In order to provide this stable housing the maximum length allowable for our primary coils is 12 mm, placing a limit on the number of turns in a single layer for a given wire diameter. However the depth of these channels can be altered to allow multiple layers for a given coil. As mentioned previously secondary coils must be placed symmetrically within the primary coil

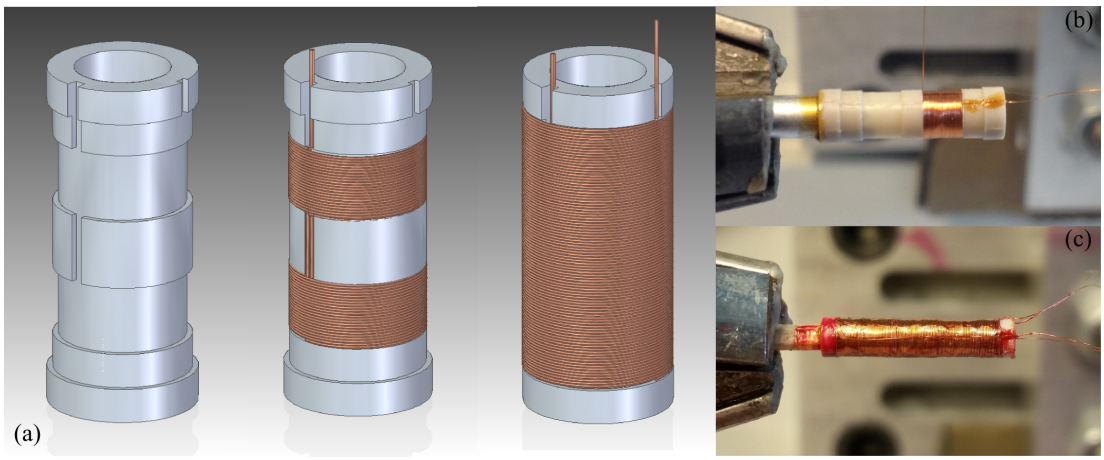

Figure 2.5 *(a) Design of bobbin with illustration of secondary and primary windings across its features, (b) a secondary coil being wound onto a PEEK bobbin and (c) a completed susceptometer with a long multi-layer primary wound atop the secondary coils.*

such that they experience the same field profile, illustrated in Figure 2.6. A secondary coil length of 3 mm was chosen to maximise the size of sample that may be measured, as well the signal generated by our susceptometer. A separation between the secondary coils of the same length is required in order to reduce field overlap and flux coupling between them, ensuring the greatest sensitivity[4, 60]. Optimisation of the susceptometer's sensitivity has also accounted for the filling factor consideration in the design. The wall separating the secondary coil from the sample space has been reduced to 0.15 mm allowing samples of comparable volume to the coil to be measured, resulting in an optimal filling factor and hence maximum signal achievable.

Coil Winding

In order to improve sensitivity the number of turns in both secondary and primary coils is maximised by winding fine insulated 63 μm copper wire into these recessed channels; a coil winding machine is used and manually monitored throughout the process. As the coil balance of secondaries is very sensitive to imperfections between windings this must be carried out carefully and any mishaps corrected during the winding procedure. Multiple windings of a secondary coil act as a voltage amplifier of the measured signal and so multi-layered secondaries are desirable[4, 40]. Upon completion each layer is sealed with dilute nail varnish to bind wires preventing vibrations and displacement during use[60], as well as providing a smooth surface for winding of further layers on top of it. Very

careful balancing of secondary coils through opposite windings ensures maximum cancellation of any signal from them, as well as compensating for any background signal from the surrounding pressure cell[40]. Balancing can be achieved through unwinding turns or adding additional turns on one secondary to minimise coil signal; however, it can be difficult to determine the actual imbalance until a primary has been wound onto it, at which point altering the number of turns is no longer a possibility. Thus careful precise winding is the first and foremost consideration for the secondary coils. Primary coils are wound atop completed secondary coils where multiple layers help to increase the maximum field through creation of concentric solenoids as discussed in Section 2.2.6.

Figure 2.5 (b) and (c) indicates a designed bobbin being wound with such secondary and primary coils in practice respectively. These susceptometers have been used as the sensing apparatus for the EDLC arrangement as well as for measurement of AC susceptibility throughout this work. Table 2.1 lists the appropriate specifications for the constructed susceptometers.

	Design 1	Design 2
Susceptometer Diameter	4.8 mm	2.95 mm
Internal Volume Diameter	3.5 mm	1.9 mm
Length of Primary	12 mm	12 mm
No. of Primary Layers	3	3
Total No. of Primary Turns	570	570
Length of Secondary	3 mm	3 mm
No. of Secondary Layers	3	2
No. of Turns in each Secondary	141	94
Resistance of Primary at 300 K	$\sim$80 Ω	$\sim$50 Ω
Total Resistance of Secondaries at 300 K	$\sim$36 Ω	$\sim$15 Ω
Inductance of Primary	456.65 μH	168.08 μH
Inductance of each Secondary	64.50 μH	11.27 μH

Table 2.1 *Table of specifications for main coil designs employed in AC and EDLC measurements. Inductances calculated based on the multi-layer consideration discussed in Section 2.2.7.*

2.2.6 Field of Coil

The driving field of our manufactured susceptometers is supplied by applying an alternating current to the wound primary coil. The field from a current at any point along the central axis of a finite solenoid is given by altering the formula

for an infinite solenoid to account for end corrections as follows

$$B = \frac{\mu_0 N_p I_p}{2l}(cos\theta_1 + cos\theta_2) \tag{2.13}$$

Where N_p are the number of turns, I_p the current and l the length of the primary coil with θ_1 and θ_2 the angles formed from a point along the coil axis to either end of the coil. As our primary coils are multi-layer the field from each layer can be calculated using Equation 2.13 and added to give the total field along the central axis. Using such an approach a profile of the AC field along the central axis can be determined. As can be seen in Figure 2.6 the field is not constant across the secondary coils within a 12 mm long susceptometer, ideally a longer primary coil would ensure a constant field yet due to the size restrictions imposed by our pressure cells this is not possible. Thus the average along the axis of a secondary coil is the best indication of the field experienced by a sample within it, given by

$$B_{avg} = \frac{1}{b-a}\int_a^b B dx \tag{2.14}$$

Where b and a are the start and end positions of the secondary coil along the coil axis.

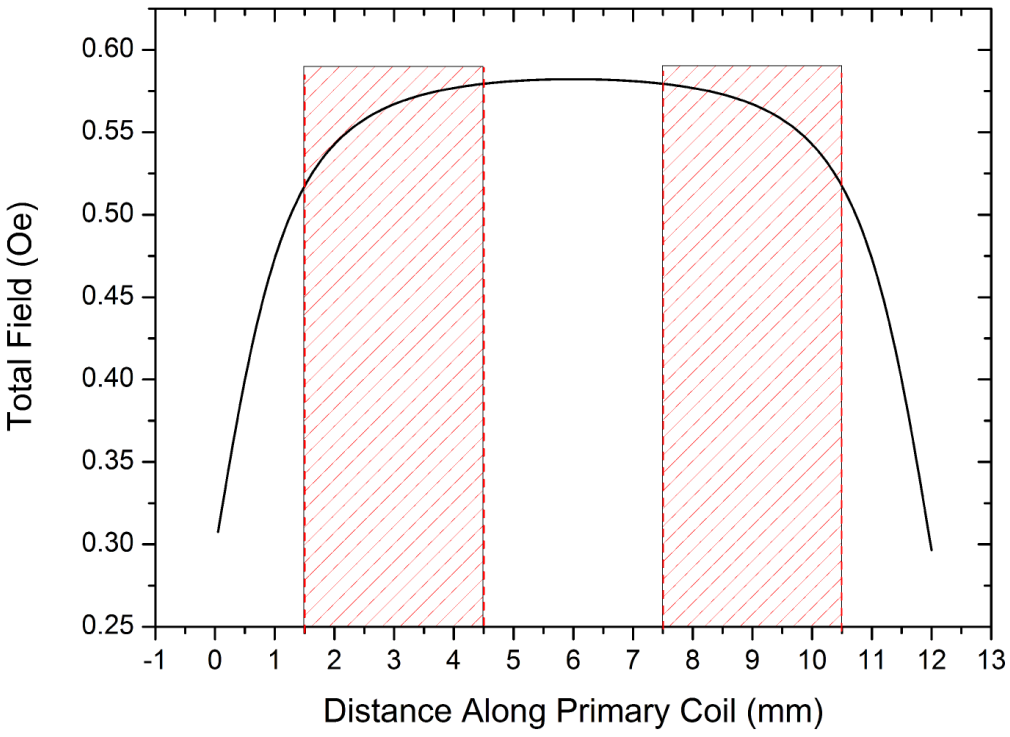

Figure 2.6 *Calculated magnetic field profile along a 12 mm primary coil of a design 2 susceptometer for 1 mA applied AC current. Dashed boxes indicate positions of secondary coils along field profile.*

Using Equation 2.14 the average field along the axis of the secondary coils for the example in Figure 2.6 is ≈ 0.56 Oe for a 1 mA applied current. It should be noted that the calculations underpinning determination of the AC susceptibility often assume a uniform magnetisation from a constant AC field yet as can be seen this will not be the case for our susceptometers, with an $\approx 3\%$ variation from the average. Whilst it is not possible to construct longer susceptometers the calibration constant α in Equation 1.18 determined experimentally can account for this variation across a sample[40].

2.2.7 Frequency Considerations

As of yet frequency has not been mentioned in great detail, however for AC susceptibility measurements there are several important considerations which must be taken into account in regards to this.

As mentioned in the previous section, the field is supplied by driving the primary coil with an alternating current which is most effectively accomplished by a current source; such as the Keithley 6221 employed for many of our measurements. However current sources often have a limited frequency range, with the Keithley 6221 having a maximum operating frequency of 10 kHz. If higher frequencies are desired a voltage source can be connected to our primary coil in order to supply the alternating current. Of course in this case as the resistance of our primary coil, R_p, changes with temperature a large resistor must be connected in series to ensure a stable current within the coil; this stabilising resistor primarily determines the current in the circuit. Whilst the resistance of a coil falls with temperature the frequency dependent inductive impedance does not, yet must still be accounted for in determining the total impedance of the primary coil as follows

$$Z_p = \sqrt{R_p^2 + (\omega L_p)^2} \tag{2.15}$$

Where $\omega = 2\pi f$ and L_p is the self inductance of our primary coil. The self inductance for a single layer solenoid of length l, turns N and cross sectional area A is given by

$$L_p = \frac{\mu_0 N^2 A}{l} \tag{2.16}$$

However our primary coils are multi-layer in order to provide as large a field as possible. Their inductance can thus be determined more accurately by numerical means making use of Maxwell's elliptical integral formula for coaxial

circular filaments[70]. This allows calculation of the mutual inductance between pairs of wires and summing across an entire coil will give the total inductance. Programs implementing this numerical method have already been created and optimised thus we make use of such a program[71] to determine our multi-layer coil inductances, L_{multi}, and compare these to that predicted for single layer coils from Equation 2.16. As can be seen in Table 2.2 accounting for the multiple layers of a coil provides a more accurate value of its true inductance and thus shall be used throughout this thesis.

	Primary		*Secondary*	
Coil Type	L_p	L_{multi}	L_p	L_{multi}
Design 1	503.32 μH	456.65 μH	98.46 μH	64.50 μH
Design 2	167.01μH	168.08 μH	14.07 μH	11.27 μH

Table 2.2 *Comparison of self inductances for coil designs 1 & 2 based on single and multi-layer coil calculations.*

The frequency supplied to our primary coil will thus determine its total impedance based on Equation 2.15 and values for L_{multi}. Table 2.3 illustrates coil impedances for a range of frequencies and its proportion to a resistor inserted to stabilise the current when connected to a voltage source. As can be seen a suitably large resistor of say 10 $k\Omega$ can provide a stable current within 1% up to 0.1 MHz or even up to 1 MHz with a 100 $k\Omega$ resistor. A larger stabilising resistor will limit the current supplied to a coil depending on a given sources maximum voltage, however this will not be an issue if the field generated is suitable for our measurements.

		Z_{coil}/R (%)		
Frequency (Hz)	Z_{coil}	1 $k\Omega$	10 $k\Omega$	100 $k\Omega$
100	50	5	0.5	0.05
1000	50.01	5.01	0.501	0.05
10000	51.1	5.11	0.511	0.051
100000	116.8	11.68	1.168	0.117
1000000	1057.3	105.73	10.573	1.057

Table 2.3 *Frequency dependent impedance of coils at 300 K based on the more commonly used design 2 specifications and their proportion to an inserted stabilising resistor of varying values.*

A voltage (back emf) can also be induced from the self inductance of a primary coil introducing a phase lag to the alternating signal driving it. However for our coils the inductances are very low and as with the impedance this dephasing only

becomes appreciable for very high frequencies. Thus impedance and dephasing issues can generally be managed by keeping operating frequencies relatively low, and if higher frequencies are required triggering a lock-in amplifier directly from the primary circuit itself can resolve this issue[4]. The self inductance of secondary coils is often negligible due to their connection to a high impedance lock-in amplifier ($\sim$ 10 MΩ) rendering any impedance change insignificant[4, 39], and opposite windings of the secondary coils will cancel any induced emf contributions regardless.

2.2.8 Eddy Currents & Skin Effect

In the presence of a time-varying magnetic field loops of current, known as eddy currents, are induced in planes perpendicular to flux lines in a conducting material due to Faraday's law of induction. Lenz's law predicts that these eddy currents produce magnetic flux in opposition to those which induced them in the first place thereby reducing the total flux and attenuating it exponentially the further it permeates into a material. Thus the current density is greatest near the surface and attenuates deeper into a conductor in what is known as the skin effect[72]. The characteristic length scale for this attenuation is known as the skin depth, corresponding to a decrease in the surface field of $1/e$ ($\approx 37\%$)

$$\delta = \sqrt{\frac{2\rho}{\mu\omega}} \tag{2.17}$$

Where ω is the angular frequency, ρ is the resistivity and μ is the permeability of a material[73]. Figure 2.7 illustrates the skin depth's dependence on these parameters. Higher frequencies, conductivity or permeability of a material reduce the skin depth and thus we observe faster attenuation of eddy currents and field penetration into a sample. Conversely for low values of any of these parameters a much higher degree of field penetration is able to occur due to a larger skin depth. Generally the ratio of skin depth to sample dimension, d, is indicative of the overall situation; for $d/\delta \gg 1$ the eddy currents are confined to the surface and effectively screen the interior of the sample from the field, whereas for $d/\delta < 1$ we have full flux penetration through a sample with some attenuation between these limits.

The real susceptibility χ' provides a direct measure of this attenuation and the screening of the AC field[75]. If a conducting material of known permeability

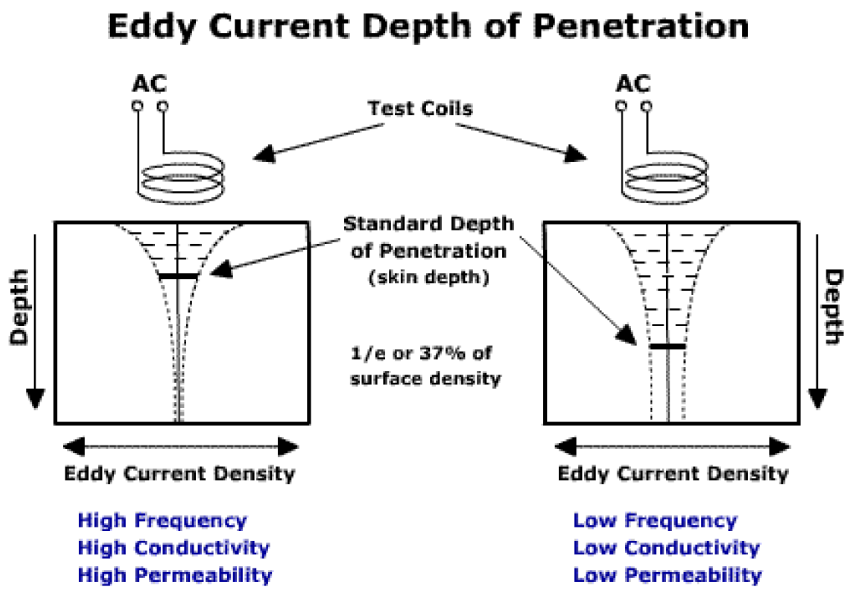

Figure 2.7 *Illustration of AC field penetration into a sample where parameter values determine the skin depth. Dashed lines indicate planes of eddy current loops which are attenuated further into a sample as they reduce the field penetration[74].*

is subjected to a field of fixed frequency the skin depth will only change with temperature, due to its changing resistivity. Thus χ' plotted versus temperature, effectively d/δ, will initially yield minimal values for full penetration at high temperatures. However, as temperature falls the skin depth becomes appreciable to the sample dimension and screening takes place, with χ' growing in magnitude accordingly.

Eddy currents also produce heat in resistive materials and are a source of energy loss, which can be detected through the dissipative part of the susceptibility χ''[2]. In superconductors the skin depth is equivalent to the penetration depth and thus eddy currents contribute to the AC losses observed in χ'' along with other dissipative processes[76]. Eddy currents can also be induced in the conductive walls of a surrounding pressure cell which could contribute both heat to our system and also reduce the field subjected to our sample. However the field generated by a susceptometer is primarily concentrated along its internal axis and is much weaker exterior to it. Thus if fields are kept relatively low this should not present a significant issue.

Chapter 3

Ionic Liquid Glass Transition Pressure Mapping

Ionic liquids have proven highly effective as dielectrics in electric double layer devices for electrostatic doping in a range of materials. N,N-diethyl-N-methyl-N-(2-methoxyethyl)ammonium bis(trifluoromethanesulfonyl)imide (DEME-TFSI) in particular is a commonly used ionic liquid dielectric due to its large electrochemical potential window and a low glass transition at 182 K[34, 36, 77] where the mobility of ions falls to zero[25]. No known crystal phase has been observed[34]. Tuning of material properties using an EDL device relies on ion mobility and thus it is important to ensure that any bias is applied above glass or solid phase transitions.

Application of pressure provides a dual tuning parameter in tandem with the electric field and potentially could increase the versatility of EDL devices yet progress is hampered by the lack of an accurate pressure-temperature phase diagram for DEME-TFSI. To date there has been some research into the use of pressure with electrostatic doping[35] and on DEME-TFSI's structure[36] yet no definitive mapping of the glass transition shift. In this chapter we present our published results[1] on expansivity and leakage current measurements of the ionic liquid dielectric DEME-TFSI to provide a temperature-pressure phase diagram mapping the glass transition temperature up to $\sim$1 GPa. This should allow the effective operation of EDL devices using DEME-TFSI under pressure.

3.1 Experimental Setup

As ionic liquid dielectric properties cannot be measured by conventional means due to their high ionic conductivity[78] we instead opted to measure the expansivity of the liquid as it undergoes the glass transition. Many materials upon undergoing a liquid-glass transition experience a sudden change in their expansivity[79] which should be detectable with a sensitive pressure gauge.

Initial measurements employed a heavily doped n-InSb single crystal, whose resistance is sensitive to pressure, to detect this transition and determine the pressure within the cell. A noticeable discontinuous jump in pressure will indicate the change in expansivity and hence the glass transition. However it became apparent that this pressure gauge was not sensitive enough for the purposes of our measurement as the discontinuity became indistinguishable from noise at higher pressures. It was also discovered that the electrical contacts within the cell decomposed due to electrochemical reactions with the ionic liquid. This is a common issue for EDL devices and requires electrical insulation of contacts from the liquid usually by coating them in GE varnish[80]. A KYOWA KFL-02-120-C1-11 strain gauge, normally designed to measure minute expansion or contractions of crystals, provides a far greater degree of sensitivity in detecting the expansivity change associated with the glass transition. Whilst unable to provide a direct numerical measure of the liquids expansivity it should register a relative change as it undergoes this transition. Such a strain gauge is employed in conjunction with a thermally cycled manganin gauge which should also detect this change in expansivity but is primarily used to track the pressure[53] within the cell as discussed in Section 2.1.2.

In order to measure the leakage current through DEME-TFSI platinum plates of area 50 mm^2, separated $\sim$100 μm apart by insulating plastic spacers, were chosen for immersion in the ionic liquid in order to avoid electrochemical reaction on application of voltage. A constant 2 V are applied between the plates whilst the small leakage current through the ionic liquid is measured by a Keithley 6517A electrometer. A low voltage must be applied in order to remain within the potential window for DEME-TFSI and prevent oxidation/reduction reactions[34, 77]. Plates of other metals were initially trialled yet platinum proved the most resilient against any such electrochemical degradation. DEME-TFSI is also dried prior to use under a vacuum line pressure of $\sim$5 x 10^{-3} mbar at $\sim$120°C for 24 hours to reduce water content and prevent electrolysis under

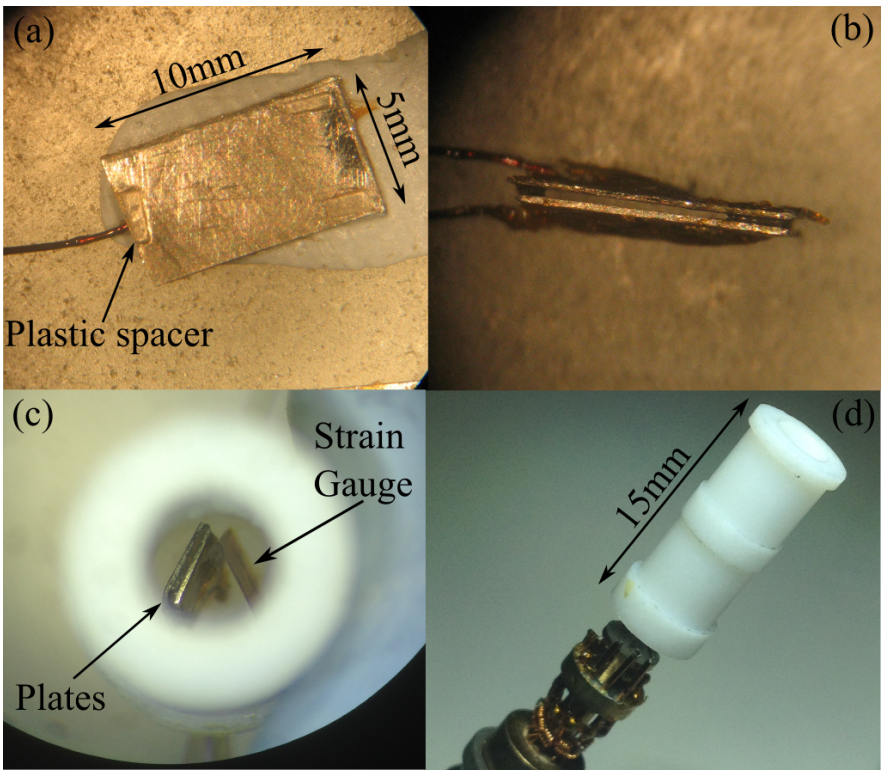

Figure 3.1 *(a) Platinum plate with plastic spacers affixed, (b) assembled plates with ∼100µm spacing between, (c) plates and strain gauge mounted within teflon capsule and (d) teflon capsule capsule mounted on pressure cell plug.*

voltage application[34, 77]. The platinum plates and strain gauge were placed within a teflon capsule and mounted on the plug of the 1.1 GPa pressure cell as shown in Figure 3.1. Measurements are taken at each applied pressure whilst the cell is cooled and warmed on a cold finger closed cycle cryostat.

3.2 Analysis

3.2.1 Expansivity Measurements

The change in expansivity of DEME-TFSI is measured by monitoring the temperature dependent resistance of a manganin gauge and sensitive strain gauge immersed in the ionic liquid within the pressure cell. At ambient pressure a small discontinuity in the manganin gauges resistance is detected as it is cooled or warmed within the cryostat at 176.4 ± 2.0 K. Strain gauges are specially designed to measure the stress and strain of a material as it undergoes

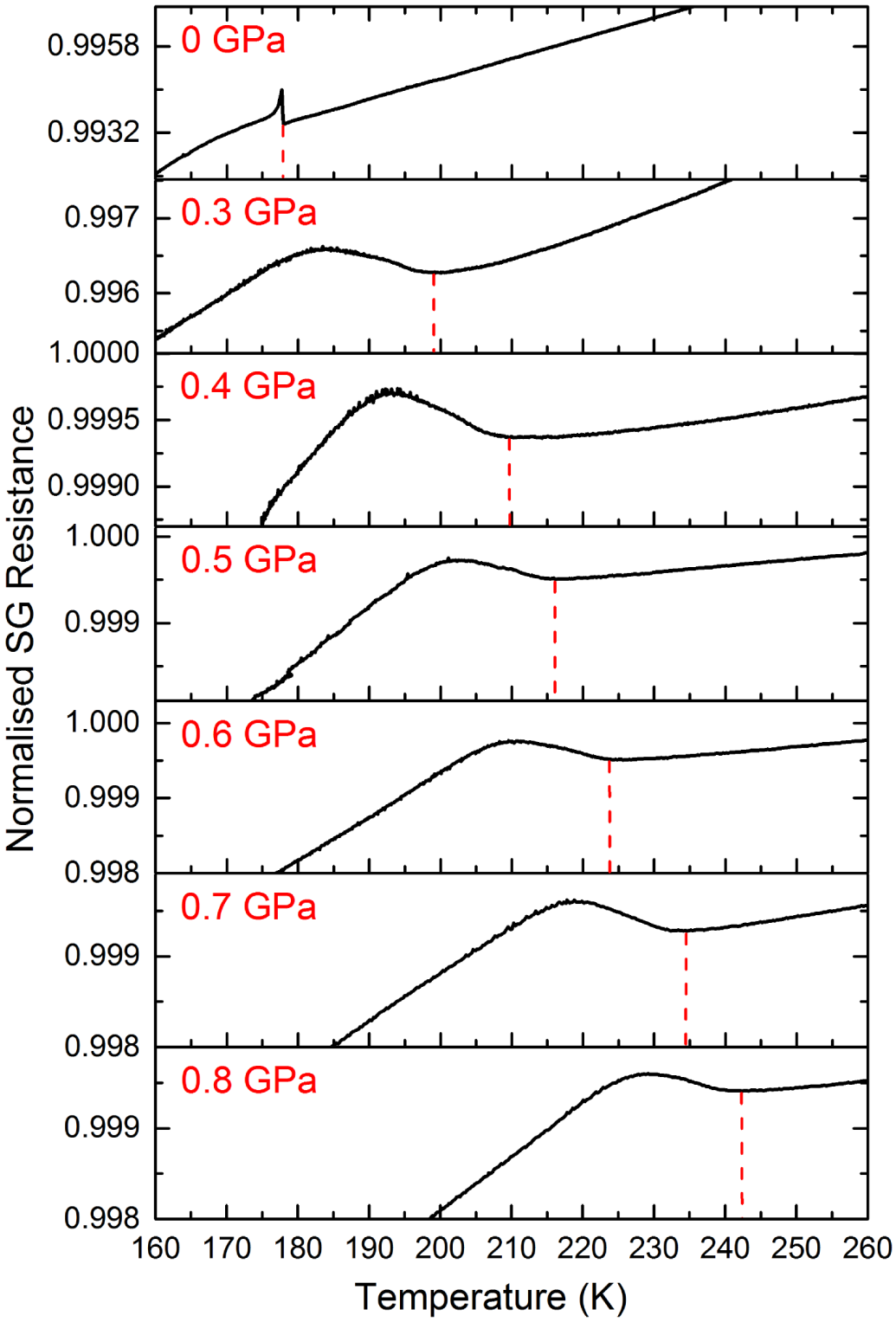

Figure 3.2 *Temperature dependent normalised strain gauge resistance at various pressures. Dashed lines indicate proposed onset of glass transition in DEME-TFSI and approximate room temperature applied pressures are listed.*

expansion or contraction with temperature change[50], as such it also exhibits a similar, but more greatly pronounced, discontinuity at 179.0 ± 3.1 K visible in Figure 3.2. These values are approximately consistent with the observed glass transition temperature of DEME-TFSI at 182 K[34, 36, 77] indicating that these discontinuities are indeed associated with this phase change.

Further measurements are conducted at a range of pressures after the pressure cell has been sealed and loaded. The discontinuity previously seen in the manganin gauge became indistinguishable from noise at the following pressure steps and thus we were unable to determine the glass transition temperature using this gauge. However due to the sensitive nature of the strain gauge we were still able to observe and track the glass transition temperature which shows steady increase with pressure as can be seen in Figure 3.2. Interestingly under pressure the change in expansivity detected by the strain gauge is no longer a sharp discontinuity but rather a broad peak disrupting the approximate linearity of the resistance with temperature. Potentially this feature could be due to the pressure within the cell falling with temperature, as is often seen with the slow contraction of any pressure medium, essentially resulting in the glass transition being shifted across a larger temperature regime thereby spreading out the sharp discontinuity. Another possibility is that upon transitioning into the glass phase the pressure application is no longer hydrostatic resulting in a pressure gradient across the DEME-TFSI. If large enough not all of the DEME-TFSI may remain in the glass phase until lower temperatures are reached thus resulting in a less defined transition zone. Regardless of the loss of the sharp discontinuity the onset of this broad peak is still indicative of a change in expansivity thus we take this to be our estimate for onset of the glass phase transition as shown by the dashed vertical lines in Figure 3.2.

3.2.2 Ionic Liquid Conductivity Measurements

The ionic conductivity of DEME-TFSI quickly falls with temperature as ion mobility slows on approach of the glass phase, this can be observed by the rapidly decreasing leakage current between plates immersed within it[25]. As shown in Figure 3.3 at approximately 0.3 GPa of pressure we see just such an exponential decrease until it plateaus at a stable value. This plateau is consistent with previous measurements of the leakage current at ambient pressure where DEME-TFSI experiences a rubber phase between its liquid-glass transition and

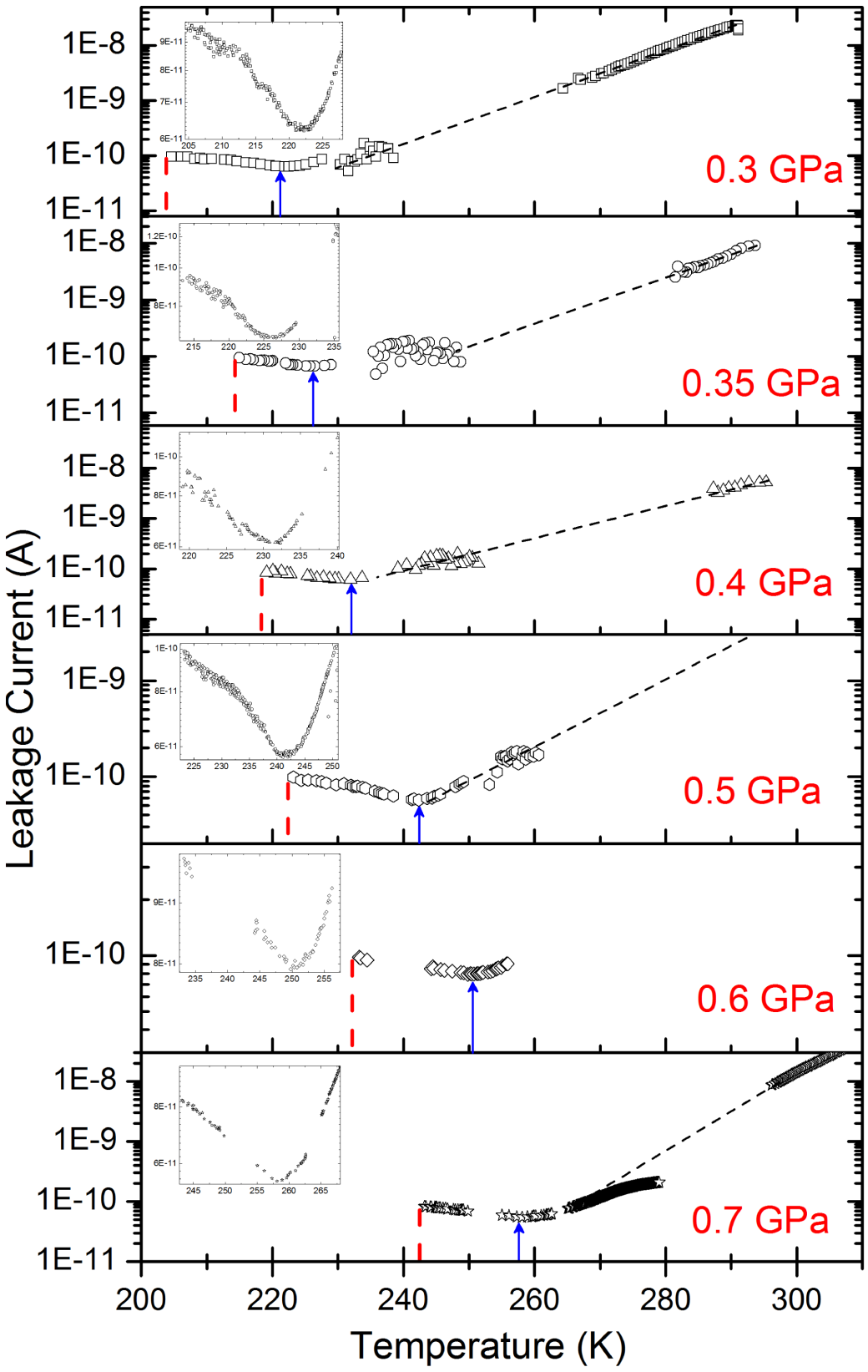

Figure 3.3 *Leakage current across platinum plates immersed in DEME-TFSI at various pressures. Vertical dashed lines indicate proposed onset of glass transition, arrows the weak minimum for rubber phase extent and approximate room temperature applied pressures are listed. Insets feature zoomed in view of the weak minimum.*

ion mobility begins to slow[25]. There appears to be a weak minimum of the leakage current at the edge of this plateau, indicated by arrows and seen in insets of Figure 3.3, that could be taken to correspond to the limit of the rubber phase. At 204 K there is a sharp cutoff where it is believed the ion mobility suddenly slows to such an extent on approaching the glass phase that measurements exceed the limits of our instrumentation ($I < 1 \times 10^{-12}$ A) and as such we have taken this to be our measure of the glass transition.

Figure 3.3 illustrates how the cutoff, weak minimum and plateau region are all shifted to higher temperatures as the pressure is increased indicating the glass transition and rubber phase migration is consistent with the expansivity shifts observed in Section 3.2.1. Dashed lines indicate extrapolation of stable high temperature data down to the plateau as measurements in this intermediate region were too erratic to provide meaningful data due to the conductivity changing too rapidly. Interestingly the leakage current in the rubber phase remains constant at approximately 1×10^{-10} A implying that the absolute ion mobility in this phase is independent of pressure.

3.2.3 Phase Diagram

Figure 3.4 shows the glass transition temperatures determined by averaging multiple thermal cycles of expansivity and leakage current measurements at each pressure. Rather than using room temperature applied pressures, as in Figures 3.2 & 3.3, values at each observed glass transition temperature were determined using the manganin gauge[53] to provide the most accurate pressure experienced by DEME-TFSI at this point.

The estimate of the glass transition temperature from leakage current measurements appears to be consistently higher than that determined from the strain gauge. In all likelihood this is due to the fact that ion mobility slows markedly whilst DEME-TFSI is in the rubber phase[25]. Thus the expansivity measure from the strain gauge provides the most accurate estimate of the glass transition temperature whilst the leakage current cutoff helps indicate the lower regime of the rubber phase immediately above it rising in tandem with increased pressure. At higher pressures the leakage current cutoff position became more erratic between thermal cycles as evidenced by the large error on the final data point in Figure 3.4 at $\sim$ 0.6 GPa. Thus reliable measurement of the cutoff for higher pressures was not possible. Potentially this could be attributed to

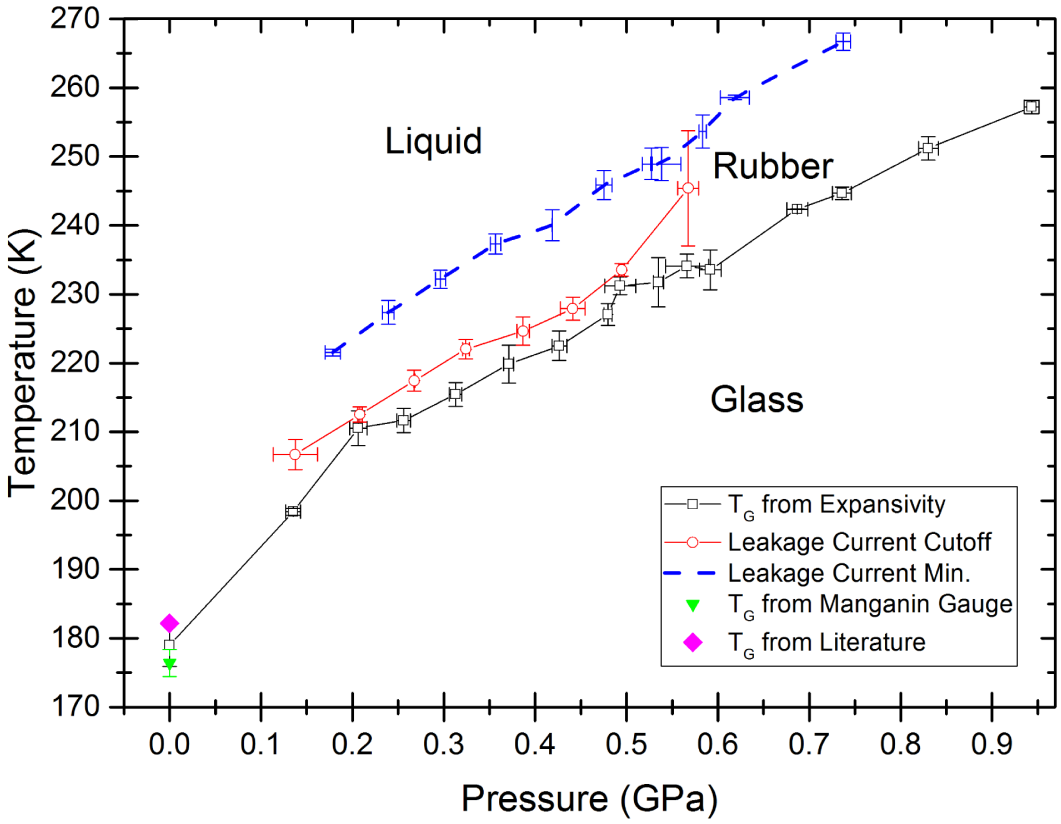

Figure 3.4 *DEME-TFSI temperature-pressure phase diagram as determined from leakage current and expansivity measurements under pressure. Pressure at each temperature determined using manganin gauge[53]. Dashed line indicates proposed onset of rubber phase between liquid-glass transition. Included is ambient pressure glass transition from literature[34, 77].*

higher pressures physically affecting the plate setup within the cell and reducing its limit of accuracy. Regardless the weak minimum of the leakage current was still consistently resolvable up to even greater pressures allowing mapping of the rubber phase onset.

Previous measurements of the leakage current in an EDL device have suggested that this rubber phase is present at room temperature for pressures in excess of 0.59 GPa[35]. Considering the weak minimum in our leakage current measurements to mark the extent of the rubber phase we have plotted this on our phase diagram and would estimate a value of around 255 K at $\sim$ 0.6 GPa. The leakage current would be significantly low even at room temperature for such a pressure due to slowing ion mobility on approach of the rubber phase as seen in Figure 3.3. Thus the estimate of the rubber phase onset at room temperature from literature[35] may simply be a premature determination based on the low leakage

current prior to the minimum and lack of numerous measurements. Extrapolation of our phase diagram thus suggests the rubber phase has fully set in at room temperature at $\sim$ 1 GPa.

3.3 Conclusions

Through expansivity and leakage current measurements we have mapped the glass transition and shift of the rubber phase of DEME-TFSI up to applied pressures of 0.95 GPa to create a pressure-temperature phase diagram. Effective application of EDL devices at ambient pressure generally requires change of bias at 40 - 60 K above the glass temperature to ensure ion mobility and a set wait time for equilibrium to be established[25]. Our data shows that this should be done at increasing temperature with pressure. We also note that the leakage current measured in the rubber phase is almost independent of pressure. Thus mobility of the ions appears to remain unchanged with pressure implying that the same wait time for equilibrium on change of bias at ambient pressure can be applied at other pressures.

Chapter 4

Electrostatic Doping of $La_{2-x}Sr_xCuO_4$

The superconducting cuprate compound $La_{2-x}Sr_xCuO_4$ (LSCO) has proven to be highly sensitive to electrostatic doping in the past[31] and thus should provide an excellent demonstration of our electric double layer devices capability. In this section we discuss the synthesis of an already superconducting cuprate compound and its characterisation. Measurement of LSCO's susceptibility using the susceptometer described in Chapter 2 is presented for ambient pressure, as well as within an EDLC device in an attempt to shift the superconducting onset temperature T_c with electrostatic doping. Successful implementation should allow use of our devices within a piston cylinder pressure cell in order to investigate any potential increase in its effectiveness under pressure.

4.1 $La_{2-x}Sr_xCuO_4$ Review

The lanthanum family were the first cuprate high temperature superconductors to be discovered by Bednorz and Müller in 1986[8] of which $La_{2-x}Sr_xCuO_4$ (LSCO) is a member. As mentioned in Section 1.2 cuprates generally have a perovskite structure with layered copper oxide planes in which the superconductivity originates[17]. LSCO is a type II hole doped superconductor where substitution of the trivalent La with divalent Sr atoms introduces holes to the single copper oxide plane seen in Figure 4.1 (a). Increasing the hole carrier density within these

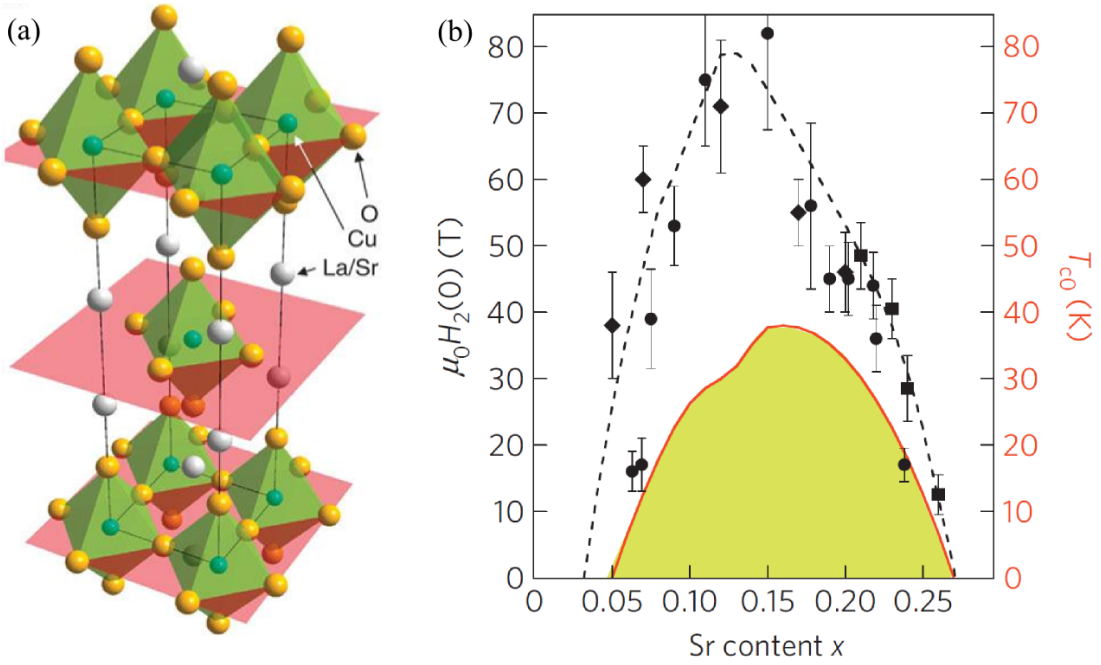

Figure 4.1 *(a) Crystal structure of layered $La_{2-x}Sr_xCuO_4$[83] and (b) Phase diagram indicating Sr doping concentration with relevant T_c and H_{c2}[84].*

planes suppresses the antiferromagnetic parent phase and leads to new electronic states such as superconductivity[81, 82].

Structurally LSCO is the simplest of the cuprate family containing only a single copper oxide layer with a relatively low maximum T_c of $\approx$ 40 K at an optimal Sr doping of $\sim$0.15 - 0.16 as can be seen in Figure 4.1 (b). Although T_c's as high as 44 K have been reported[85]. However it has been of particular interest due to its intermediate out-of-plane anisotropy providing a link between the 2D $Bi_2Sr_2CaCu_2O_{8+x}$ and 3D $YBa_2Cu_3O_x$ cuprate systems. The small lower critical fields in the cuprates results in a magnetic phase diagram predominantly occupied by the mixed phase, and the doping dependent anisotropy of LSCO gives rise to a number of vortex phases within this; such as the vortex fluid and vortex glass. AC susceptibility has previously been employed along with DC magnetisation in order to probe these various vortex states in single crystal LSCO[86, 87].

We primarily however are concerned with LSCO as a prospective material for electrostatic doping. Bollinger investigated the effects of such doping on LSCO single crystal films by constructing multiple EDLT devices with various dielectrics to probe its superconductor-insulator transition. Temperature dependent measurements of the sheet resistance in these EDLTs illustrated their capability in shifting the T_c by up to 30 K, an appreciable portion of its maximum,

under various gate voltages as shown in Figure 4.2 (a). The electrostatically induced carrier density within the LSCO copper oxide planes was determined from the sheet resistance and yielded a critical density of $\sim$ 0.06 holes per unit cell for the superconductor-insulator transition with a maximum T_c at $\sim$0.15 - 0.16. This carrier density is analogous to the doping proportion x as it is induced only within the uppermost copper oxide layer by these EDLTs, and as such the electrostatic phase diagram very closely matches that obtained from chemical doping shown in Figure 4.1 (b). Bollinger also employed the mutual inductance technique to measure the diamagnetic response and shifted T_c, under various gate voltages, of his LSCO films to further corroborate device operation as seen in Figure 4.2 (b)[31, 88].

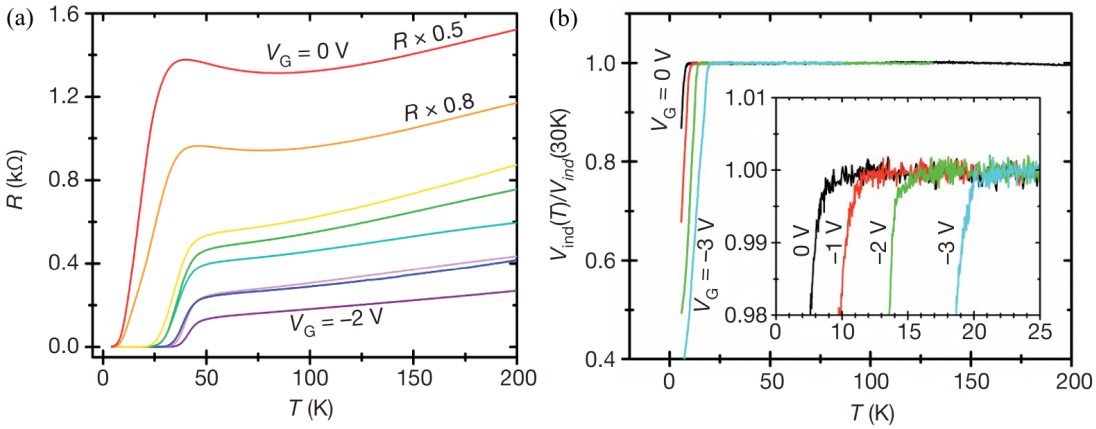

Figure 4.2 *The shifted superconducting transition of LSCO thin films under various listed gate voltages in temperature dependent measurements of (a) resistance in EDLT devices and (b) mutual inductance voltages from coils surrounding LSCO films[31].*

LSCO has thus already proven to be susceptible to electrostatic doping with its T_c highly sensitive to applied gate voltages. As such it is an excellent material to utilise in our electrostatic doping under pressure to determine the effectiveness and implementation of our EDL devices.

4.2 Synthesis and Characterisation

4.2.1 Solid State Synthesis

EDLC devices allow more straightforward application of electrostatic doping without the need for single-crystalline, atomically-flat films by making use of powdered material coated on the working electrode of a device. Thus we opted

to synthesise polycrystalline $La_{2-x}Sr_xCuO_4$ material to implement in our EDLC. A doping concentration of $x = 0.10$ was chosen to be on the underdoped side of LSCO's phase diagram (see Figure 4.1 (b)). Any degree of electrostatic doping should then markedly change the measured T_c. Polycrystalline LSCO was synthesised by grinding together stoichiometric amounts of La_2O_3, $SrCO_3$ and CuO and decarbonating them at 900°C for ∼10 hrs. The resultant powder was further ground and pressed into pellets before being sintered at 950°C in air for ∼20 hrs and cooled to room temperature[89]. Powder X-ray diffraction was carried out on the resultant material and as can be seen in Figure 4.3 single phase $La_{1.9}Sr_{0.1}CuO_4$ was produced with minimal impurities.

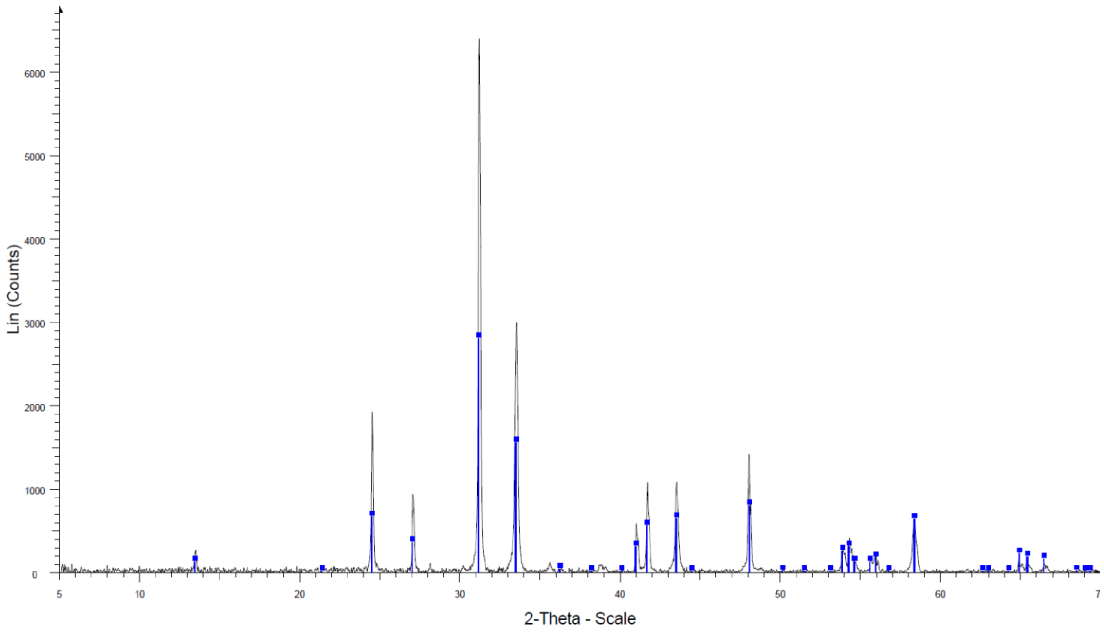

Figure 4.3 *Powder x-ray diffraction spectrum taken on a 0.15418 nm wavelength Bruker D2-Phaser X-Ray Diffractometer of the synthesised LSCO sample ground with a mortar and pestle. Blue lines with dots indicate the overlaid database pattern for* $La_{1.9}Sr_{0.1}CuO_4$.

4.2.2 AC Susceptibility Measurement

The polycrystalline LSCO powder was loaded into a cylindrical teflon capsule, and its AC susceptibility response through the superconducting transition measured for several frequencies in a SQUID magnetometer. The magnetic moment, m, is measured in emu and can be converted to a volume susceptibility in dimensionless MKS units by

$$\chi = \frac{4\pi m}{H_{a0} V_s} \tag{4.1}$$

Where H_{a0} is the driving field amplitude in Oersteds (Oe) and V_s is the sample volume in cm^3[90]. As can be seen in Figure 4.4 (a) T_c ~23.6 K for our sample which is consistent with a doping concentration of $x = 0.10$ on LSCO's phase diagram, thereby confirming the desired phase has been synthesised.

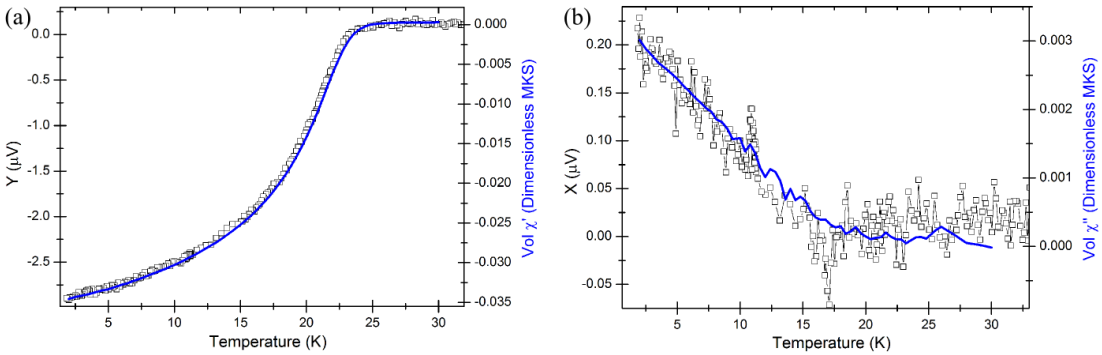

Figure 4.4 *Comparison of (a) out-of-phase and (b) in-phase measured voltage signals in the susceptometer (empty squares, left axis) to SQUID measured real and imaginary susceptibilities (blue line, right axis) respectively on the LSCO sample at 573 Hz in an ~2.8 Oe average field.*

The same teflon capsule was loaded into a susceptometer of design 1, chosen primarily to maximise sample space and hence signal, to provide a direct comparison with SQUID measurements. A Keithley 6221 AC current source supplied the driving current to the primary coil to generate the AC field; whilst the secondary coil was connected to a Signal Recovery 830 lock-in amplifier triggered by the 6221. No filters were employed in order to avoid dephasing the measured signal. While secondary coils have been carefully counterwound to cancel any induced signal from them, there still remains a small imbalance which must be corrected for. Thus temperature dependent measurements on the empty susceptometer were performed at the frequencies and AC fields of interest. Subtraction of this background from measurements of the LSCO sample have produced in- and out-of-phase voltage signals which reproduce the imaginary and real susceptibilities measured in a commercial MPMS very closely, as can be seen in Figure 4.4.

The measured voltages from the lock-in amplifier can be directly related to the real and imaginary susceptibilities as shown in Equation 2.9 by using the prefactors of Equation 1.18. A calibration factor α is necessary and may be determined in a number of ways as discussed in Section 2.2.3. Figure 4.5 illustrates how α determined by the dipole approximation proves insufficient, as would be expected for our much larger cylindrical sample. Experimentally

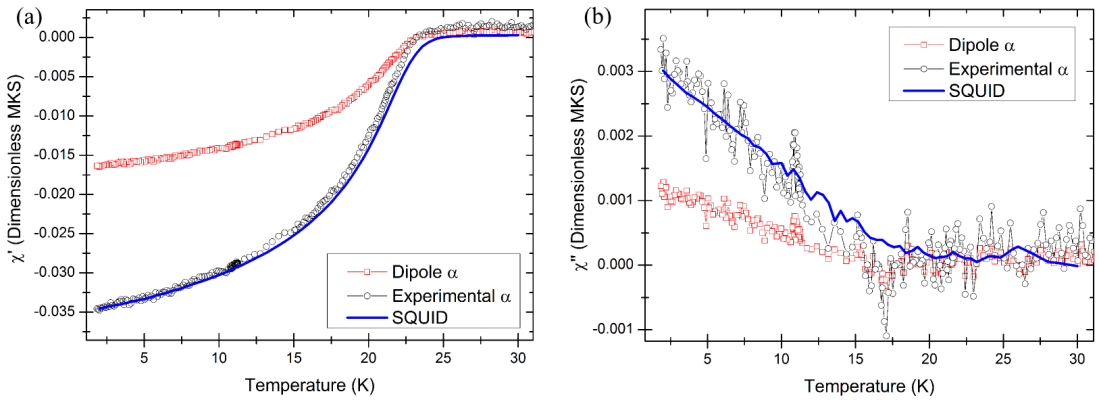

Figure 4.5 *(a) Real and (b) imaginary susceptibilities of LSCO sample measured in the susceptometer applying the dipole approximation (red squares) and experimentally determined (black circles) α's at 573 Hz in an ∼2.8 Oe average field overlaid with SQUID measurements (blue line).*

determining α based on SQUID measurements provides a much more effective calibration of our susceptometer measurements. A small deviation of the χ' calibrated data from SQUID measurements in the normal state vicinity is evident, which can be attributed to the background subtraction. Any differences in the immediate experimental environment near the susceptometer between measurements can give rise to a small additional background contribution, thus resulting in a slight change in the signal magnitude. Thus perfect background subtraction is not always possible. However, any residual background is minimal and experimental calibration still provides accurate χ' and χ'' susceptibilities for our susceptometer.

While χ' from our susceptometer allows determination of the same T_c for our sample we can also gain information on the energy dissipation from χ''. In polycrystalline cuprate superconductors generally two peaks can be observed in χ'', due to inter- and intra-grain contributions as seen in Figure 4.6 (a). The collection of individual grains couple at lower temperatures with a much lower critical field than individual grains themselves. Thus as the temperature rises flux and shielding currents first penetrate this inter-grain mix giving rise to hysteretic losses in addition to thermal flux creep. These losses are maximised upon full penetration resulting in the coupling peak in χ''. Above this peak grains decouple and losses reduce until the same penetration and losses arise in individual grains, resulting in a second intra-grain peak very near T_c. This intra-grain peak however is very weak in comparison to the coupling peak and only evident under larger AC fields as seen in Figure 4.6 (a)[4, 91].

χ'' for our LSCO sample thus does not exhibit this intra-grain peak due to the low fields used in our measurement. However, losses do appear at T_c and continue to grow as the temperature falls shown in Figure 4.5 (b). These losses do not appear to reach the maximum associated with the coupling peak, however, implying that the grain coupling is weak and they remain decoupled until very low temperatures.

The coupling peak is known to shift to lower temperatures and broaden as the applied field is increased due to increased flux creep, as illustrated in Figure 4.6 (b)[4, 91, 92]. Figure 4.6 (c) shows how measurements at higher fields on our LSCO sample produced a shallower gradient for χ'' which is consistent with this coupling peak broadening. Thus our applied field of ~2.8 Oe is likely too high to observe the coupling peak in χ'' in the measured temperature range. A lower AC field potentially could shift the coupling peak into the observable range, yet lower fields may prove difficult for accurate measurement with our susceptometer. As can be seen in Figure 4.6 (c) at 573 Hz a fair degree of noise is already evident for a low field of ~2.8 Oe; however, as the signal is directly proportional to field and frequency (see Equation 1.18) increasing either of these improves the signal-noise ratio markedly.

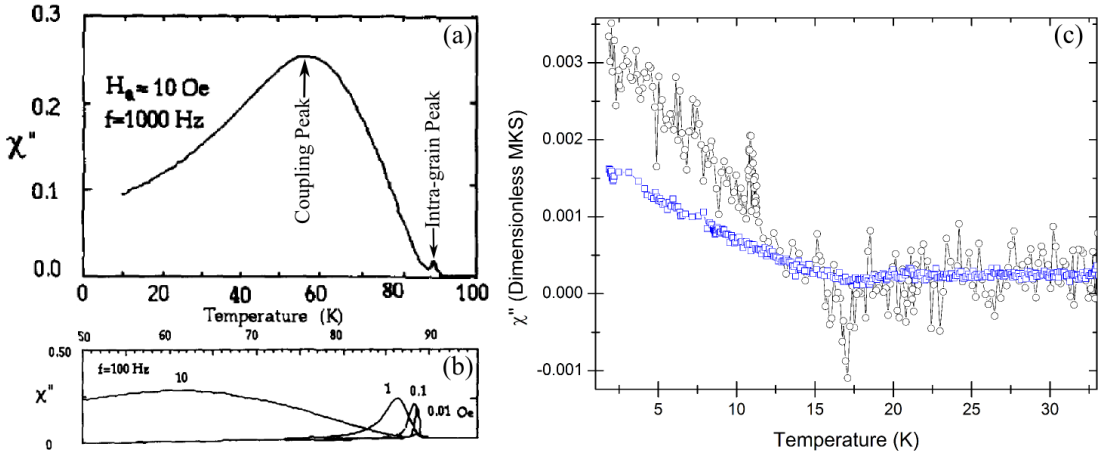

Figure 4.6 *Temperature dependent imaginary susceptibilities from literature[4, 91] of a $YBa_2Cu_3O_{7-\delta}$ cuprate superconductor illustrating (a) the coupling and intra-grain peaks and (b) temperature shift and broadening of the coupling peak under different AC field amplitudes. Measurements of our LSCO sample at 573 Hz (c) illustrates a shallower gradient under 5.6 Oe (blue squares) compared to 2.8 Oe (black circles) consistent with coupling peak broadening.*

4.3 Ambient Pressure Electrostatic Doping

4.3.1 Device Preparation and Experimental Setup

Due to the thin nature of EDLs formed only the top ∼1 nm of a sample will be electrostatically doped, resulting in a very small observable signal. Thus an EDLC device was constructed utilising the larger design 1 susceptometer in order to maximise the sample space, allowing for more material on the device electrodes and hence a stronger detectable signal.

As with Kasahara's EDLC[16], electrodes were constructed from aluminium foil with platinum wires soldered to them to provide electrical connection exterior to the susceptometer. Foil dimensions were chosen to fit within the secondary coil volume while also attempting to maximise total surface area in order to increase the amount of available material for doping. Lead-tin solder was employed in the initial devices and the superconducting transitions for both of these elements were readily evident in the measurement signal. Silver paint was also trialled but this proved too fragile resulting in loss of electrical connection to the foils. Finally bismuth was settled on as a robust solder with no observable superconducting transition. Solder joins were also sealed with a small amount of stycast to prevent any dislocation due to poor wetting to the aluminium foil, and to protect them from electrochemical reactions with the ionic liquid. The working electrode is prepared following the procedure outlined by Kasahara in order to ensure optimal electrical connection between the aluminium foil and our LSCO material, as well as efficient charge accumulation[16]. A conductive slurry consisting of polycrystalline LSCO powder (80 wt %), acetylene black conductive agent (5 wt %) and polyvinylidene difluoride binder polymer (15 wt %) mixed with a 1:1 ratio of N-methylpyrrolidone (NMP) and N,N-dimethyl-formamide (DMF) is coated onto the aluminium foil of the working electrode. The DMP & NMP is then evaporated by drying the foils at ∼100°C for 12 hours. As can be seen in Figure 4.7 both foils are rolled and fed into the susceptometer aligning the working and counter electrodes within each of the secondary coils.

Aligning the electrodes within the counterwound secondary coils should also allow for maximum cancellation of any induced magnetisation from the aluminium foils, platinum wire and bismuth solder resulting in a voltage attributable primarily to our LSCO sample. Of course the positions and precise shape of the

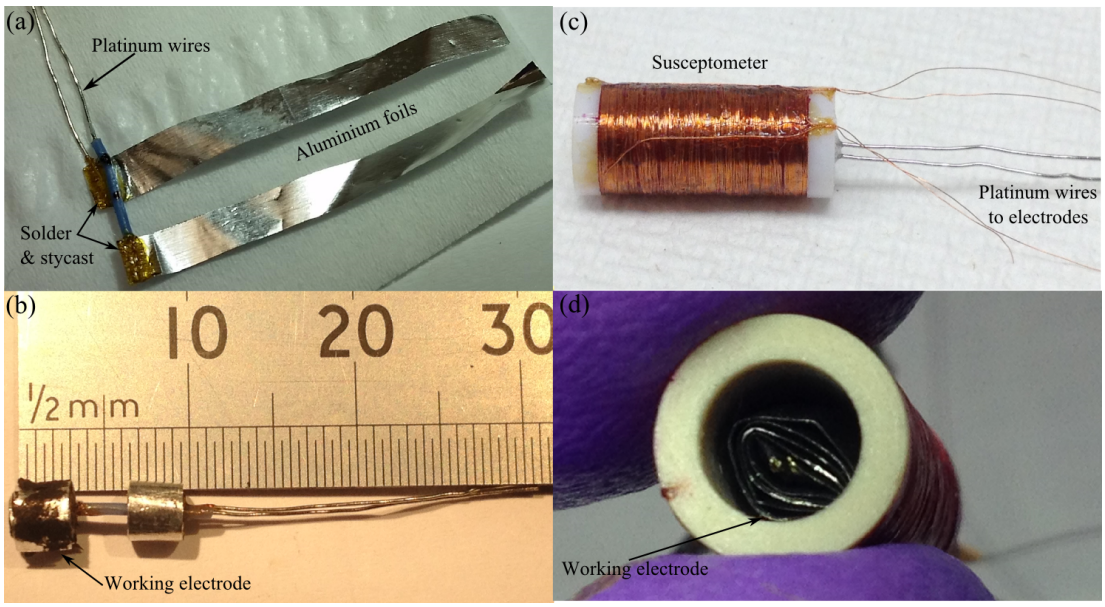

Figure 4.7 *Construction process of a EDLC device featuring (a) identical aluminium foils with platinum wires, (b) rolled foils with working electrode coated in LSCO material, (c) electrodes fed into susceptometer with platinum wires allowing connection to them and (d) working electrode visible within susceptometer bore.*

rolled electrodes may differ slightly between the secondary coils, so while total cancellation is unlikely the majority of these contributions should be accounted for. It should also be noted that whilst bismuth solder on the electrodes removed any superconducting transition from our measured signal there is still a noticeable superconducting transition from the lead solder joins to our secondary coil.

The susceptometer internal cavity is filled with the ionic liquid DEME-TFSI in order to facilitate the electrostatic doping and sealed with a nitrile rubber membrane for ambient pressure measurements. The field provision and measurement setup is identical to that described above for AC susceptibility measurements on the LSCO compound. A Keithley 6517A electrometer is used to provide the voltage between our electrodes and reduce the possibility of any circuit leakage currents. Temperature dependent measurements of this EDLC are taken in a helium gas closed cycle refrigerator with a base temperature of 1.8 K. Any alteration of the voltage across electrodes once at base temperature requires warming the cryostat to ∼220 K to melt DEME-TFSI from its glass phase, allowing ions to become mobile and waiting ∼30 minutes before cooling the system once more. This method allows effective reformation of EDLs and has been shown to maximise the electrostatically induced carrier density over voltage application at other temperatures[25]. Such a procedure is time consuming requiring approximately

a day to warm and cool our large bore cryostat in order to alter applied voltages, thus creating a bottleneck in measurements.

4.3.2 Skin Effect of Aluminium Plates

Whilst the majority of magnetic signal from the electrodes is likely canceled by our counterwound secondary coils there still remains a remnant magnetisation, which provides an additional background to the measurement signal. Measurements of uncoated electrodes inserted into our susceptometers has revealed there is minimal contribution from these at higher temperatures yet becomes more appreciable as the temperature falls. Such behaviour is consistent with the skin effect discussed in Section 2.2.8.

For a given frequency the skin depth of a metallic material (such as the aluminium, platinum and bismuth solder components of the electrodes) decreases as temperature falls due to the falling resistivity, as shown by Equation 2.17. Once this skin depth becomes comparable to the dimensions of a material screening of the flux penetrating begins to take place, yielding a diamagnetic signal which grows as the skin depth continues to shrink. Figure 4.8 illustrates how measurements of uncoated electrodes within our susceptometer resemble precisely this behaviour when compared to measurements of an aluminium foil (the chief component of our electrodes) measured in a SQUID magnetometer. Direct comparison is not possible due to the combination of components within the electrodes along with partial cancellation of their signal from our counterwound secondary coils. The skin effect is also dependent on the frequency of the applied

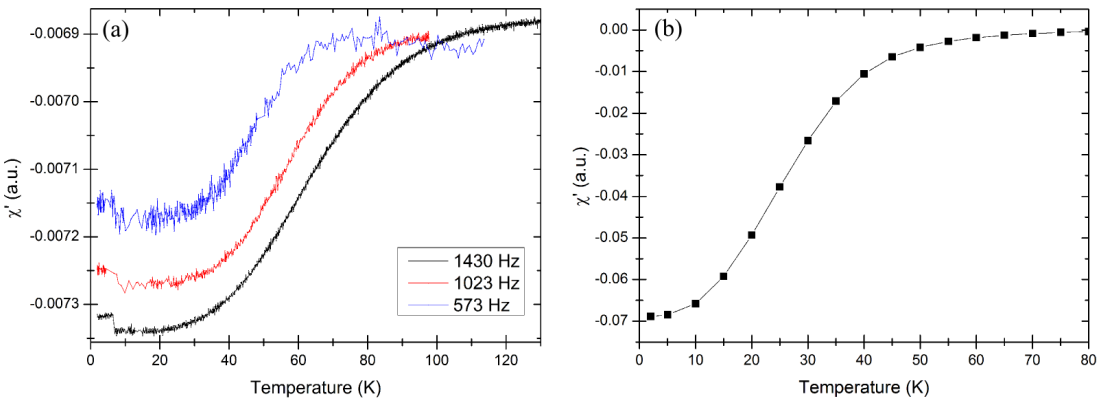

Figure 4.8 *Real susceptibility of (a) electrodes measured within our susceptometer at frequencies listed and (b) an aluminium foil sample measured in a SQUID magnetometer.*

AC field with lower frequencies yielding a larger skin depth. As such lower frequencies result in onset of screening currents and their associated diamagnetism at lower temperatures as can be seen in Figure 4.8 (a), further corroborating the source of this signal as the skin effect.

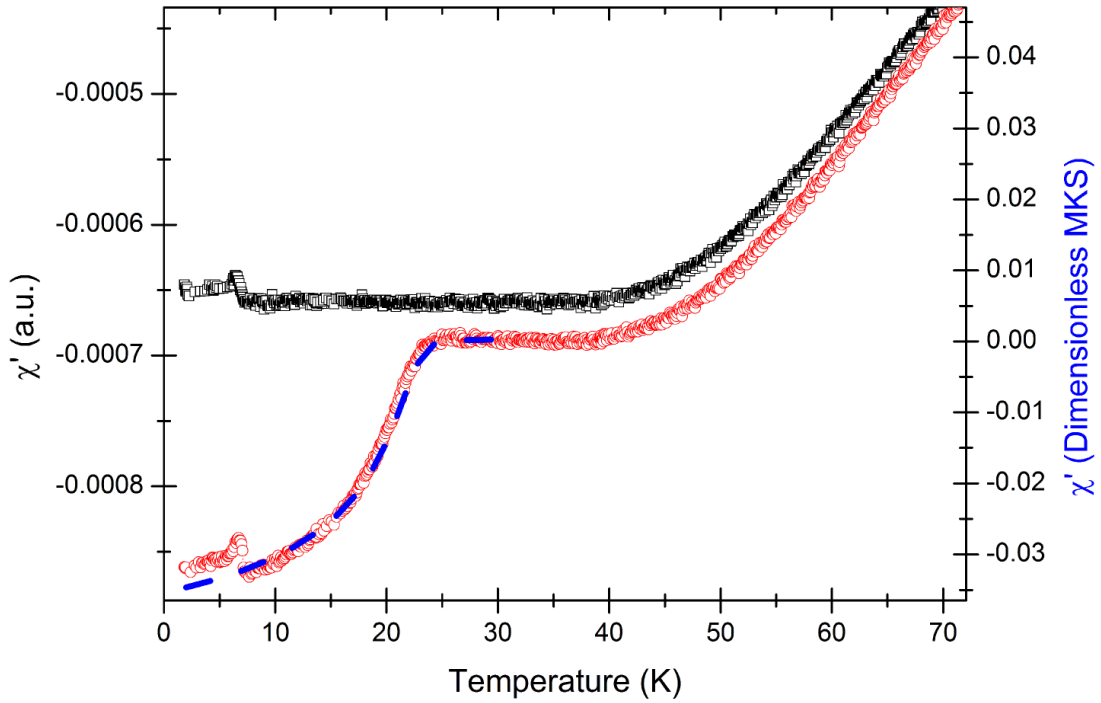

Figure 4.9 *Real susceptibility of the bare electrodes (black squares) and with the working electrode coated in LSCO material (red circles). Superconductivity signal of LSCO material (blue dashed line, right axis) measured in a SQUID magnetometer overlaid to illustrate detection of LSCO coating.*

The additional background from the skin effect on the electrodes is minimised through use of the thinnest aluminium foils possible, reducing the temperature at which screening occurs as well as the magnitude of the diamagnetic signal. The majority of our EDLC devices employ 0.02 mm thick aluminium foil in their electrode construction allowing for maximum measurement sensitivity. As can be seen in Figure 4.9 the superconducting signal from a LSCO coating on the working electrode is still clearly discernible even with the electrode background unaccounted for. Also observable is a small transition at ∼7.2 K which is attributed to the onset of superconductivity in the lead based solder of the secondary coil connections altering the environment near the coil. Application of a DC field suppressed this transition confirming this. Susceptibilities are listed in arbitrary units as it is not possible to determine a precise calibration constant experimentally due to the partial cancellation of electrode signals, as well as the spiral shape of the LSCO coating distributed across the working electrode.

4.3.3 Component AC Contributions

Measurements of the AC susceptibility in our EDLC device combine contributions from a number of sources; the small imbalance of the coil background, the electrodes, the LSCO coating and the ionic liquid itself. The AC response of each of these components can be separated in order to provide information on which contributes the most appreciable signal and how these vary across temperature, as can be seen in Figure 4.10. The coil background (b) and uncoated electrode

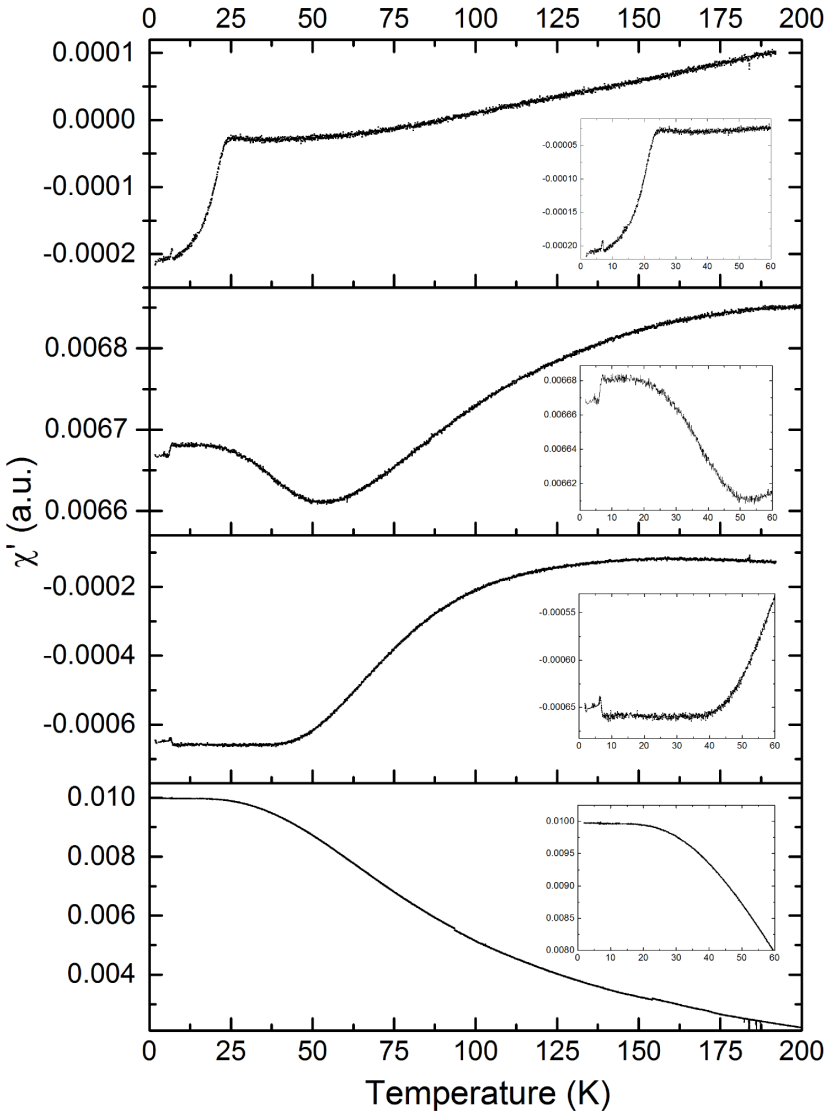

Figure 4.10 *Real AC susceptibility response of each individual EDLC component for (a) LSCO coating, (b) empty susceptometer background, (c) bare uncoated electrodes and (d) ionic liquid DEME-TFSI to illustrate their unique temperature dependence. Susceptibilities are in arbitrary units calculated based solely on field and frequency of measurement to provide accurate comparison. Insets feature the 2 - 60 K range we primarily are interested in.*

(c) responses are relatively large but vary in a consistent manner which can be accounted for. Indeed subtraction of these backgrounds from a coated electrode measurement allows resolution of the LSCO superconducting transition of (a). There remains a small residual background which can be seen in the normal state up to 200 K, yet this is likely due to slight differences in the electrode positions within our susceptometer altering the background between the uncoated/coated measurements. The highly polar ionic liquid DEME-TFSI within our EDLC devices contributes the most significant signal to our measurement as seen in (d). As DEME-TFSI fills both of the counterwound secondary coils the observable signal is in fact the unbalanced signal remaining from cancellation implying that DEME-TFSI has an even larger AC response. However, even with this larger background the LSCO transition is still just as discernible as can be seen in Figure 4.11 (a).

4.3.4 Electrostatic Doping

Measurements of an EDLC with 0 V applied between the electrodes are subtracted from measurements under voltage in order to resolve the electrostatic doping effect. An EDL will only dope ∼1 nm of the polycrystalline LSCO coating and thus the shifted T_c will only occur in a very small volume of the total material. Subtraction of a 0 V measurement will resolve this small volume of doped material by removing the bulk superconducting signal, as well as accounting for background signals from the susceptometer, electrodes and ionic liquid. Measurements under a range of applied voltages were run on many EDLC devices at several frequencies and AC fields of ∼2.82 & 5.64 Oe.

Due to the likely very small signal to be detected from electrostatic doping we have primarily focused on identifying the superconducting transition from the much stronger χ', which will be more easily resolvable. Figure 4.11 (b) shows 0 V corrected χ' measurements at 1430 Hz and 5.64 Oe for various applied voltages. On the initial warm at 1 V the EDL remains frozen along with DEME-TFSI until ∼220 K and thus an essentially flat signal is recovered. For further cooling measurements there appears to be a small superconducting transition shifting with applied voltage, as would be expected from electrostatic doping. This is a subtle change and is not observable at the lower frequencies and fields measured where the signal to noise ratio is much lower. The superconducting volume fraction has been estimated based on the magnitude of this transition

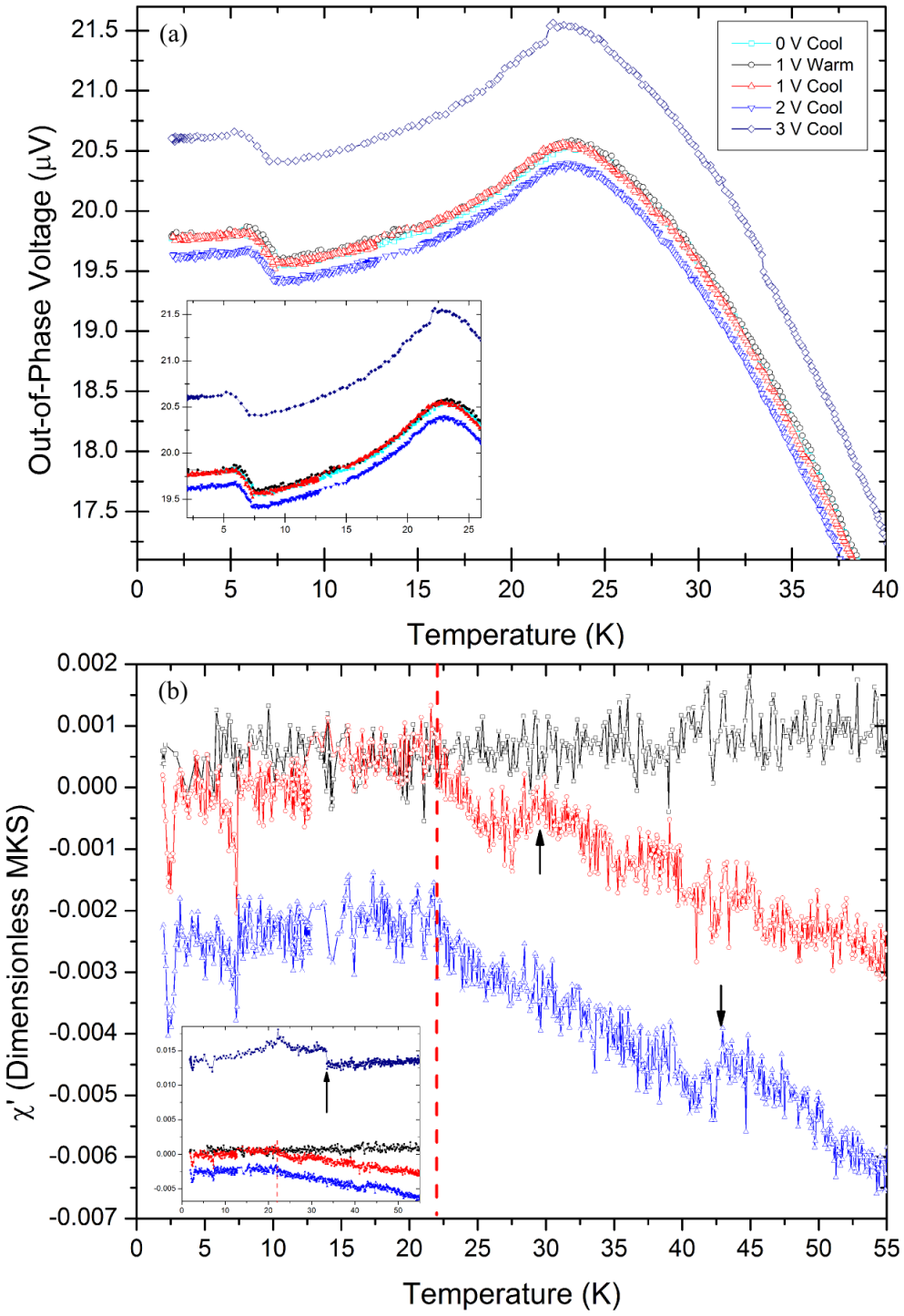

Figure 4.11 *(a) Temperature dependent unaltered out-of-phase voltage signal from LSCO EDLC for various applied voltages under 1430 Hz and 5.64 Oe with zoomed inset and (b) 0 V corrected measurements converted to χ' for 1 V warm (black squares), 1 V (red circles) and 2 V (blue triangles) cools. Arrows indicate proposed onset of electrostatically induced superconductivity shifting under different applied voltages. Red dashed line indicates bulk superconducting T_c. Inset illustrates 3 V measure where appreciable background change has occurred yet possible superconductivity shift is still evident.*

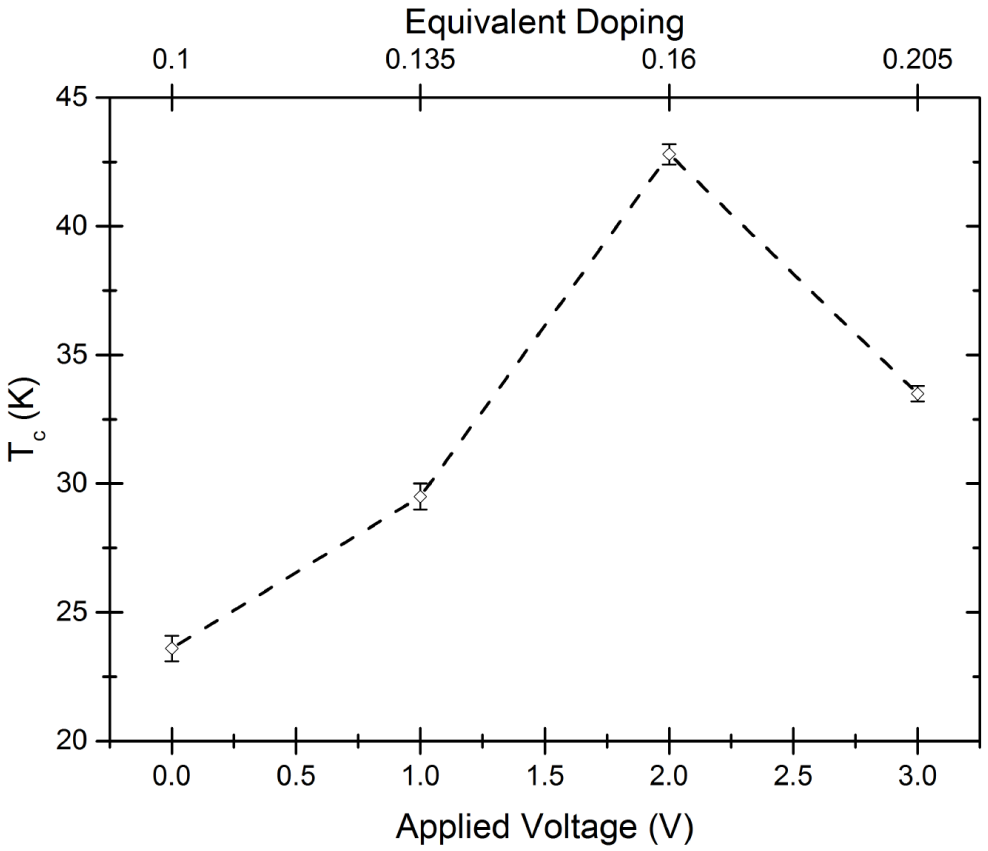

Figure 4.12 *Phase diagram for electrostatically doped superconductivity observed in $La_{1.9}Sr_{0.1}CuO_4$ coated EDLC correlated with equivalent La doping concentrations from literature[84, 85].*

in relation to the bulk superconductivity and yields a value of ∼0.16%, which is consistent with induced superconductivity from EDLC devices in literature[16]. The associated T_c of these superconducting transitions against applied voltage has been plotted to give an electrostatically doped phase diagram in Figure 4.12, and correlated to equivalent chemical doping concentrations from literature. A dome of superconductivity seems evident similar to that shown in Figure 4.1 (b), as well as a maximum T_c ∼42.8 K being observed which agrees with values expected for optimal doping of this material[85].

A change of the normal state is also evident in Figure 4.11 (b), where above the bulk material T_c a more paramagnetic signal is observed possibly as a result of the electrostatic doping. Kasahara's EDLC similarly does not always recover the same normal state response under electrostatic doping as shown in Figure 1.8. However, as can also be seen in the inset of Figure 4.11 (b) under 3 V the background appears to change markedly; a small superconducting transition still appears to be present yet must be treated with some scepticism in light of the altered background. Potentially these changes may be due to the AC response of

the highly polar ionic liquid (which has an appreciable contribution) changing as it is subjected to voltage, as the background has already shifted somewhat under 2 V. Such a voltage dependence could be a result of local density changes of the ionic liquid near electrodes as it is polarised, and possibly a contributing factor to the supposed normal state change seen in our measurements. The significant background change could also be attributed to possibly exceeding the EDLC's limiting voltage and causing electrochemical reactions between the electrodes and DEME-TFSI, leading to degradation of the device. The bias across the EDLC was returned to 0 V yet the same background magnitude as found in the original measurement was not recovered. Additionally, repetition of the 1 V bias was attempted and whilst the normal state change was recovered the small superconducting transition was not. Both of these results seem to support the possibility of irreparable change to the device from an electrochemical reaction compromising its operation.

Further measurements were attempted with several other EDLC devices utilising new electrodes and LSCO coatings while keeping voltages low in order to prevent possible electrochemical degradation. Alteration of the normal state was reproduced as before with a shift towards paramagnetic behaviour, but consistent superconductivity transitions were not evident. Application of initial voltages seemed to induce a possible weak superconducting transition as shown in Figure 4.13, yet this was not discernible for following voltages even after averaging numerous temperature sweeps to improve the signal to noise ratio. The background also appeared to shift consistently between voltage applications as seen in the inset.

A possible explanation for these issues may be that the method of sealing our EDLC is not as robust as believed and leakage of the ionic liquid has occurred between measurements. Warming of our EDLC in order to change the bias voltage would melt the ionic liquid from its glass phase, allowing leakage to occur if our device seal is poor. As a result the background signal would indeed change between voltage applications due to the consistent loss of the the DEME-TFSI dielectric. Loss of DEME-TFSI could also have resulted in the loss of superconductivity induced by electrostatic doping by compromising the formation of EDLs through lack of a dielectric. Potentially this could explain the loss of induced superconductivity as voltage is swept higher, and the inability of a device to reproduce superconductivity shifts induced previously at the same voltage. Careful examination of the latest devices tested did indeed indicate leakage of

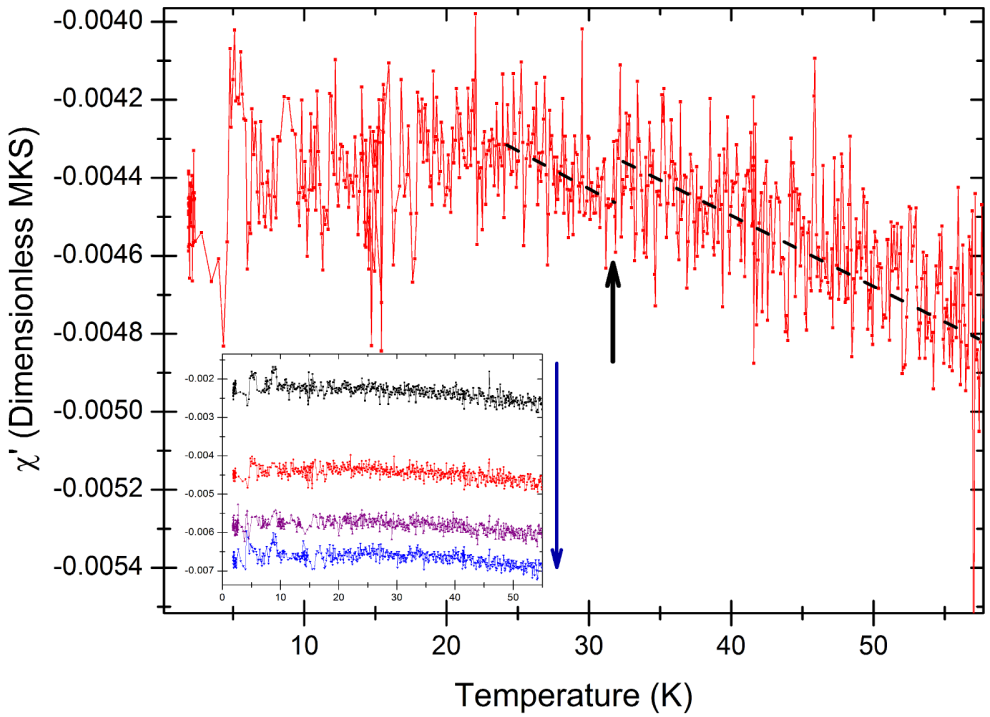

Figure 4.13 *Arrow indicates possible weak superconducting transition for 1 V electrode bias in LSCO EDLC with dashed lines indicating the altered normal state. Inset illustrates consistent shift of background with navy arrow indicating voltage increase between measurements from 0.5 - 2 V in 0.5 V steps.*

the ionic liquid corroborating this as a likely source for these issues.

It should be noted however that recent experimental evidence has emerged in literature suggesting doping may be due to electrochemical means rather than electrostatic, casting doubt on the validity of EDL device operation. Notably, examples of ionic liquid gated EDL devices with oxides such as VO_2[93], TiO_2[94] and $SrTiO_3$[95] have been shown to alter the doping depending on exposure to an oxygen atmosphere, indicating oxygen vacancy creation; sometimes causing irreversible changes even on removal of the dielectric[93]. Irreversible behaviour has even been observed in EDL devices of the high temperature superconductor $YBa_2Cu_3O_{7-x}$, and has been attributed to possible electrochemical reaction with the ionic liquid causing oxygen depletion of the CuO_2 planes[96]. Potentially such electrochemical reactions may arise from low energy barriers to oxygen vacancy formation in these materials, yet even so there have been inconsistencies between studies as to whether this occurs only at higher gate voltages or not[97]. Precluding the possibility of fully reversible electrochemical reactions from pure electrostatic is also difficult[98]. The occurrence of electrostatic versus electrochemical doping appears to depend greatly on the material in question and

its redox stability to the ionic liquid as much as anything else[97]. Indeed recent work has shown that $La_{0.5}Sr_{0.5}CoO_{3-\delta}$ in fact exhibits electrostatic doping under negative voltage bias and irreversible electrochemical reaction under positive bias, illustrating oxide behaviour may be very complex in EDL devices[97]. Thus the changing backgrounds and lack of repeatability in our LSCO devices may be attributable to such electrochemical reactions. In order to identify this issue careful voltage studies should be performed on devices in absence of the aforementioned potential leakage.

4.4 Conclusions

EDLC devices have been constructed capable of measuring the AC susceptibility response of our synthesised $La_{1.9}Sr_{0.1}CuO_4$ superconductor to the same degree as a SQUID magnetometer. Superconductivity has potentially been induced by our devices through electrostatic doping, shifting the critical temperature as high as the optimal doping for LSCO as well as altering the normal state response. However, individual EDLC devices failed to perform consistently in the later stages of each experiment which has been attributed to poor sealing resulting in the loss of the DEME-TFSI dielectric. This issue can however be overcome by sealing EDLC devices within a piston cylinder pressure cell for pseudo-ambient pressure measurements. Such a setup would prevent any leakage and allow greater reproducibility of results, as well as providing the same experimental conditions for accurate comparison to further measurements under pressure. However time constraints and equipment availability prevented completion of these further measurements and thus this remains as future work to be carried out. Electrochemical reactions impairing device operation are also a possibility and a careful voltage study in absence of leakage should assist in determining this. The voltage dependence of the ionic liquid DEME-TFSI with uncoated electrodes should also be investigated as this may be a contributing factor altering its appreciable background response.

Chapter 5

AC Susceptibility of Single Chain Magnet

Single chain magnets (SCM) are an interesting class of material, exhibiting superparamagnetism and long relaxation times at low temperatures; making them promising candidates for high-density memory storage applications[99]. To date only minimal investigation into the effect of pressure on certain examples of these one-dimensional (1D) materials has been performed, although results suggest improved SCM behaviour with longer relaxation times[100, 101]. Thus AC susceptibility measurements are carried out on the co-ordination polymer SCM $[Co(NCS)_2(pyridine)_2]_n$ for the first time, using our constructed susceptometers in piston cylinder cells in order to determine the effect of pressure on its magnetic relaxation times and spin reversal activation energy barrier.

5.1 Single Chain Magnet Review

Single chain magnets (SCM) are comprised of isolated one-dimensional (1D) chains exhibiting such slow magnetic relaxation that at low temperatures they are considered magnetic without any applied field[102]. Indeed they are closely related to the zero-dimensional single molecule magnets (SMM) that also exhibit magnetic hysteresis, slow relaxation, and superparamagnetism below a blocking temperature T_B[102, 103]. A superparamagnet can be magnetised under a field to a much greater degree than conventional paramagnets due to single

magnetic domains exhibiting large magnetic moments. The relaxation time for these moments grow longer as temperature falls, leading to them eventually displaying permanent magnet-like behaviour. Such properties thus make these materials promising candidates for high-density memory storage and electronics applications[99].

SCMs are a relatively new class of material observed experimentally for the first time in 2001[104], even though Glauber predicted such behaviour by modeling 1D Ising spins in 1963[105]. In order for a material to exhibit SCM behaviour it must have a large uniaxial magnetic anisotropy and strong magnetic coupling of spins along the chain (J), in order to allow magnetisation of molecular chains resistant to quick relaxation. Notably interchain interactions must also be minimal to prevent disruption of individual chain behaviour[3, 102]. Characterisation of a SCM must be made through both the static and dynamic magnetic properties in order to distinguish it from similar systems such as spin glasses[103]. In the static case the anisotropic Heisenberg chain model is generally applied described by the Hamiltonian

$$H = -2J \sum_{-\infty}^{+\infty} S_i S_{i+1} + D \sum_{-\infty}^{+\infty} S_{iz}^2 \tag{5.1}$$

Where S_i depicts a magnetic spin in the chain, D accounts for the magnetic anisotropy of single ions and S_{iz} is a spins projection onto the materials easy magnetic axis[102]. A length scale ξ_c defines correlation of spins along the chain and grows exponentially larger as the temperature falls, giving rise to domains of oriented spins separated from oppositely oriented domains by narrow walls of anti-parallel spins. Ideally the length of a chain is infinite, however in real systems the occurrence of defects defines finite chain segments of average length $\langle L \rangle$. At high temperatures when $\xi_c \ll \langle L \rangle$ the chain can still be considered infinite, whereas in the low temperature regime $\xi_c \gg \langle L \rangle$ the chain acts as finite segments[102, 103]. In a 1D system described by the anisotropic Heisenberg model χT is proportional to ξ_c and thus the susceptibility is given by

$$\chi T / C_{eff} \approx exp(\Delta_{\xi_c} / k_B T) \tag{5.2}$$

Where C_{eff} is the effective Curie constant, k_B is the Boltzmann constant and Δ_{ξ_c} is the energy cost to create a domain wall along the chain. Thus plots of $ln(\chi T)$ versus $1/T$ should produce a linear region with slope of Δ_{ξ_c}/k_B if a system exhibits such 1D behaviour with significant magnetic anisotropy. Experimentally DC and

low frequency AC measurements are often employed to confirm this static case. In the Ising limit, characterised by narrow domain walls, this energy can be related to the magnetic interaction of spins by[99, 102]

$$\Delta_{\xi_c} = 4JS^2 \tag{5.3}$$

The dynamic behaviour of a SCM is primarily investigated via the temperature dependence of the relaxation time. At finite temperatures spin flipping in chains is possible through thermal activation, and decay of the magnetisation occurs over a relaxation time τ which may be described by the Arrhenius law

$$\tau(T) = \tau_0 e^{E_a/k_B T} \tag{5.4}$$

Where τ_0 is the characteristic flipping time of spins in the system and E_a is the activation energy barrier of spin reversal. In systems characterised by the anisotropic Heisenberg model the activation energy is actually comprised of two energy barriers, representing the available spins to flip. Δ_{ξ_c} is the energy required to create a domain wall within the chain and Δ_A is that necessary to flip a spin within a domain wall without any spin interaction ($\Delta_A = DS^2$). Thus the activation energy barrier at high temperatures characterised by infinite chains is

$$E_a = 2\Delta_{\xi_c} + \Delta_A \tag{5.5}$$

Whereas for finite chains in the low temperature regime

$$E_a = \Delta_{\xi_c} + \Delta_A \tag{5.6}$$

A lower energy is required in the latter case as the ends of segments require less energy to flip due to only one neighbouring spin[3, 102]. AC susceptibility measurements are used to monitor the system response from small perturbations around equilibrium in order to determine the temperature dependent relaxation time. As τ varies with temperature it will eventually coincide with the driving AC oscillation frequency, $\tau = 1/2\pi f$, giving rise to maximum dissipation evidenced by a peak in the imaginary susceptibility χ''. Thus temperature dependent measurements at a range of frequencies allow determination of $\tau(T)$ based on shifting χ'' peaks. Below such peaks the moments are unable to follow the AC field oscillation, due to the slower relaxation time, and the measured AC signals decrease.

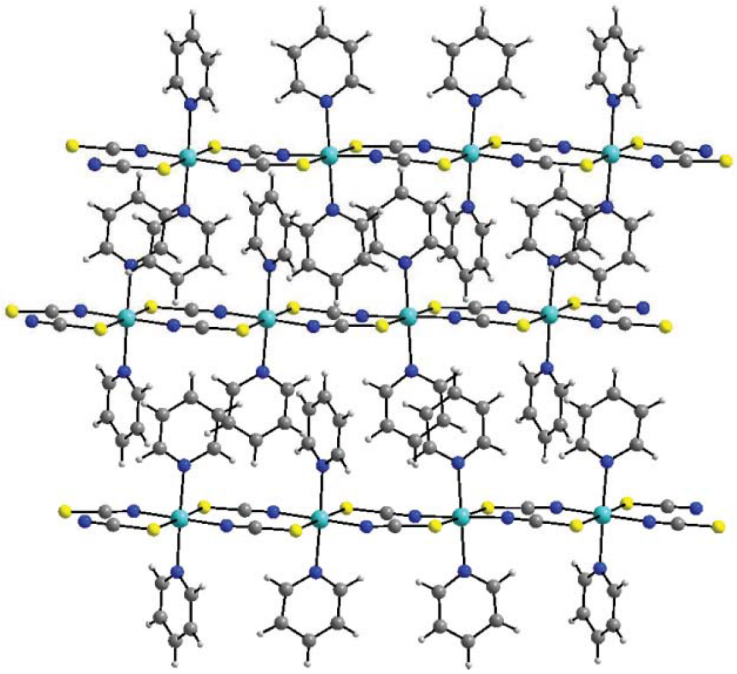

Figure 5.1 *Several $[Co(NCS)_2(pyridine)_2]_n$ polymer chains (chain direction horizontal) packed alongside each other displaying their structure comprised of Co (aqua), N (blue), S (yellow), C (grey) and H (light-grey) atoms[106].*

SCMs exhibiting very long relaxation times and high activation barriers against spin reversal are most desirable for technological applications. Thus, much research has been conducted in recent years into design of SCMs, with 1D co-ordination polymer compounds proving to be a particularly useful class of material. Co-ordination polymers usually consist of inorganic polymer structures containing metal cation centres, featuring organic ligands to keep individual chains separated. One such co-ordination polymer $[Co(NCS)_2(pyridine)_2]_n$ is shown in Figure 5.1 where Co metal cations are bridged by short thiocyanato anions (SCN^-) allowing for magnetic interaction along the chain. Co-ordinated pyridine ligands also assist in keeping chains separated from one another and reducing the possibility of interchain interactions[106].

AC susceptibility measurements were performed on $[Co(NCS)_2(pyridine)_2]_n$ by Boeckmann and confirmed the existence of SCM behaviour. Figure 5.2 illustrates the existence of frequency dependent peaks in the real and imaginary susceptibilities at low temperature characteristic of a SCM. The peak maximum in χ'' indicates the AC field oscillation coinciding with the systems relaxation time at that particular temperature, as discussed above. Thus Boeckmann determined $\tau(T)$ for this material over the investigated range and fitting this data to the Arrhenius law of Equation 5.4 calculated an activation energy barrier of $E_a/k_B =$

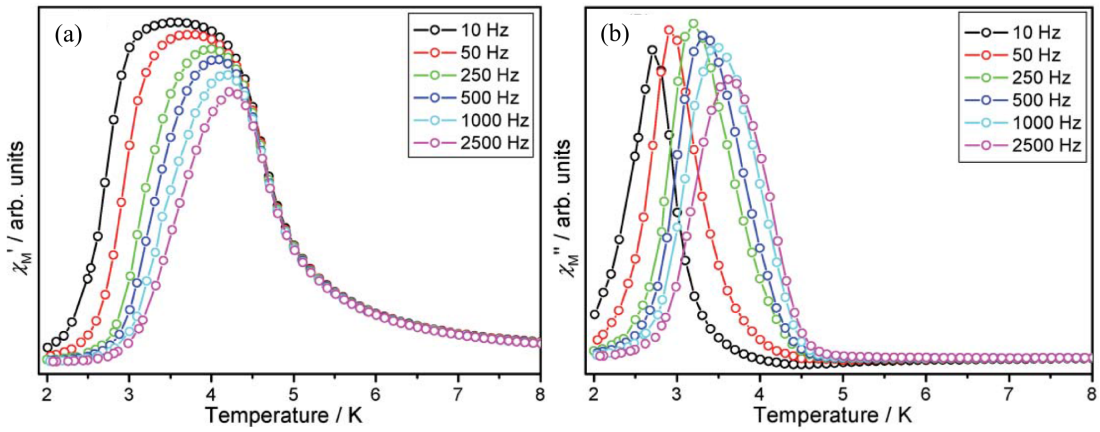

Figure 5.2 *Temperature dependence of the (a) real and (b) imaginary susceptibilities at the listed frequencies in the co-ordination polymer $[Co(NCS)_2(pyridine)_2]_n$ displaying frequency dependent peaks characteristic of a SCM[106].*

62.5 K and $\tau_0 = 2.02 \text{ x } 10^{-12}$ s consistent with similar SCM systems[106].

The degree to which maxima shift with frequency can also be used to distinguish between different systems. In particular spin glasses exhibit very small shifts with frequency allowing differentiation from superparamagnets, where shifts are more pronounced, through the empirical Mydosh parameter given by[3, 107, 108]

$$\varphi_M = \frac{\Delta T_p}{T_{p,min}\Delta(log f)} \tag{5.7}$$

Where T_p is the temperature of the χ'' peak, $T_{p,min}$ is the lowest temperature peak and f the frequency. The AC data collected by Boeckmann yielded a $\varphi_M = 0.12$ for $[Co(NCS)_2(pyridine)_2]_n$ which lies within the expected range of a superparamagnet, $0.1 < \varphi_M < 0.3$, and is an order of magnitude greater than those determined for spin glasses (typically $\sim$0.01[3, 107]) thereby discounting these systems[3, 106, 108].

To date there has been minimal investigation into SCM systems under pressure, with the most notable work being carried out by Mito. Mito conducted AC susceptibility measurements with a SQUID magnetometer on several structural configurations of a Manganese based single chain magnet within a piston cylinder cell. Pressure was found to increase the energy activation barrier resulting in longer relaxation times and higher onset temperatures of SCM behaviour; which Mito attributes to improved ferromagnetic interaction of spins[100, 101]. Thus similar improvements may also be exhibited in the SCM magnet system $[Co(NCS)_2(pyridine)_2]_n$ when subjected to pressure.

5.2 Characterisation

Samples of the co-ordinated polymer $[Co(NCS)_2(pyridine)_2]_n$ have been synthesised and provided by the Murrie Research Group of the University of Glasgow. Comparison to certain experimental results on similar samples carried out by this group are occasionally referred to throughout this chapter.

A pellet of $[Co(NCS)_2(pyridine)_2]_n$ was prepared of diameter 1.8 mm and length 2.5 mm as shown in the inset of Figure 5.3 (b). Temperature dependent measurements in a SQUID magnetometer were performed along the central axis of this cylinder in order to provide an ambient pressure characterisation of its behaviour. Figure 5.3 (a) displays the temperature dependent χT determined from DC magnetisation measurements under a 1000 Oe field. χT decreases with temperature down to ∼35 K, as seen in the inset, which has been attributed to antiferromagnetic interactions[106] before climbing to a maximum at ∼3.9 K. Below this maximum a sharp fall is seen suggestive of a transition to ferromagnetism and saturation of χ. A field dependent DC measurement at 2 K is shown in Figure 5.3 (b) confirming the ferromagnetic behaviour with minimal hysteresis in this temperature regime. Such behaviour is consistent with that seen in literature for this compound[106].

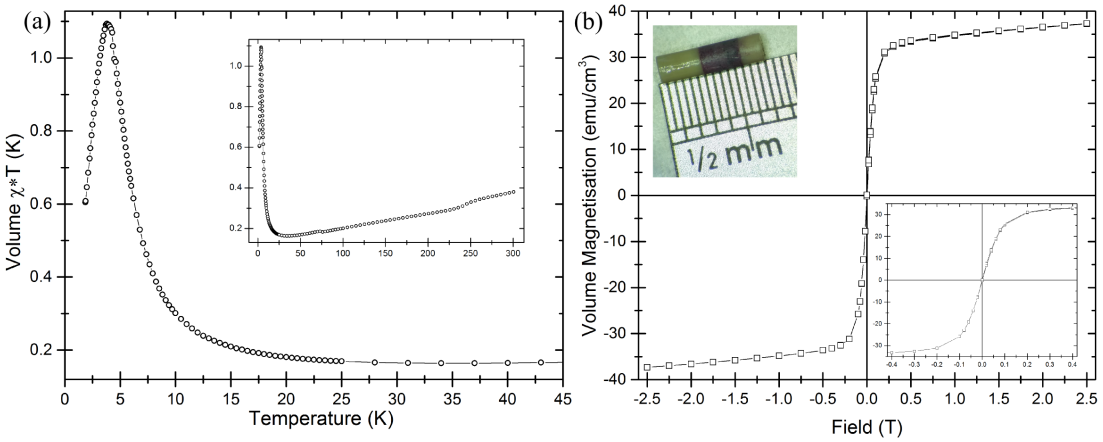

Figure 5.3 *(a) DC volume χT of $[Co(NCS)_2(pyridine)_2]_n$ measured on SQUID magnetometer illustrating a maximum at ∼3.9 K as a potential transition to ferromagnetic behaviour. Inset displays decreasing values down to ∼35 K indicating antiferromagnetic interactions as seen in literature previously[106]. (b) DC magnetisation field sweep at 2 K illustrating saturation and providing further evidence for ferromagnetic behaviour. Insets feature cylindrical sample (upper left) and minimal hysteresis of field sweep (lower right).*

Temperature dependent AC susceptibility measurements under zero DC field were performed on the sample at a range of frequencies to investigate its dynamic behaviour and are shown in Figure 5.4. A clear frequency dependence of broad peaks is evident below ~4 K in both χ' and χ'' which is indicative of SCM behaviour as observed previously in literature[106]. Calculation of the Mydosh parameter from Equation 5.7 yields $\varphi_M = 0.081$, which is similar although somewhat lower than the 0.12 value determined by Boeckmann[106]. Regardless, this value indicates our sample is on the edge of the superparamagnetic regime and is larger than that found in typical spin glass systems[3].

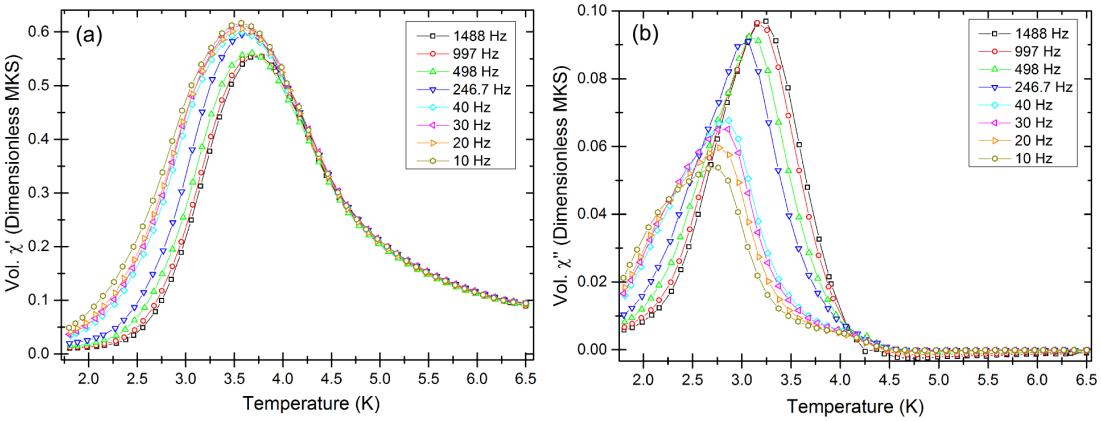

Figure 5.4 *(a) Real and (b) imaginary AC susceptibility measurements on a SQUID magnetometer of $[Co(NCS)_2(pyridine)_2]_n$ at ambient pressure under a 3 Oe AC field amplitude and various listed frequencies (not all frequencies measured shown for clarity).*

In order to confirm the SCM behaviour the DC and low frequency AC (1 Hz) susceptibility measurements are plotted as $ln(\chi'T)$ versus $1/T$ as shown in Figure 5.5 (a). In this static case if the system possesses uniaxial magnetic anisotropy characteristic of a SCM, then it can be described by the anisotropic Heisenberg chain model as discussed in Section 5.1, and should display a linear regime[99, 102]. Such a linear regime is evident confirming the 1D anisotropic nature of $[Co(NCS)_2(pyridine)_2]_n$ and fitting Equation 5.2 to this yields a domain wall creation energy of $\Delta_{\xi_c}/k_B = 11.96$ K which matches that observed by the Murrie group on similar samples[109]. As $\chi'T$ is directly proportional to the correlation length ξ_c the observed maximum and linear decrease above this (along with falling temperature) is consistent with ξ_c growing larger than the mean separation of defects along the chain, indicative of the finite chain regime[99].

The dynamic behaviour of SCM systems can be determined from the evolution of the relaxation time with temperature as discussed in Section 5.1. The relaxation times at the temperatures of χ'' peaks may be determined from the applied

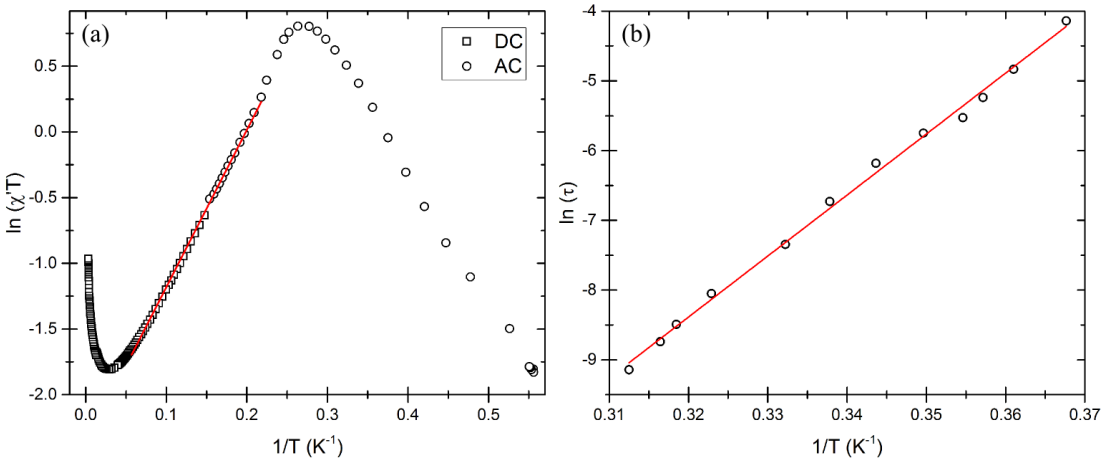

Figure 5.5 *(a) $\chi'T$ for AC (1 Hz, circles) and DC (squares) susceptibility measurements fitted to anisotropic Heisenberg behaviour in the linear regime (red line). (b) Arrhenius plot of relaxation times determined from χ'' peak temperatures fitted to the Arrhenius law of Equation 5.4 (red line).*

frequencies and fitted to the thermally activated Arrhenius law for spin reversal of chains. Figure 5.5 (b) illustrates relaxation times determined in this manner from AC measurements and plotted as $ln(\tau)$ versus $1/T$ producing a linear fit to Equation 5.4. Fit to the Arrhenius law is consistent with SCM behaviour and predicts an energy barrier to macro spin reversal of E_a/k_B = 87.46 K and a τ_0 = 1.5979 x 10^{-16} s for our sample. This E_a is larger than that observed by Boeckmann although the τ_0 is several orders of magnitude smaller[106]. Potentially this discrepancy could be due to differing sample quality although a larger E_a is more beneficial for SCM applications. As we have established we are in the finite chain regime at these temperatures we can use Equation 5.6 and the deduced values for E_a/k_B and Δ_{ξ_c}/k_B to estimate the anisotropic energy barrier Δ_A/k_B = 75.5 K. Δ_A represents the energy necessary to flip a spin within a domain wall in the absence of exchange energy from neighbouring spins, thus providing an indication of the intrinsic magnetic anisotropy of chain ions[102].

5.3 Ambient Pressure Susceptibility Calibration

The same cylindrical $[Co(NCS)_2(pyridine)_2]_n$ sample was placed within a susceptometer of design 2 thus filling almost the entire sensing coil volume to ensure a maximal detectable signal. The susceptometer was mounted on the plug of the 1 GPa piston cylinder pressure cell which was just sealed in order to perform pseudo-ambient pressure measurements.

Measurements are performed on a helium gas exchange closed cycle refrigerator (CCR) with an accessible temperature range of 1.9 - 300 K. As in Chapter 4, a Keithley 6221 AC current source supplied the driving current of the primary coil to generate the AC field; whilst the secondary coil was connected to a Signal Recovery 830 lock-in amplifier triggered by the 6221. No filters were employed in order to avoid dephasing the measured signal. Due to the slight mismatch of the coils the remnant signal from the susceptometer is corrected for by subtraction of measured coil backgrounds at the various frequencies. Temperature dependent AC susceptibility measurements are performed on the SCM sample at the same frequencies used in the above SQUID measurements in order to provide optimal calibration. As in Chapter 4, direct comparison of these measurements allowed for experimental determination of a calibration constant α; in this instance the magnitude of χ' maxima is used. Susceptibility measurements are also corrected for demagnetisation as described in Section 2.2.4.

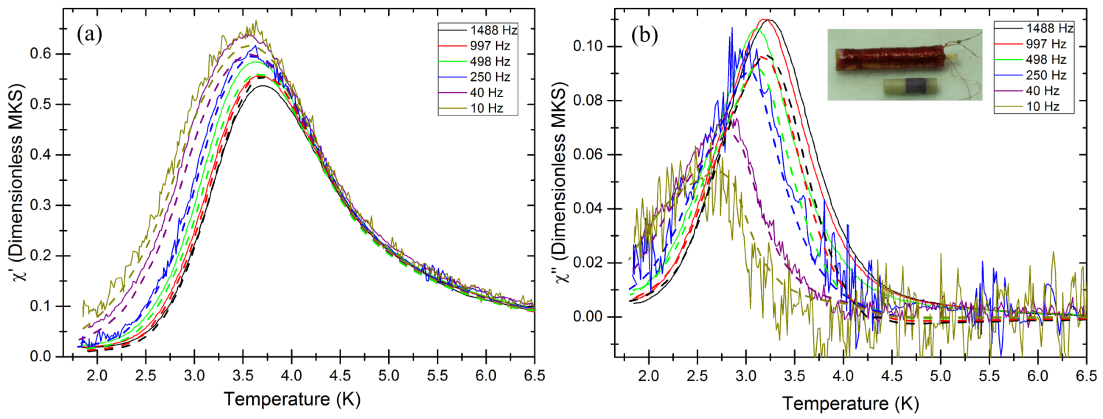

Figure 5.6 *(a) Calibrated real and (b) imaginary AC susceptibilities (solid lines) of $[Co(NCS)_2(pyridine)_2]_n$ in susceptometer at various frequencies (listed) and a 3 Oe AC field amplitude overlaid with SQUID measurements (dashed lines). Inset illustrates sample size in relation to susceptometer used. Note not all frequencies measured have been shown in the interest of clarity.*

Figure 5.6 displays the calibrated AC susceptibility measurements from our susceptometer overlaid with SQUID data. The calibrated measurements tend to fit the SQUID data well at high and low temperatures generally, although some disparity in magnitude is seen in the peak region, most notable in the weaker χ'' signal. Due to the many peaks measured at multiple frequencies the calibration constant α is actually an average value and thus exhibits some uncertainty, primarily due to greater noise on lower frequency measurements. Additionally, a complete background subtraction is not always possible, as the

susceptometer's precise position within the cell cannot be perfectly replicated after unloading and reloading it; leading to a slightly different response. Thus some residual background may remain unaccounted for, contributing toward this magnitude discrepancy. Such error is greatest for low frequency measurements where the background is most appreciable in comparison to signal strength. Nevertheless the calibration provides a fair reproducibility of signal magnitude, yet more importantly the shape and position of the peaks match very well to SQUID measurements with the frequency dependence emerging at $\sim$4 K as seen previously. Determination of the SCM properties is primarily calculated from peak positions which can be accurately established by our susceptometer measurements.

5.4 AC Susceptibility under Pressure

Temperature dependent AC susceptibility measurements at the same frequencies and field were carried out at a range of pressures to investigate development of the SCM behaviour. A sensitive manganin gauge is employed to track the pressure within the cell as discussed in Section 2.1.2. Table 5.1 lists the applied pressure at 300 K and that remaining at base temperature due to pressure medium contraction for each set of measurements. Throughout this section, pressure points are referred to by their low temperature value as SCM behaviour is observed in this regime.

Pressure Step	Pressure at 300 K (GPa)	Pressure at 2 K (GPa)
P0	0.01	0.1 x 10^{-3}
P1	0.31	0.1 x 10^{-3}
P2	0.49	0.10
P3	0.69	0.30
P4	0.81	0.44
P5	0.88	0.51
P6	0.97	0.60
P7	0.1 x 10^{-3}	0.1 x 10^{-3}

Table 5.1 *Applied pressures at 300 K and value at 2 K determined from manganin pressure gauge resistance as discussed in Section 2.1.2, listed in order investigated. P7 represents depressurisation of the cell following measurements under pressure.*

Figure 5.7 illustrates the AC susceptibility measurements for three representative frequencies under various pressures. The behaviour of the χ' and χ'' peaks under

pressure is consistent across all of these frequencies as well as those not shown. Several major features are evident as a result of the pressure application:

- Real and imaginary susceptibilities increase dramatically with pressure initially, implying improved spin alignment of the domains, before suddenly dropping at pressures ≥ 0.44 GPa.
- Peaks likewise shift to higher temperature before returning to lower values directly in line with the susceptibility behaviour.
- A distinct asymmetrical broadening becomes apparent at 0.44 GPa in χ' coinciding with the susceptibility drop.
- Asymmetry of χ' resolves into two distinct peaks at the highest pressure of 0.60 GPa.

In addition to these major features we also observe recovery of the ambient pressure susceptibility on depressurisation, indicating any pressure induced changes are reversible. A slight drop in signal magnitude is seen between the P0 and P7 ambient pressure measures yet the overall shape is maintained, indicating the same susceptibility behaviour is present. Interestingly pressure step P1 should have depressurised to ambient pressure at 2 K as determined by our manganin gauge (see Table 5.1); however, the susceptibility has increased somewhat which is indicative of the following behaviour at higher pressures. It is possible that some small residual pressure not detected by our manganin gauge is still being exerted on the sample which would be consistent with the susceptibility increase. The gauge is not located directly at the sample thus any residual pressure acting on it, for instance from a slight expansion of the coil bracket surrounding it, could potentially not be detected. The low pressure increase of the susceptibility peak positions indicates onset of SCM behaviour at higher temperatures which is more desirable for effective applications.

In order to corroborate these observed pressure induced features, the Murrie group performed independent pressure measurements on a separate sample. AC susceptibility measurements with a 3 Oe field amplitude were carried out on a SQUID magnetometer utilising a piston cylinder pressure cell up to pressures of 1.3 GPa. Due to the background signal of the pressure cell their measurements were restricted to frequencies of 20 Hz and lower. All the major features noted above were also observed in their measurements, thus eliminating the possibility

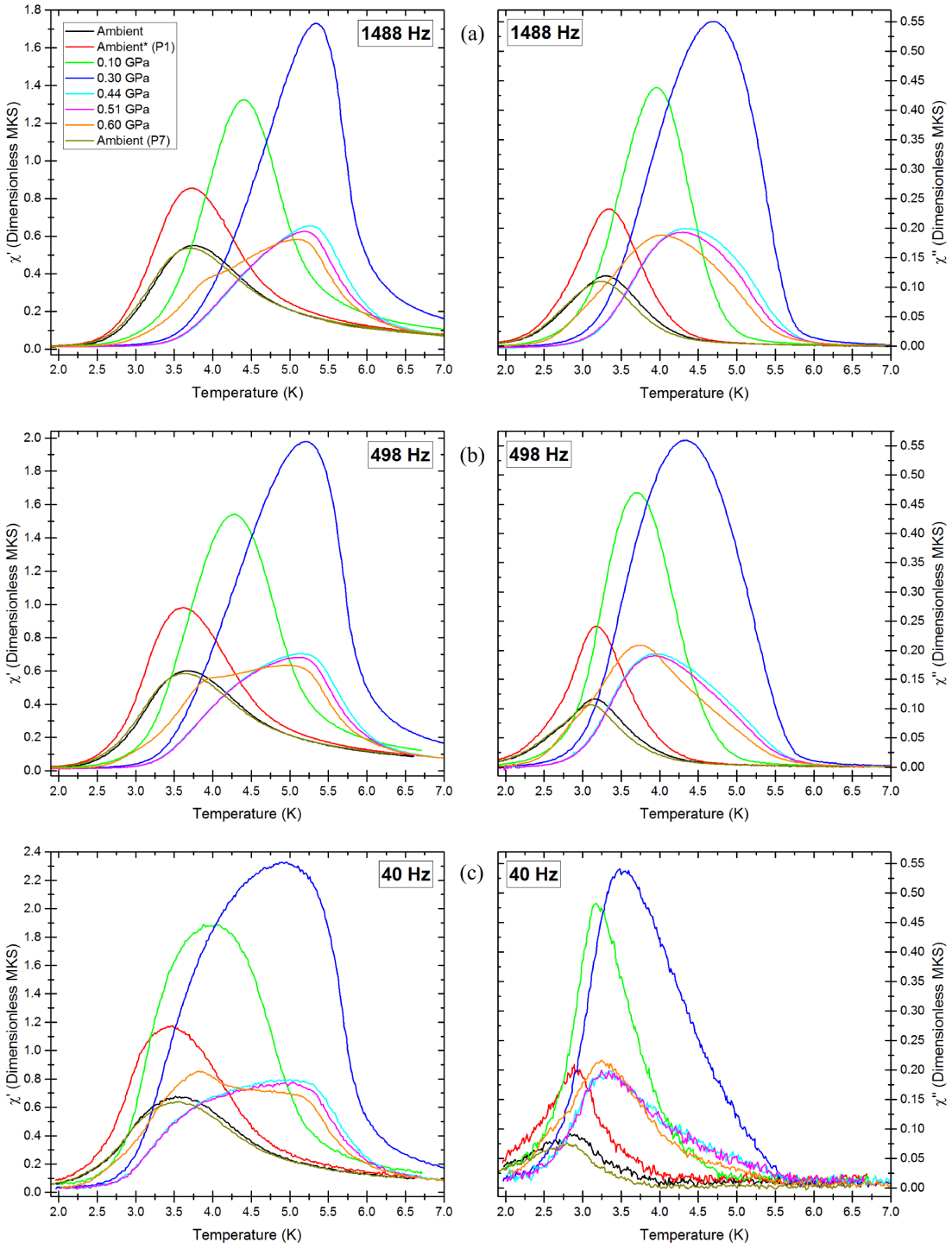

Figure 5.7 *Temperature dependent real and imaginary susceptibility measurements of $[Co(NCS)_2(pyridine)_2]_n$ sample under various pressures (low temperature values listed, top left) at selected frequencies (a) 1488 Hz, (b) 498 Hz and (c) 40 Hz. *P1 pressure step (red lines) has depressurised to ambient at 2 K although potentially some small residual pressure may remain.*

of these being attributed to our specific setup or coil background changes. Furthermore, the Murrie group has conducted crystallographic measurements under pressure and discovered development of a new high pressure structural phase. The crystallography data indicates that in this new high pressure phase the pyridine ring ligands (see Figure 5.1) fold in alongside the chain and allow them to slot together at the highest pressures. Indeed in their highest pressure AC susceptibility measurement (1.3 GPa) they observed the broad asymmetrical χ' peak finally resolve into a single sharp peak which is suggestive of only the high pressure phase being present[109].

Thus the two peaks observable in our χ' measurements are likely attributable to a mix of both the original SCM and the new emergent high pressure phase. Indeed further evidence for this is apparent on review of preliminary measurements carried out on the sample. Initially pressure measurements were performed in a cell with a higher 3 GPa limit; however, electrical shorts developed in the pressure cell plug yielding noisy data (especially at low frequencies) and prevented accurate calibration. Connection to the susceptometer within the cell was also lost before high pressures were reached. Due to these issues the susceptometer was transferred to the 1 GPa pressure cell in order to perform the accurate AC susceptibility measurements presented in this chapter. However before connection loss in the 3 GPa cell, a high pressure point of ~0.74 GPa (at 2 K) was measured. Comparison of this high pressure point to the maximum pressure of ~0.60 GPa achieved in the 1 GPa cell is shown in Figure 5.8. It is clear that as the pressure is

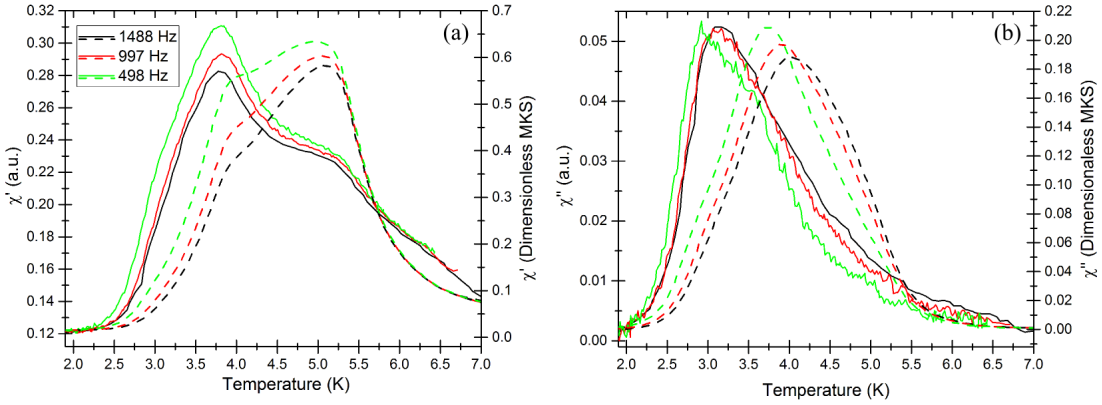

Figure 5.8 *Temperature dependent (a) real and (b) imaginary susceptibility measurements at several frequencies (listed) from susceptometer in separate pressure cells. Solid lines (left axis) illustrate uncalibrated measurements at ~0.74 GPa in the 3 GPa cell whilst dashed lines (right axis) display calibrated measurements at ~0.60 GPa in the 1 GPa cell. Relative heights of χ' peaks indicate shift of phase composition with pressure.*

increased, the high temperature χ' peak is reducing in magnitude whilst the low temperature peak is growing more intense. Such behaviour is indicative of the two phase mix (SCM and high pressure phase) adjusting its relative composition with pressure tending toward existence of only the high pressure phase, as observed by the Murrie Group at 1.3 GPa.

The frequency dependence of the susceptibility was investigated at each pressure and three representative pressures are shown in Figure 5.9 (additional pressures are shown in Appendix A). At low pressures, such as 0.10 GPa shown in (a), the susceptibility exhibits characteristic SCM behaviour with frequency dependent peak positions and broadening of the χ' peak at lower frequencies. As noted above, such behaviour persists until a sudden drop in susceptibility is observed at pressures $\geq$ 0.44 GPa. In this mid-pressure regime, see (b) 0.51 GPa, a distinct broadening and asymmetry is noticeable in χ' which has been attributed to potential coexistence of the two aforementioned phases (SCM and high pressure phase). The χ' peaks continue to broaden and shift to lower temperatures with decreased frequency, implying the most significant response is still consistent with SCM behaviour. χ'' has also broadened with pressure increase which is likely a consequence of the phase coexistence. Finally at the highest pressure measured, (c) 0.60 GPa, the broad asymmetric χ' has resolved into two overlapping peaks directly attributable to the two phases. The lower temperature peak appears to have a stronger frequency dependence than the high temperature peak, implying significant difference in their behaviour. Similar behaviour is also observable in the uncalibrated 0.74 GPa step displayed in Figure 5.8. Broad χ'' peaks are also observed which potentially may be comprised of two peaks attributable to each phase, yet if this is the case separation of these is not straightforward.

5.5 Analysis

Using these measurements we are able to further analyse the precise development of the samples behaviour with pressure. In terms of the static behaviour we make use of the 10 Hz χ' measurements to determine if the sample continues to be described by the anisotropic Heisenberg chain model. Ideally this should be concluded from both DC and very low frequency AC ($\sim$1 Hz) measurements (as in Section 5.2) in order to represent the static nature; however, in our measurements 10 Hz proved to be the lowest frequency with reasonable signal to noise. DC measurements can only be performed within a SQUID magnetometer and are

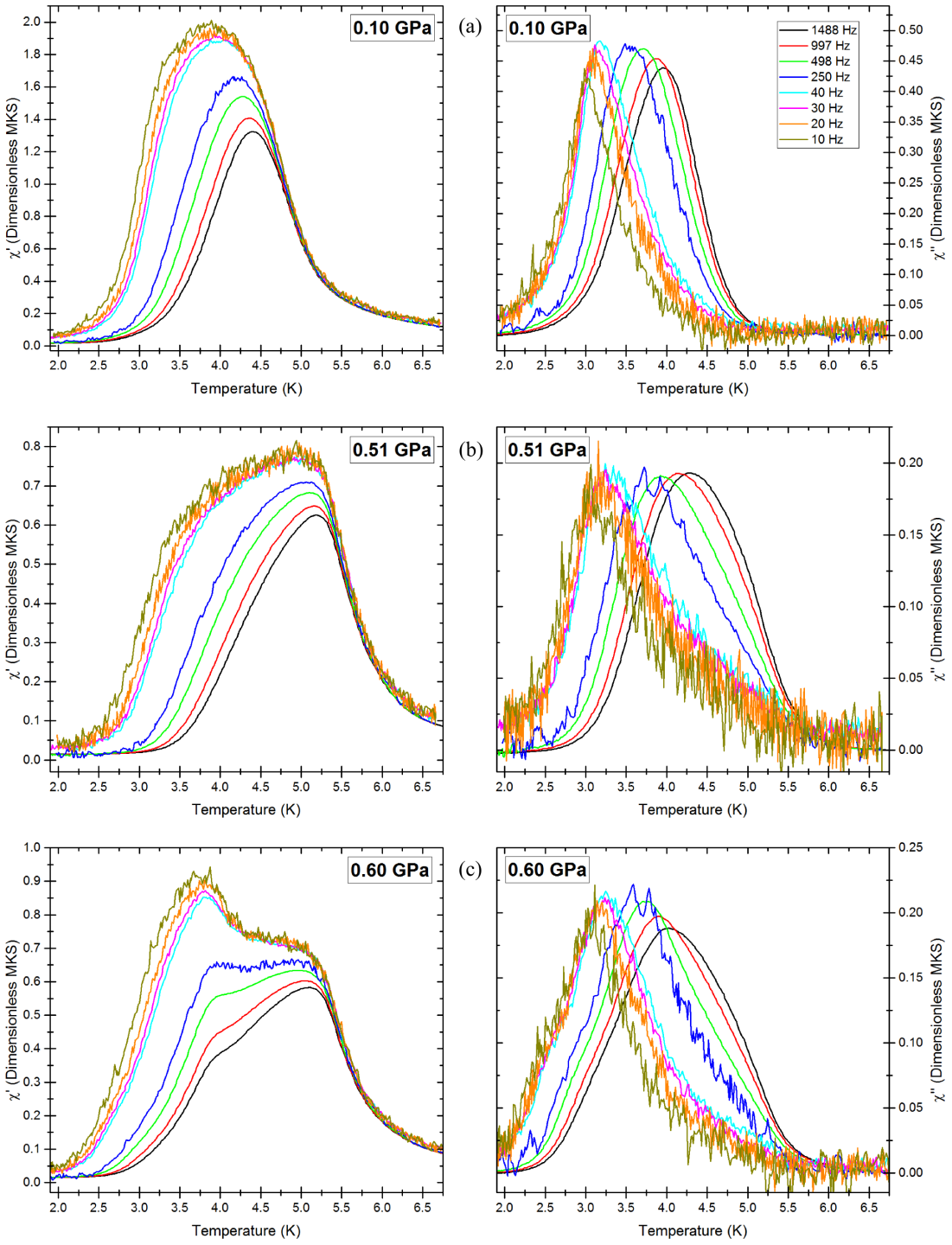

Figure 5.9 *Temperature dependent real and imaginary susceptibility measurements of $[Co(NCS)_2(pyridine)_2]_n$ sample under various frequencies (listed, top right) at selected pressures (base temperature values) (a) 0.10 GPa, (b) 0.51 GPa and (c) 0.60 GPa.*

not possible with our cell due to its size and significant background contribution. Thus Figure 5.10 (a) displays $\ln(\chi' T)$ versus $1/T$ for the 10 Hz AC measurements across the pressures investigated overlaid with the SQUID data from Figure 5.5 (a). Even at the higher frequency of 10 Hz the ambient pressure measurements (P0 and P7) agree with SQUID measurements, indicating linearity toward a maximum and then decrease with falling temperature. Additionally P0 and P7 match well, confirming full recovery of the static behaviour after pressure induced changes. The anomalous pressure step P1 should also exhibit ambient pressure at these temperatures yet the increased χ' signal is evident once again, although the general shape of the curve is still reminiscent of the same behaviour.

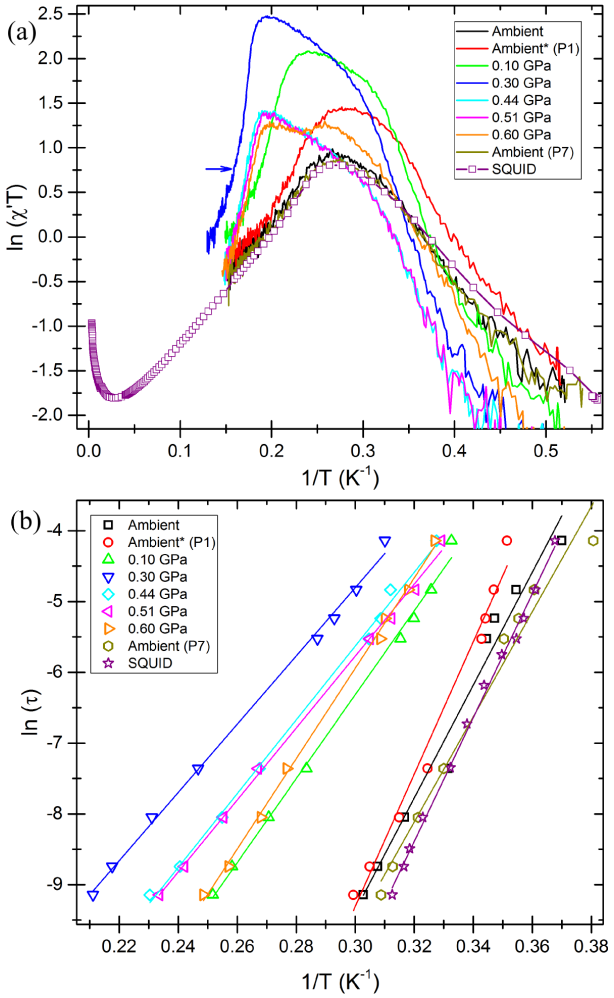

Figure 5.10 *(a) $\chi' T$ for 10 Hz AC susceptibility measurements at various pressures (listed) overlaid with ambient pressure SQUID measurements from Figure 5.5 (a). Arrow indicates kink discussed in main text. (b) Arrhenius plots of relaxation times determined from χ'' peak temperatures at various pressures (values in Appendix A) fitted to the Arrhenius law of Equation 5.4 (lines) including ambient pressure SQUID measurements from Figure 5.5 (b). *P1 pressure step (red curves) has depressurised to ambient at 2 K although potentially some small residual pressure may remain.*

Increase in pressure results in a broadening of the maximum which is attributable to development of the high pressure phase coexisting with the SCM phase. The high temperature linear regime persists across the pressure range indicating the sample may still be described by the 1D anisotropic Heisenberg model. The slope in this regime also grows steeper, implying the domain wall creation energy Δ_{ξ_c} is increasing and thus so is the intra-chain magnetic coupling (J) according to Equation 5.3. SCM behaviour relies on strong magnetic coupling of spins[3, 102] which pressure appears to be improving. However without DC measurements to corroborate the linear regime it is inadvisable to formally fit this, especially in light of the altered curve profiles. Indeed close investigation of the linear regime in Figure 5.10 (a) reveals a possible kink (indicated by arrow for one pressure), perhaps indicating two competing regimes which could be a result of the phase coexistence. Thus any conclusions drawn on the development of the static behaviour with pressure must be treated with caution.

While the asymmetry is quite marked in the χ' signal the χ'' peaks generally only broaden with pressure. Thus determination of the dynamic behaviour should still be possible through the temperature dependent relaxation times associated with χ'' maxima. Figure 5.10 (b) displays such relaxation times determined for each pressure, with linear fits to the Arrhenius law of Equation 5.4. Extraction of the various parameters associated with the Arrhenius law are listed in Table 5.2 along with the Mydosh parameter calculated from Equation 5.7. The ambient pressure values (P0 and P7) still agree well with each other, indicating the dynamic behaviour is recovered after pressure application.

Pressure Step	Pressure at 2 K (GPa)	τ_0 (s)	E_a/k_B (K)	φ_M
P0	0.1 x 10^{-3}	3.53 x 10^{-15}	79.7	0.096
P1	0.1 x 10^{-3}	6.04 x 10^{-17}	93.5	0.071
P2	0.10	3.37 x 10^{-11}	59.3	0.138
P3	0.30	4.28 x 10^{-9}	48.2	0.203
P4	0.44	5.81 x 10^{-10}	52.1	0.176
P5	0.51	7.43 x 10^{-10}	50.8	0.176
P6	0.60	1.26 x 10^{-11}	63.9	0.135
P7	0.1 x 10^{-3}	9.79 x 10^{-15}	75.4	0.109

Table 5.2 *Table of energy activation barriers and characteristic time determined from Arrhenius fits as well as the average Mydosh parameter calculated from Equation 5.7 at each applied pressure. P7 represents depressurisation of the cell following measurements under pressure.*

Figure 5.11 illustrates the development of these parameters with pressure. The SQUID values from Section 5.2 are also represented and tend to agree with those determined from our ambient pressure susceptibility measurements. The Mydosh parameter increases from ambient values indicating the sample is clearly within the expected superparamagnetic regime, $0.1 < \varphi_M < 0.3$, under pressure. The characteristic time τ_0 markedly grows by several orders of magnitude and plateaus at values consistent with other SCM systems[106, 108]. τ_0 is representative of the characteristic spin flip time for a given material, and the observed increase indicates a shift of the system from metallic to more insulating behaviour[3]. Such a change may be indicative of altered Co cation behaviour, potentially influenced

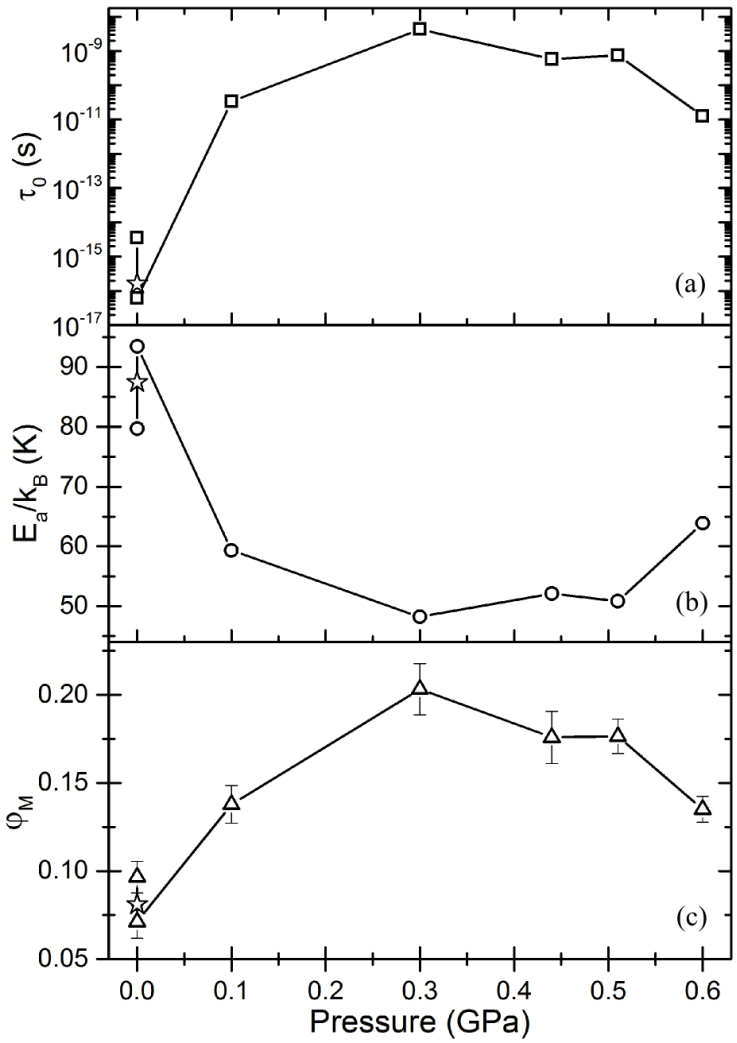

Figure 5.11 *Pressure dependence of (a) characteristic time τ_0, (b) spin reversal activation barrier E_a/k_B and (c) Mydosh parameter φ_M as determined from our AC susceptibility measurements. Ambient pressure values determined from SQUID data are also included (star). Values plotted in order pressures investigated as laid out in Table 5.2, depressurised step P7 excluded for clarity.*

by the pyridine ligands shifting positions relative to the chain under pressure. However further measurements would be required in order to corroborate this. Regardless, increased τ_0 values indicate pressure could be conducive to longer relaxation times in this system. Conversely the spin reversal activation energy E_a drops and plateaus with increased pressure, which is not suggestive of improved SCM behaviour. Indeed the relaxation time of a system is most heavily influenced by the value of E_a due to its exponential dependence within the Arrhenius law, thus it dominates over τ_0. A lower E_a implies decrease of the chain's magnetic anisotropy, especially if the suggested increase of Δ_{ξ_c} from our limited static measurements is taken into account. The anomalous improvement of E_a for the first pressure step (P1) provides the most beneficial SCM behaviour, even with a reduced τ_0. As has been mentioned previously, this may be a result of small residual pressure acting on the sample, implying very low pressures may exhibit different trends to those observed across the following range.

At the highest pressure investigated E_a begins to increase once more, and coupled with the still relatively large τ_0 provides a promising indication for further enhancement of SCM behaviour at greater pressures. Indeed at this point the high pressure phase becomes directly observable as a secondary peak in our susceptibility data, and its behaviour may be dominating over the original SCM phase. The crystallographic measurements performed by the Murrie group indicate the chains lock together in this new high pressure phase; thus there may be more significant contributions from inter-chain coupling influencing the behaviour along the chain[109]. The marked difference in frequency dependence of the two χ' peaks implies the behaviour is indeed quite different in the two phases. According to our susceptibility data the high pressure phase is likely already present in our mid-pressure regime from observed asymmetry of χ'. Whilst this asymmetry is not discernible in the χ'' peaks the observed broadening may be due to two very closely overlapping peaks attributable to each phase. Thus analysis utilising the single broad χ'' maximum alone may not produce an entirely accurate representation of the dynamics.

In the low frequency AC measurements performed by the Murrie group they observed a single sharp χ' peak with no asymmetry at 1.3 GPa indicating only the high pressure phase remains[109]. Thus, measurement of AC susceptibility on our setup at higher pressures, where only this new phase is present, will allow determination of its peak profiles and frequency behaviour. Utilising these measurements, it may be possible to accurately fit two peaks to the broad

χ'' and identify development of the individual phases behaviour with pressure. Investigation of the high pressure phase will also reveal if it too exhibits SCM behaviour, and whether it possesses more favourable properties than the low pressure phase.

5.6 Conclusions

Calibrated frequency dependent AC susceptibility measurements have been conducted on the SCM $[Co(NCS)_2(pyridine)_2]_n$ under pressure utilising our constructed susceptometer in a piston cylinder cell. Increase of the susceptibility and peak positions is observed at low pressures, implying improved spin alignment, followed by decline above a threshold pressure of 0.44 GPa. At this pressure development of an asymmetry in χ' is observed, which resolves into two distinct peaks at 0.60 GPa, attributed to coexistence with a new high pressure phase observed independently in crystallographic measurements by the Murrie group. Independent AC susceptibility measurements confirm the reproducibility of this behaviour. All pressure induced changes are reversible. Fits of thermally activated Arrhenius laws to frequency dependent data indicates the characteristic time τ_0 grows by several orders of magnitude. However, the spin reversal activation barrier E_a reduces, implying pressure is not conducive to longer relaxation times nor improved SCM behaviour. However the coexistence of these two phases with potentially different behaviour may be obscuring these results. Completion of similar AC measurements at high pressures where only the high pressure phase is present, as determined by the Murrie group, is recommended in order to characterise the new phase and separate the individual phase behaviour in this coexistence regime.

Chapter 6

AC Susceptibility of U_6Fe

U_6Fe is a heavy fermion superconductor exhibiting unusually high H_{c2} values exceeding both the orbital and Pauli limits. A charge density wave (CDW) has recently been observed in it[110] and its Maki parameter is high, indicating it should be in the Pauli limit, thus making it a promising candidate for exhibiting the theorised Fulde-Ferrel-Larkin-Ovchinnikov (FFLO) state. Suppression of the CDW in similar U-based compounds is achieved with pressure[111] which could allow for formation of the FFLO state. Thus AC susceptibility measurements are carried out on a U_6Fe sample, along the unexplored c-axis, using our susceptometer in a 1 GPa piston cylinder cell to map H_{c2}(T) and search for evidence of such a state under pressure.

6.1 U_6Fe Review

U_6Fe is a heavy fermion superconductor ($m^*/m_e \approx 23$[112, 113]) with the highest T_c ~4 K of all the U-based compounds[110]. It has a body-centred tetragonal structure with the I4/mcm space group, as seen in Figure 6.1, and lattice parameters $a = b = 10.302$ Å and $c = 5.2385$ Å under ambient conditions[110, 114].

Anisotropy is observed for the upper critical field H_{c2} with typical values of 13.1 T, 10.4 T[115] and 10.19 T[110] in the [001], [110] and [100] directions respectively. Interestingly all of these exceed not only the Pauli limit prediction but also the BCS orbital limit for U_6Fe. The Maki parameter α_M is directly proportional

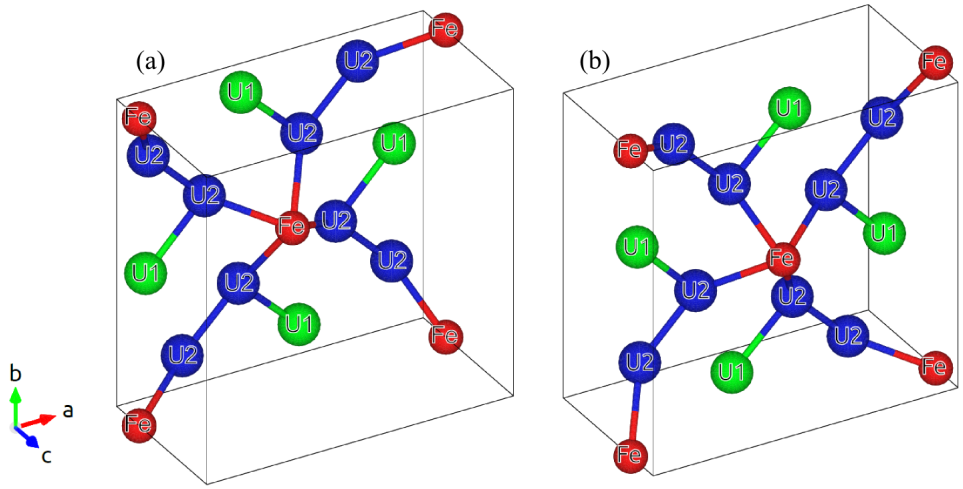

Figure 6.1 *U_6Fe structure viewed between (a) $z = 0$ & $z = \frac{1}{4}$ and (b) $z = \frac{1}{2}$ & $z = \frac{3}{4}$. U atoms occupy two sites with U_1 at $(x,x+\frac{1}{2},0)$ and U_2 at $(x,y,0)$[110].*

to electron mass, and thus for heavy fermion materials Pauli limiting is more likely[116]. Applying Equations 1.3 & 1.4 to early measurements of single crystal U_6Fe[115] predict an orbital H_{c2} = 9.88 T in the clean limit and Pauli H_{c2}^P = 7.24 T respectively, both well below the actual measured values; suggesting BCS theory is inadequate. Whitley, however, has had some success in fitting critical field curves measured along the a-axis utilising a two-band model[110]. Under application of pressure H_{c2} and T_c have also been found to increase initially reaching a maximum before falling. Early measurements on U_6Fe observed a maximum T_c ~4.2 K at ~0.6 GPa[117] whilst more recent measurements have found a T_c ~4.4 K at ~1.2 GPa indicating this increase is likely affected by sample quality[110].

AC susceptibility measurements along the a-axis of U_6Fe have previously been performed under pressure in order to investigate its effect on H_{c2}(T). In order to minimise any background signal a plastic diamond anvil cell was used, yet due to the small sample space available a background subtraction was necessary. Even so the measurement sensitivity proved poor in the higher field regime preventing detailed results[110]. Evidence for the peak effect along with collective pinning, as discussed in Section 1.4.3, has been observed in resistivity measurements on U_6Fe[110], implying it may also be observable in AC susceptibility if the sensitivity is improved compared to previous measurements.

Whitley recently confirmed the existence of a suspected charge density wave (CDW) in U_6Fe at T_{CDW} ≈10 K via X-ray scattering measurements[110]. Figure 6.2 (a) illustrates the satellite peaks appearing below 10 K at a reciprocal lattice

ordering vector $(\delta h, \delta k, \delta l) = (\pm 0.11, \pm 0.11, 0)$ around the (10,0,2) Bragg peak. Such satellite peaks indicate a modulation of the underlying crystal lattice[118] and are the clearest evidence of the CDW observed in the related α-U system[111]. In Figure 6.2 (b) the intensity of the satellite peaks is seen plateauing below the superconducting T_c, indicating the CDW does not develop further likely due to superconductivity gapping the Fermi surface. The intensity however does not noticeably reduce either indicative of coexistence of the CDW with superconductivity[110].

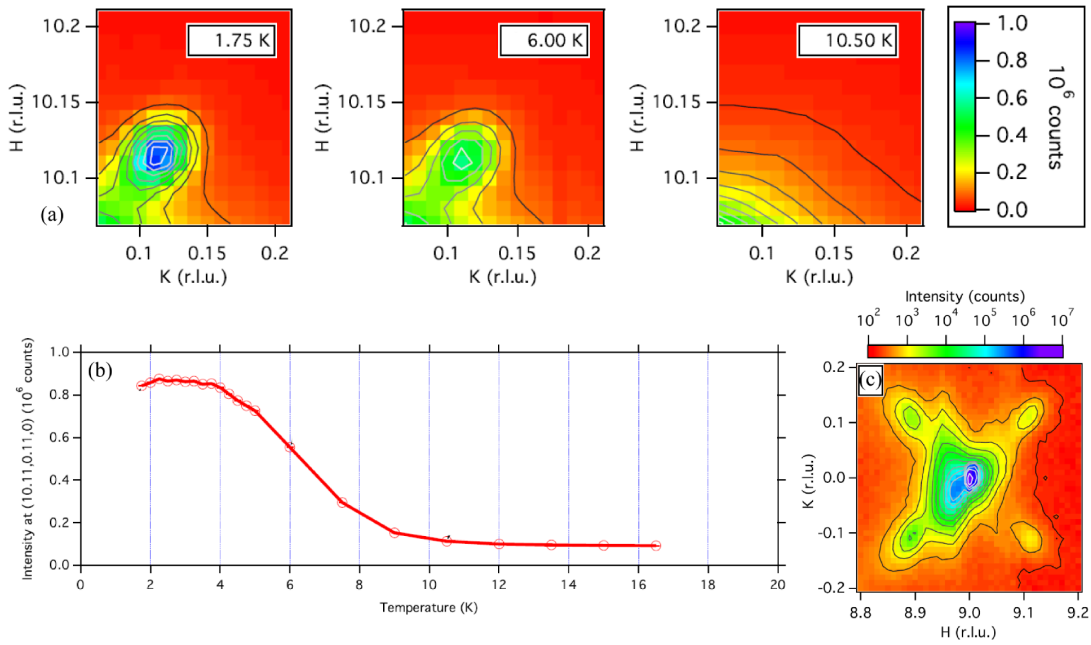

Figure 6.2 *(a) X-ray scattering intensity map in (h,k) space illustrating appearance of satellite at (+0.11,+0.11,0) around the (10,0,2) Bragg peak below 10 K and (b) intensity of satellite peak across temperatures plateauing below T_c ~4 K. (c) Satellite peaks appearing around forbidden (9,0,1) Bragg peak[110].*

Additionally, a feature at ~110 K has been previously observed in a number of measurements suggesting a possible transition, yet its exact nature has not been clearly identified. Often evidence of this feature is subtle such as a slight kink in resistivity data[119] or a disparity in Mössbauer spectra, seen in Figure 6.3 (a). Whitley noted a step in specific heat measurements as well as an anomaly of Bragg peak intensity, seen in Figure 6.3 (b), suggestive of U atom movement at this temperature[110]. It had been suggested previously that this transition may be due to formation of a CDW[119] yet the satellites attributed to this only develop at 10 K[110]. Thus the nature of the feature at 110 K still remains uncertain but could be caused by a potential breaking of crystal symmetry. Indeed in X-ray scattering experiments Whitley observed $(h, 0, l)$ Bragg peaks (h & l odd)

forbidden by the c-glide symmetry of the I4/mcm space group which also exhibit the CDW satellite peaks, shown in Figure 6.2 (c). Below T_{CDW} the forbidden peaks were determined to not be the result of multiple scattering, yet this may be the case at higher temperatures[110].

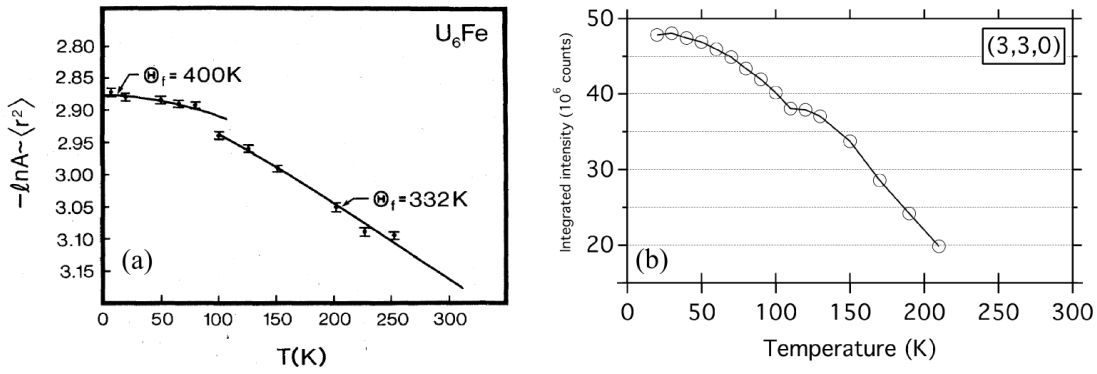

Figure 6.3 *(a) Mössbauer absorption data[114] and (b) intensity of the diffracted (3,3,0) Bragg peak both illustrating a discontinuity at 110 K[110].*

6.1.1 FFLO state

CDW formation is often favoured by systems with nested Fermi surfaces, those with large parallel flat regions, a condition which may also support development of the theorised Fulde-Ferrel-Larkin-Ovchinnikov (FFLO) state[110]. The FFLO state, proposed independently by Fulde & Ferrel[120] and Larkin & Ovchinnikov[121], is a novel form of superconductivity where the order parameter (Δ) is modulated in real space in the presence of an applied field according to

$$\Delta(\mathbf{r}) = 2\Delta_1 cos(\mathbf{q} \cdot \mathbf{r}) \tag{6.1}$$

Such modulation was proposed in order to allow for pairing of electrons even when the Fermi surface splits in momentum space due to field in the Zeeman effect. Figure 6.4 (a) illustrates how ordinarily electrons of opposite spin and momenta pair in a superconductor, yet this cannot be the case if the Fermi surface splits yielding electrons with differing momenta. However, with an additional momentum $\mathbf{q}$ from this modulated state some electrons of opposite spin are able to pair as seen in Figure 6.4 (b). The degree to which such pairing occurs is dependent on the Fermi surface shape, with nested surfaces being the most favourable towards the FFLO formation as shown in Figure 6.4 (c). Pauli paramagnetism is thus important to the FFLO state creation, requiring a material

to be in the Pauli limit in order to manifest it[122]. Indeed pair breaking in the orbital limit has been shown to impede development of the FFLO state[123]. Thus the necessary Maki parameter, which indicates the dominant limit, in order for the FFLO state to form must be α_M >1.8[122]. Calculation of α_M for U_6Fe, based on Equations 1.3 & 1.4, exceeds this limit, and indicates it is a promising candidate to exhibit FFLO[110].

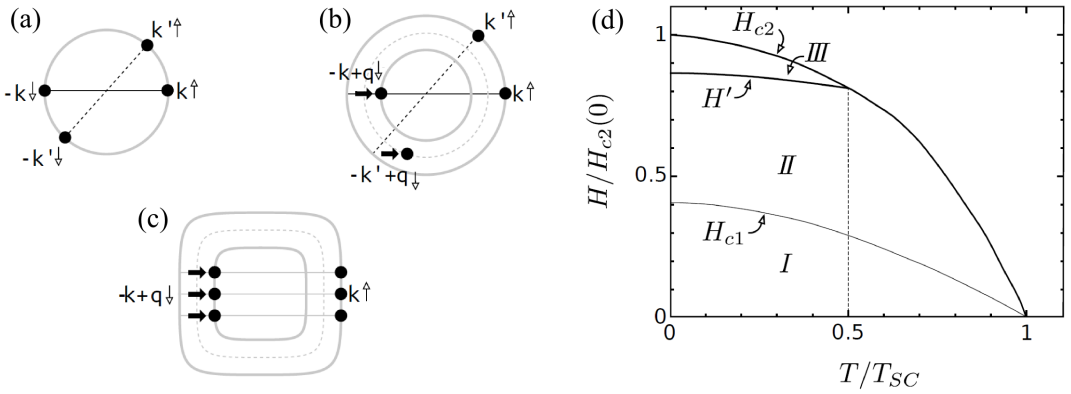

Figure 6.4 *Figures from [110, 122] illustrating (a) ordinary pairing of electrons with opposite spin and momentum and (b) pairing in the FFLO state between electrons of momenta k and $-k+q$. The additional momentum q does not allow pairing of all electrons such as those of momentum $k', -k'$. (c) A nested Fermi surface with larger parallel flat regions allowing a greater degree of pairing. (d) Phase diagram for the Meissner (I), mixed (II) and FFLO (III) superconducting states. All lines represent second order transitions except for the H' line which is first order.*

A phase diagram of the FFLO state is shown in Figure 6.4 (d) illustrating its predicted emergence above a critical field H' from the mixed state through a first order transition[122]. Evidence of such a transition has been detected in both specific heat and torque magnetometry measurements in the organic superconductor κ-(BEDT-TTF)$_2$Cu(NCS)$_2$ along with a simultaneous upturn in H_{c2} in both instances[124]; which is a further predicted signal of the FFLO state[110, 122]. Figure 6.5 depicts the phase diagrams deduced from these measurements which closely resemble that expected for FFLO and has provided the most robust evidence for existence of this phase so far[124]. Potential evidence for the FFLO state has also been detected in $CeCoIn_5$ where an additional phase within the superconducting region emerges, yet the exact nature of this has not been conclusively determined[110, 125]. While these two materials provide promising evidence for the FFLO state consensus on this experimental proof of its existence is yet to be reached.

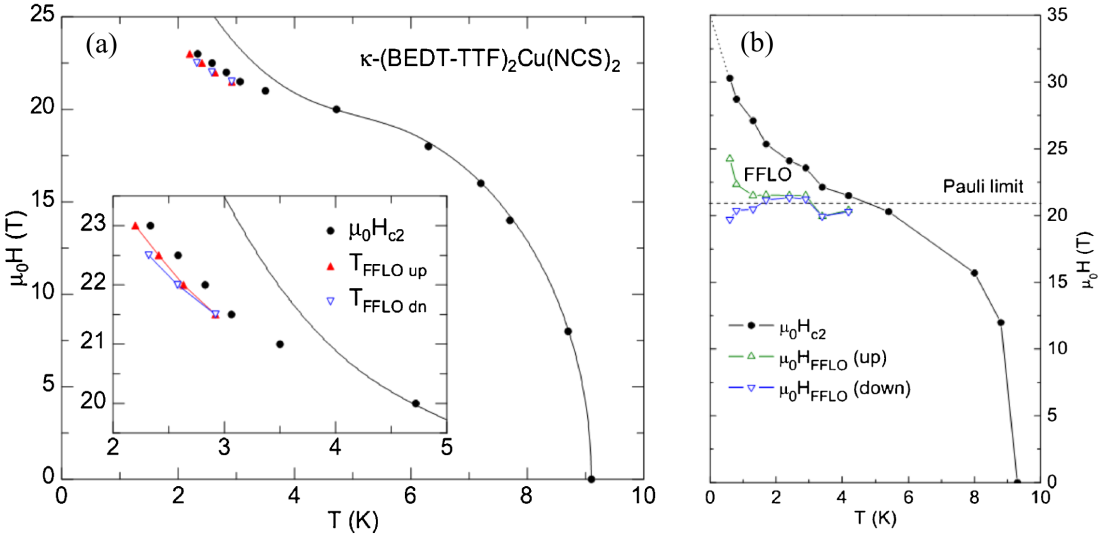

Figure 6.5 *Phase diagrams for κ-(BEDT-TTF)$_2$Cu(NCS)$_2$ deduced from (a) specific heat and (b) magnetic torque measurements both indicating a first order transition attributed to the FFLO state as well as a concurrent upturn of H_{c2}[124].*

Pressure induced increases of T_c in U-based systems have been attributed to suppression of the CDW[111], which may also be the case in U_6Fe. Suppression of the CDW could give rise to the FFLO state as both take advantage of the same nested Fermi surface arrangement. Thus AC susceptibility and resistivity measurements under pressure along the a-axis of U_6Fe were conducted by Whitley in search of such an FFLO state, yet no conclusive evidence was observed[110]. However due to the large anisotropy of H_{c2} in U_6Fe, mapping its development with pressure in other crystallographic directions could well reveal development of this state, especially in light of the newly discovered CDW.

6.2 Characterisation

6.2.1 Synthesis and Sample Quality

In the following chapter all measurements have been performed on a single crystal U_6Fe sample synthesised via the Czochralski crystal pulling technique. Whitley refined the synthesis of these single crystal samples maximising sample quality to the highest levels to date by solid state electrotransport treatment, as evidenced by their residual resistivity ratios (RRR)[110]. The sample in question was cut into a bar arrangement with volume 5.96 x 10^{-4} cm^3 and faces perpendicular

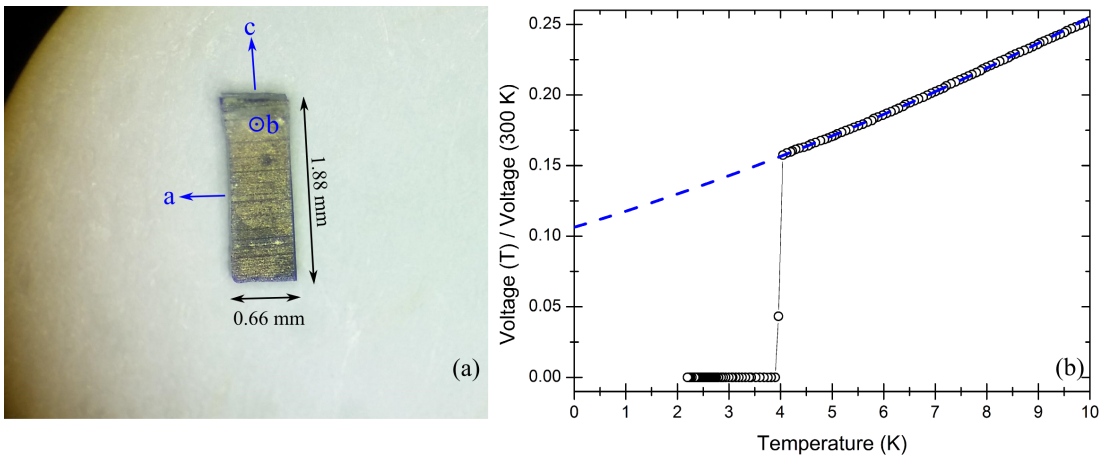

Figure 6.6 *(a) U_6Fe sample with relevant dimensions (depth of 0.48 mm not shown) and crystallographic axis indicated and (b) 300 K scaled voltage curve from four-point resistivity measurement indicating the superconducting transition and normal state extrapolation (blue dashed line) to 0 K.*

to the crystal lattice planes as shown in Figure 6.6 (a). Laue X-ray diffraction confirmed these crystallographic directions as well as indicating the sample was indeed highly crystalline. A four-point resistivity measurement along the c-axis direction of the sample was performed down to 2 K in order to determine the sample RRR and hence its quality. As can be seen in Figure 6.6 (b) the sample exhibits superconductivity with a T_c ~4.00 ± 0.04 K as expected for U_6Fe; a fit to T^2 dependence of the normal state confirms a RRR ~9.40 consistent with the highest sample quality achieved in this system thus far[110].

6.2.2 AC Susceptibility Measurement

Temperature dependent AC susceptibility measurements were performed along the c-axis of the U_6Fe sample in a SQUID magnetometer to provide a baseline characterisation of its behaviour and for calibration of our susceptometer. Figure 6.7 (a) illustrates the onset of superconductivity at T_c ~3.99 ± 0.01 K for several frequencies, with near complete shielding, consistent with the resistivity determined T_c. Losses in χ'' appear very suddenly at T_c and peak at the steepest part of the superconducting transition in χ', as indicated by the dashed line, before becoming almost non-existent at lower temperatures. This single peak is associated with intra-grain losses and the absence of any secondary coupling peak (as discussed in Chapter 4) in tandem with the sharp transition of χ' implies our sample is single crystalline with no granularity[4, 49]. Figure 6.7 (a) also indicates

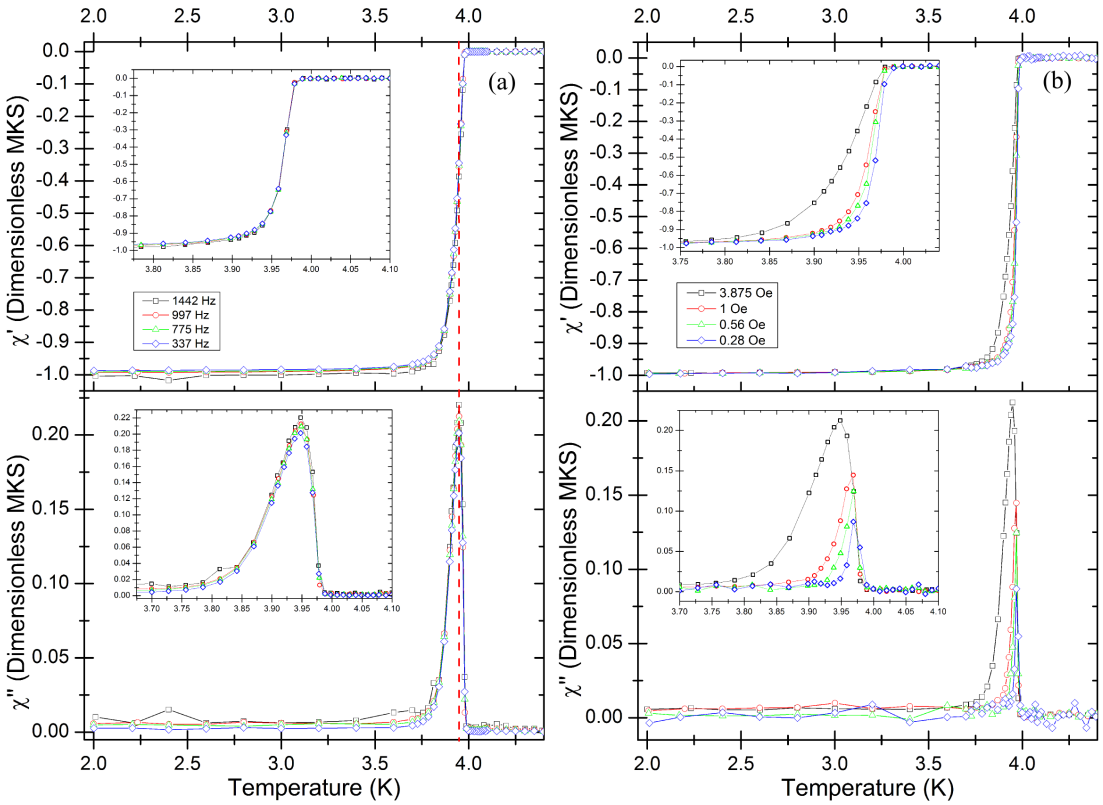

Figure 6.7 *Real and imaginary AC susceptibility versus temperature of U_6Fe along c-axis measured on SQUID magnetometer at (a) 3.875 Oe AC field amplitude and several frequencies (listed in key) and (b) 1442 Hz and several AC fields (listed in key).*

there is no apparent frequency dependence in the U_6Fe transition across the SQUID's accessible range, although there may be some minimal change in the low temperature saturation value.

Figure 6.7 (b) illustrates the susceptibility response of U_6Fe under several AC field amplitudes at 1442 Hz. As can be seen, increasing field amplitude leads to a broadening of the superconducting transition in χ', as well as the loss peak in χ'', due to a larger degree of flux penetration within the sample. The intensity of χ'' also increases with field indicative of a higher degree of losses. Thus use of small AC field amplitudes should ensure sharp well defined transitions in our measurements.

6.2.3 Calibration and Experimental Setup

The U_6Fe sample was inserted into a susceptometer of design 2, ensuring a maximal filling factor and hence signal, mounted on a pressure cell plug with the c-

axis oriented parallel to the coil axis. A 20 μm silver wire was silver painted to one end of the sample and fed out of the coil onto the pressure cell plug to thermalise the sample appropriately. The cell is just sealed allowing for pseudo-ambient pressure measurements as well as a consistent setup for comparison to higher pressure data. Temperature dependent AC susceptibility measurements through the superconducting transition are performed at 1442 Hz on the high temperature setup described below, and corrected for coil backgrounds. Comparison to SQUID measurements under the same conditions allowed experimental determination of the calibration constant α in the same manner described in Chapter 4, providing good fits to data. All proceeding measurements have been corrected for coil backgrounds before calibration.

High Temperature Setup

A helium gas exchange closed cycle refrigerator (CCR) with an accessible temperature range of 1.9 - 300 K and maximum magnetic field of 9 T is employed for the high temperature measurements. A stable driving current to the primary coil of the susceptometer is supplied by a high frequency Keithley 3390 voltage waveform generator in series with a stabilising resistor as discussed in Section 2.2.7. The AC response of the U_6Fe sample is detected from the secondary coils by a Signal Recovery 830 lock-in amplifier triggered by the 3390.

Figure 6.8 illustrates the ambient pressure real and imaginary susceptibilities measured under a $\sim$0.28 Oe AC field at 9777 Hz, compared to SQUID measurements at 1442 Hz. A superconducting T_c $\sim$4.01 $\pm$ 0.01 K is observed in χ' consistent with that measured in the SQUID, although a very small offset of $\sim$0.025 K is evident which is attributed to slight discrepancy in thermometer calibrations between the instruments. The low temperature magnitude of χ' also fails to fully match that observed in the SQUID yet potentially this could be due to uncertainty in the calibration. Whilst calibration at 1442 Hz yields a good fit between signal and SQUID data any small uncertainty in this value would be exacerbated under the much stronger measurement signal at 9777 Hz, resulting in the more noticeable difference that is seen in Figure 6.8 (a). Additionally this discrepancy could be attributed to difference in frequency between the measurements. Whilst no strong frequency dependence of the low temperature value has been established in the SQUID measurements of Figure 6.7 (a) there potentially could be a noticeable effect at the higher frequency of 9777 Hz. Even

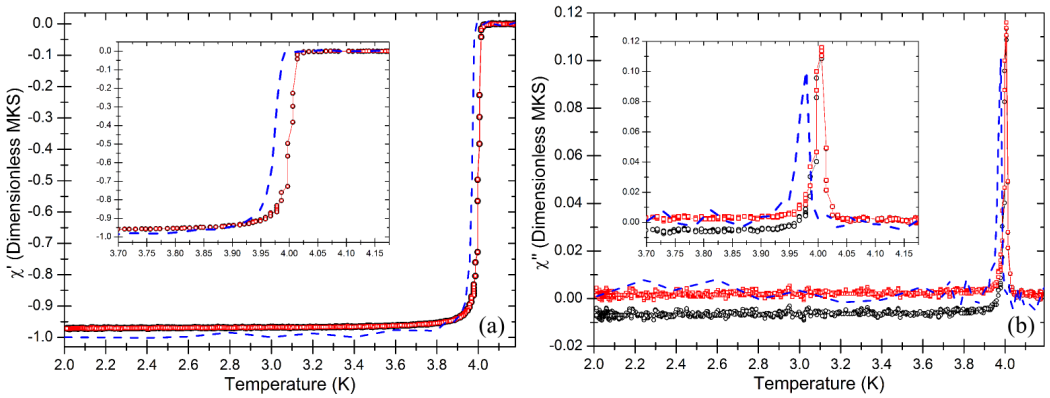

Figure 6.8 *(a) Calibrated real and (b) imaginary susceptibility of U_6Fe in susceptometer at 9777 Hz (black circles) on high temperature setup overlaid with SQUID data taken at 1442 Hz (blue dashed line), both under a ∼0.28 Oe AC field. Red circles indicate data adjusted for 0.5° of dephasing to fit expected χ'' behaviour below T_c as seen in SQUID measurement. Insets feature zoomed in view of superconducting transition.*

so χ' still illustrates approximately near-complete shielding as expected, with the temperature dependent behaviour matching very closely.

However, the disagreement of χ'' below T_c with SQUID measurements seen in Figure 6.8 (b) cannot be explained by this. χ'' represents losses in a material and as such it should always return a positive value[49], yet a negative response can occur if a small degree of dephasing is present in our setup. Dephasing would result in a slight mixing of the much stronger χ' signal with χ'' and explain the appearance of a negative signal below T_c. The origin of this dephasing is unlikely from the susceptometer alone at such a measurement frequency, and is thus attributed to the leads and internal wiring of our CCR. Such dephasing can however be corrected for by rotating the measurement signal using the following rotation matrix

$$\begin{bmatrix} cos\theta_R & -sin\theta_R \\ sin\theta_R & cos\theta_R \end{bmatrix}$$

A rotation angle of $\theta_R = 0.5°$ is required to dephase the data and align the χ'' measurement below T_c to that of the SQUID as seen in Figure 6.8 (b). Such a small rotation illustrates the dephasing is indeed minimal, yet can cause a noticeable effect on the weak χ'' signal. Correction for this dephasing does not noticeably alter the χ' low temperature saturation. Extension of the AC measurement up to 300 K yielded no evidence of magnetic behaviour at either 10 K or 110 K indicative of the features observed in other measurements of U_6Fe. Thus these features likely exhibit no observable magnetic character, nor is any additional behaviour observed over the remaining temperature range.

Low Temperature Setup

Low temperature measurements were conducted on a dilution refrigerator with a base temperature of 20 mK and a 14 T magnetic field. The Keithley 3390 is used to provide the primary coil current as above, with the secondary coil connected to a Signal Recovery 7265 lock-in amplifier triggered by the 3390. A very low AC field of ∼0.028 Oe was employed in order to minimise heating from the coil disrupting the mK temperatures reached by the dilution refrigerator.

Figure 6.9 illustrates the temperature dependent susceptibility at 9777 Hz in the dilution refrigerator overlaid with SQUID data. Immediately obvious from the larger negative χ'' below T_c is a greater degree of dephasing in this setup. As the susceptometer and pressure cell are unchanged the source of the differing dephasing between our setups thus must be attributed to the leads and internal wiring of the dilution refrigerator. Nevertheless, applying a rotation of $\theta_R = 3.9°$ as above accounts for this and realigns χ'' with the expected physical behaviour measured on the SQUID as seen in Figure 6.9 (b). Additionally, comparison of SQUID measurements at ∼0.28 Oe with susceptometer data at ∼0.028 Oe illustrates the χ'' peak is sharper and slightly weaker in magnitude as established for decreasing fields in Figure 6.7 (b) above. Indeed the fact that the χ'' peak is only slightly weaker for an order of magnitude decrease in AC field implies that the sample is in the linear response regime at this frequency, even in the absence of a DC field[126].

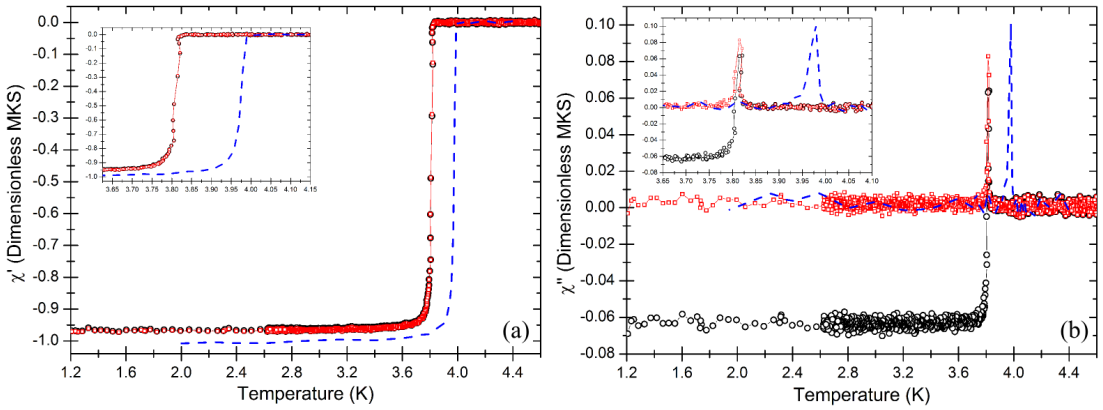

Figure 6.9 *(a) Calibrated real and (b) imaginary susceptibility of U_6Fe in susceptometer at 9777 Hz and ∼0.028 Oe (black circles) on low temperature setup overlaid with SQUID data taken at 1488 Hz and ∼0.28 Oe (blue dashed line). Red circles indicate data adjusted for 3.9° of dephasing to fit expected χ'' behaviour below T_c as seen in SQUID measurement. Insets feature zoomed in view of superconducting transition.*

The measured superconducting transition T_c ~3.81 ± 0.01 K is much lower than expected with a fairly significant disparity of ~0.2 K from the T_c observed in the SQUID and high temperature setup. The high temperature setup above indicates our susceptometer is capable of measuring the transition as accurately as the SQUID, thus this disparity has been attributed to the dilution refrigerator thermometer calibration. The dilution refrigerator thermometer is a Ruthenium Oxide thick-film resistive sensor (model RX-102B-CB) epoxied onto a Oxygen-Free High Conductivity (OFHC) copper mount provided by Lake Shore Cryotronics and calibrated for use down to 10 mK[127]. Dilution refrigerators rely solely on thermal conduction along the cold finger probe, thus thermalisation of a thermometer to the sample is essential. Figure 6.10 illustrates the experimental setup on the dilution refrigerator where the pressure cell is tightly screwed into an OFHC copper connector mounted onto the cold finger ensuring maximal thermal connection of the cell. An additional OFHC copper collar is tightly cinched around the cell body at the approximate sample position, while a copper foil provides a direct thermal bridge to the thermometer mount screwed into the copper connector. Temperature sweeps up and down reproduce the same T_c, indicating no thermal lag and hence good thermalisation of sample to the thermometer. Thus due to the disparity in T_c between setups the calibration of the thermometer has been deemed suspect at these higher temperatures.

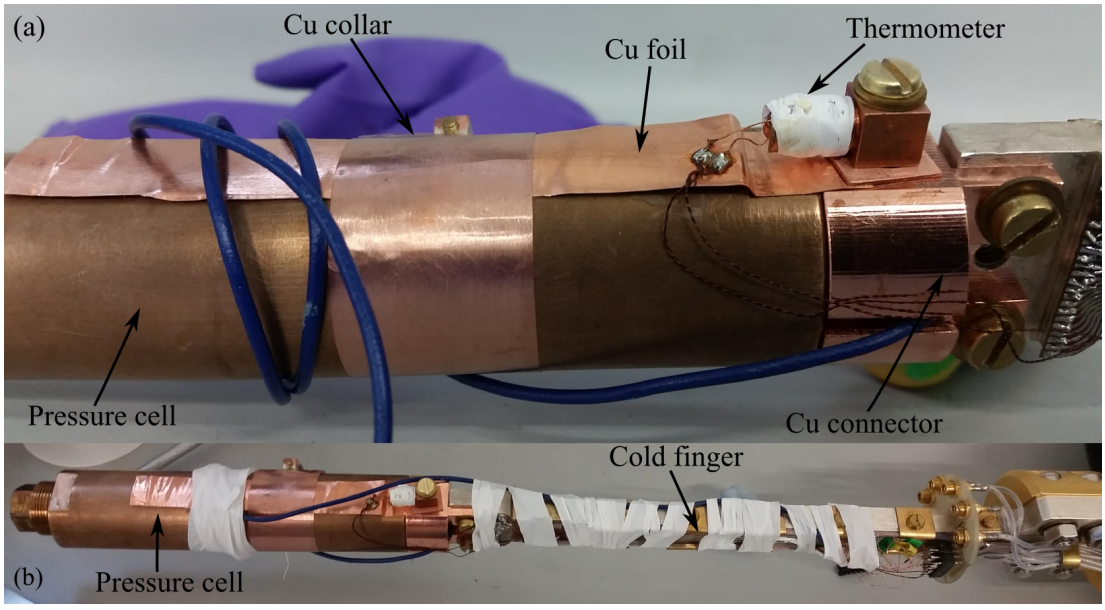

Figure 6.10 *Experimental setup in dilution refrigerator indicating (a) OFHC copper (Cu) collar cinched around cell body with foil bridge clamped by thermometer to connector providing thermalisation along cell body. (b) Pressure cell attached to cold finger probe of dilution refrigerator via copper connector.*

Indeed drift in thermometer calibration through extensive use is common and Lake Shore Cryotronics recommend annual recalibration[128], yet due to lack of an appropriate standard this has not been possible. However, at sub Kelvin temperatures the thermometer accurately reflects the temperature of the dilution refrigerator's internal mixing chamber, and thus the calibration is still deemed appropriate in this low temperature regime.

6.3 Susceptibility Measurements at Ambient Pressure

Field dependent measurements were performed on U_6Fe to map H_{c2} along the c-axis direction down to mK temperatures under ambient pressure. In order to provide consistent measurements between high and low temperature setups the small AC field of ~0.028 Oe has been used for all measurements. Thus a frequency of 9777 Hz is employed to provide a measurable voltage with good signal to noise, as well as having a known dephasing angle from the above temperature dependent data. Higher frequency measurements indicated dephasing becomes a more significant issue, yet for the purposes of H_{c2} mapping it was unnecessary to use these. Figure 6.11 provides an indication of the typical measurable voltages from our susceptometer in comparison to the field dependent coil backgrounds, both accounted for dephasing. Correction for these backgrounds are made for all following measurements before calibration.

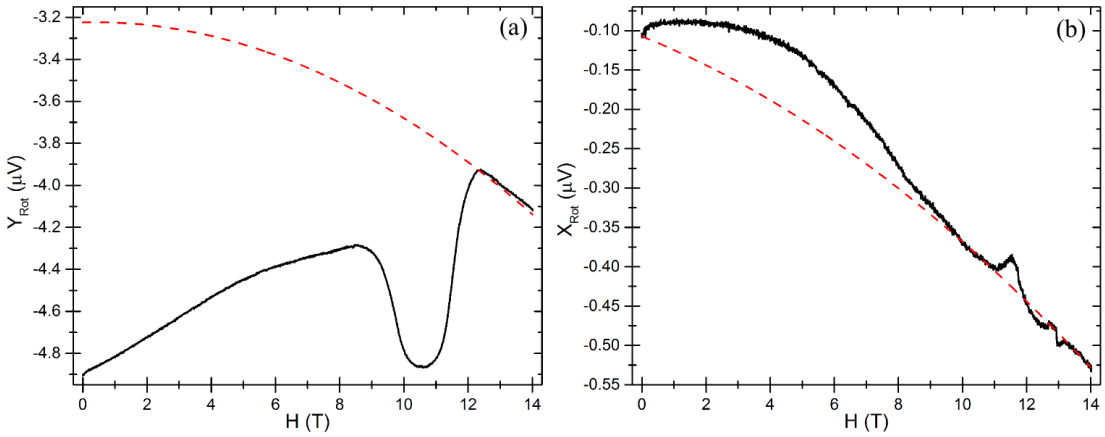

Figure 6.11 *The field dependent (a) out-of-phase and (b) in-phase voltages (black lines) from our susceptometer, corrected for dephasing, containing U_6Fe at 100 mK under a ~0.028 Oe AC field. Overlaid are measured coil backgrounds (red dashed lines) under the same conditions. All measurements conducted at 9777 Hz.*

If a small enough AC field is superimposed on a DC field a material will be in the Campbell regime of linear response[126, 129]. As the AC field oscillates the flux lines enter and exit our sample, yet they only do so across a small distance less than the intervortex spacing. Thus in this regime the flux lines only oscillate harmonically in the local minima of the pinning potentials in a reversible fashion. If the AC amplitude were increased, such that oscillations become large enough to displace flux lines from these pinning potentials, then our sample would enter the non-linear critical state regime with flux flow[130]. The penetration of the AC oscillation of flux lines drops off exponentially into a sample with the characteristic Campbell penetration depth λ_C[48, 129]. For thick samples such as ours the limit of 3D collective pinning can be used where[48]

$$\lambda_C \approx L_c = \frac{2C_{44}C_{66}\xi^2}{nf^2} \tag{6.2}$$

Thus the penetration of the AC oscillation depends explicitly on the elastic moduli of our flux line lattice. Under an AC field of ∼0.028 Oe in the presence of even a small DC field the penetration into our U_6Fe sample has been determined as smaller than the intervortex spacing, indicating we are in the Campbell regime. Indeed evidence of this regime, even in the absence of a DC field, has been noted from the AC field dependence of the χ'' peak in the temperature dependent measurements above.

Calibrated field dependent measurements of U_6Fe in our susceptometer at 100 mK are shown in Figure 6.12. As indicated, H_{c2} can be identified by deviation from the normal state before the sharp transition to diamagnetism in χ'[49]. A weak χ'' loss peak also coincides with this transition as expected for the onset of superconductivity. Evidence for weak collective pinning as discussed in Section 1.4.3 is also evident in χ'. At zero applied DC field near-complete flux exclusion is observed yet as the field grows the AC response weakens. Equations 1.28 & 1.29 indicate that any product of the elastic moduli will initially grow with field, and thus so does λ_C from Equation 6.2. Thus penetration of the AC field oscillation increases with field weakening the full exclusion. On approach of H_{c2} the falling shear modulus C_{66} dominates causing the flux line lattice to soften, yielding an enhancement of pinning and the observable diamagnetic signal known as the peak effect. Hysteresis is also observed indicating the pinning remains to lower fields when ramped down from the normal state, consistent with similar measurements of vortex disordering transitions in literature[45]. A broad loss peak is also seen as the field increases toward the peak effect which is attributed to dissipation

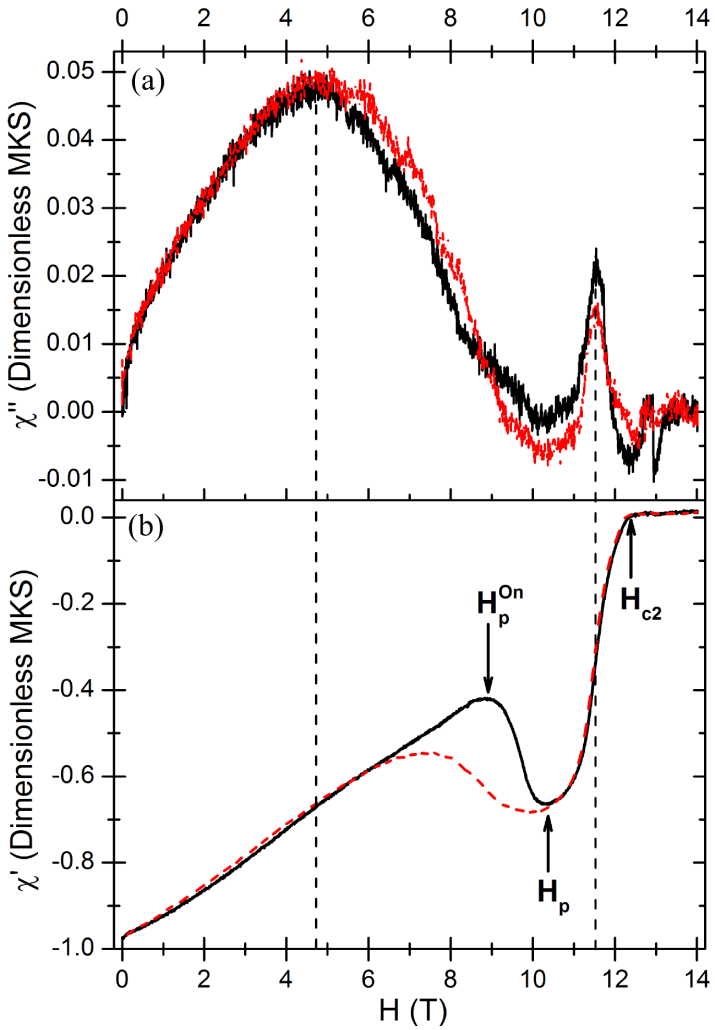

Figure 6.12 *(a) Imaginary and (b) real susceptibility of U_6Fe at 100 mK for field ramps up (black line) and down (red dashed line) indicating hysteretic behaviour. Arrows highlight the critical field H_{c2}, the peak effect H_P and its onset H_P^{On} in the ramp up measure of χ'. Vertical dashed lines highlight occurrence of loss peaks in relation to χ' behaviour.*

from the flux lines oscillating within the pinning sites, peaking at the maximum value of λ_C. The χ'' losses are of very low magnitude which is indicative of the Campbell regime characterised by low loss from pinning[126, 130].

Figure 6.13 illustrates a selection of field sweep measurements at increasing fixed temperatures across both setups. As expected H_{c2} shifts to lower fields with temperature increase along with the peak effect, and the same observed hysteretic behaviour is evident. The diamagnetic signal of the peak effect also grows weaker as temperature is increased indicating collective pinning is becoming less effective, likely due to increased thermal energy depinning flux lines. The low field behaviour also begins to develop more pronounced curvature with

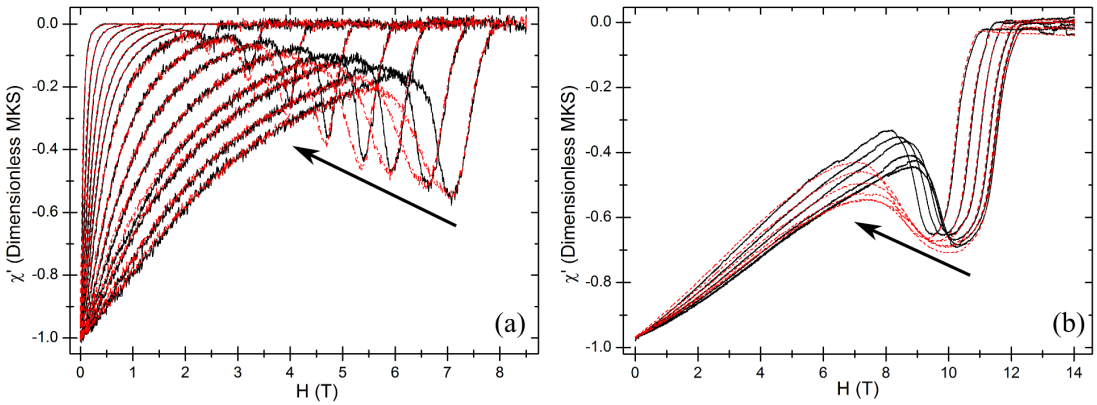

Figure 6.13 *Real susceptibility of U_6Fe for field ramps up (black lines) and down (red dashed lines) at increasing temperatures as indicated by arrows on (a) the high temperature setup spanning 1.9 - 3.9 K and (b) the low temperature setup spanning 40 - 1000 mK.*

temperature increase, which is a signature of further flux ordering behaviour developing from more accessible thermal energy. Continuous transitioning of positional and orientational order of flux lines across H-T space is expected in 3D superconducting samples, yet is difficult to discern precisely through AC measurements alone. Indeed Ganguli with similar field dependent AC measurements resorts to direct observation of the flux lines with scanning tunnelling microscopy in order to discern the complex evolution of the vortex behaviour[45]. At the highest temperatures the peak effect is no longer evident and the entire curve resembles a pure superconducting transition at low H_{c2}.

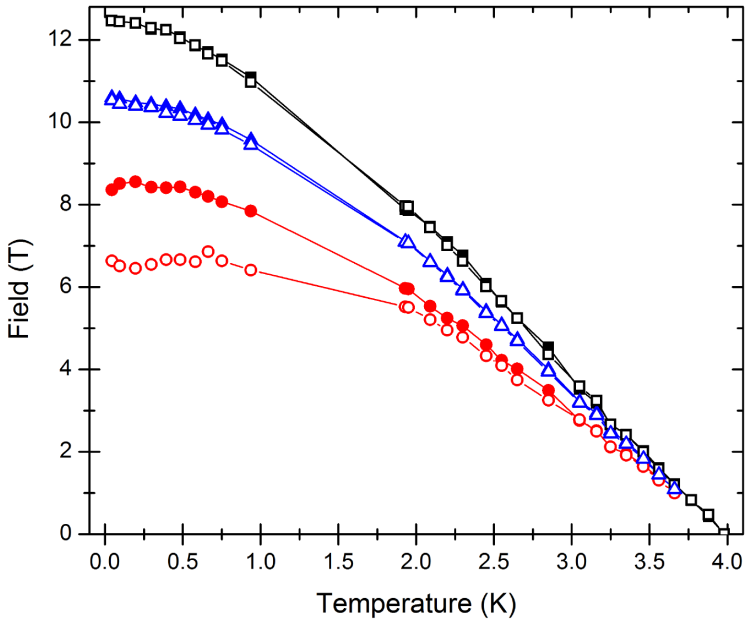

Figure 6.14 *Phase diagram of U_6Fe at ambient pressure for the upper critical field H_{c2} (black squares), peak effect maximum H_P (blue triangles) and onset of the peak effect H_P^{On} (red circles). Field ramps up denoted by solid symbols and down by open symbols.*

The AC measurements allow determination of the H-T phase diagram for U_6Fe, which can be seen in Figure 6.14. As noted above, hysteresis is most prevalent in the onset of the peak effect H_P^{On}, growing larger as temperature drops, and remains minimal for the other parameters. An $H_{c2}(0) = 12.47$ T is observed for the c-axis orientation which is substantially larger than the 10.19 T measured in the a-axis direction of similarly grown crystals by Whitley, as expected from the U_6Fe field anisotropy[110]. The general shape of the $H_{c2}(T)$ curve is also consistent with that observed by Whitley exhibiting linearity near T_c. No anomalous behaviour is evident in H_{c2} in the low temperature regime to provide any evidence of the FFLO state at ambient pressure.

6.4 Susceptibility Measurements under Pressure

Similar field dependent measurements of U_6Fe have been carried out at a range of temperatures under pressure in search of anomalous behaviour associated with formation of the FFLO state. The pressure within the cell is determined by use of a sensitive manganin gauge's resistance, as discussed in Section 2.1.2. Table 6.1 lists the applied pressures at 300 K and the remaining pressure at a base temperature of ∼50 mK due to the pressure medium contraction. Throughout this section pressures will be expressed in terms of their low temperature value. Primarily the effect of pressure on H_{c2} is investigated in the mK regime accessible with the low temperature setup.

Pressure Step	Pressure at 300 K (GPa)	Pressure at ∼50 mK (GPa)
P0	0.07	0.1 x 10^{-3}
P1	0.61	0.20
P2	0.81	0.46
P3	0.92	0.53
P4	0.55	0.14

Table 6.1 *Applied pressures at 300 K and value at ∼50 mK determined from manganin pressure gauge resistance as discussed in Section 2.1.2.*

Figure 6.15 displays field dependent χ' measurements for three temperatures in the mK range under the investigated pressures. H_{c2} increases under initial application of pressure by a fairly dramatic degree for a relatively small pressure. Further shifts at subsequent pressures exhibit less extreme changes. Most notable however is the effect of pressure on the peak effect. The intensity of the

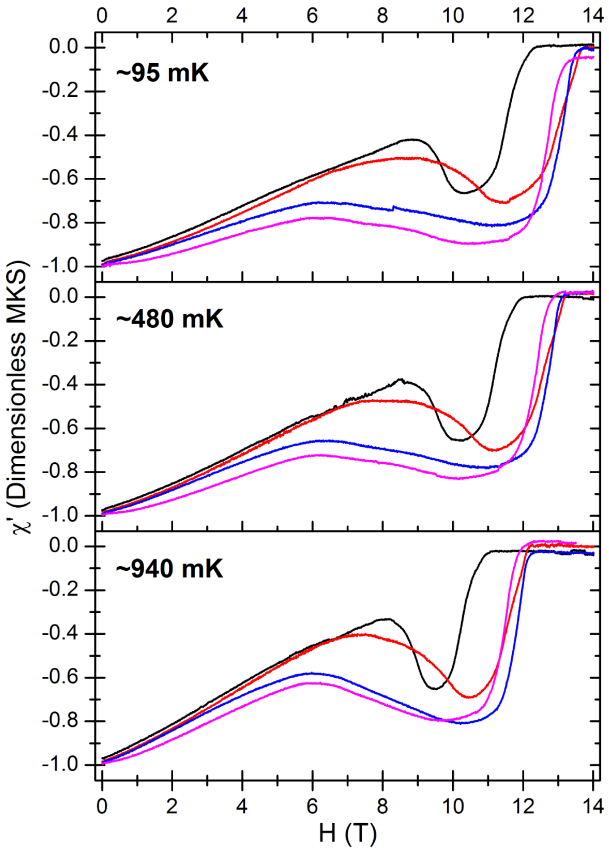

Figure 6.15 *Field dependent real susceptibility of U_6Fe at three temperatures (listed) under various pressures P0 (black), P1 (red), P2 (blue) and P3 (magenta).*

diamagnetism increases in line with pressure which implies more effective pinning of the flux lines. Furthermore, the onset of the peak effect broadens and shifts to lower fields suggesting that collective pinning is dominating over a greater range of fields. Figure 6.16 (b) illustrates the full development of H_P and H_P^{On} across the phase space with pressure. In general the peak effect field increases with the initial application of pressure and then begins to fall, along with H_{c2}, whereas the onset field continually reduces except for the highest pressure. Application of pressure thus appears to be improving the ability of defects/dislocations to pin flux lines in U_6Fe. Indeed a similar enhancement of the pinning under pressure was potentially observed in temperature dependent AC measurements along the a-axis, however the quality of this data prevented many conclusions from being drawn[110].

Figure 6.16 (a) illustrates the full H_{c2}-T phase diagram across the five pressures investigated. The majority of measurements were conducted on the low temperature setup, where onset of FFLO would be most evident, with the full temperature range only measured for pseudo-ambient and the highest pressure

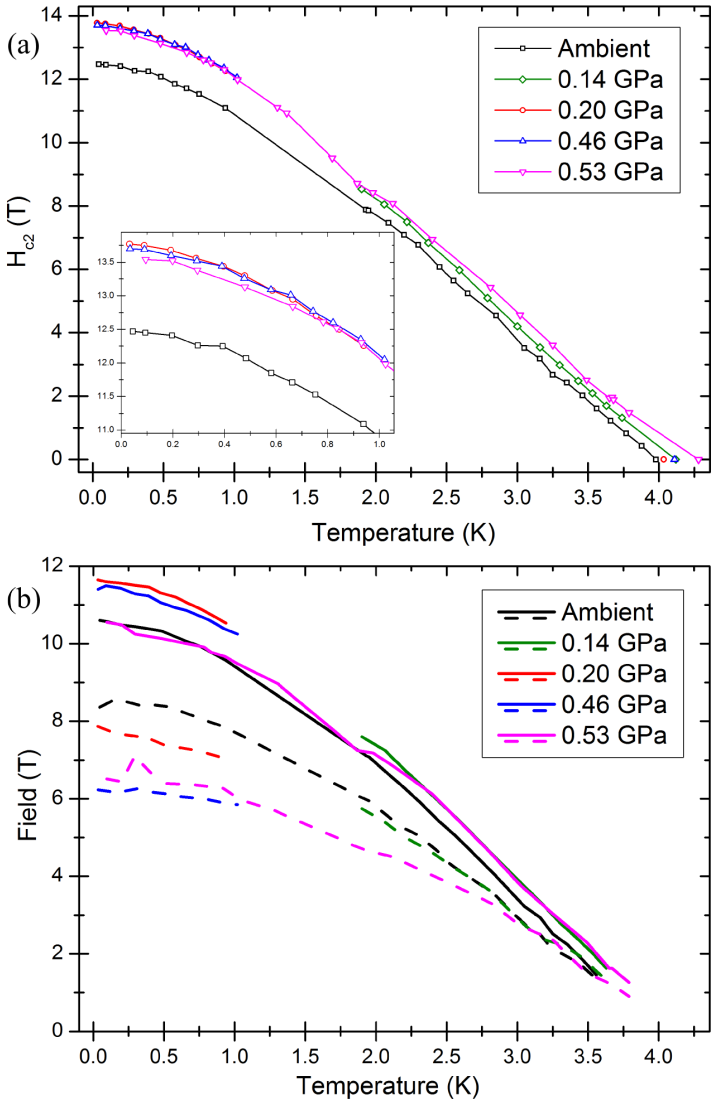

Figure 6.16 *(a) $H_{c2}(T)$ curves under various applied pressures, inset features low temperature regime exhibiting $H_{c2}(0)$ behaviour. (b) Phase diagram for peak effect indicating effect of pressure on H_P (solid lines) and H_P^{On} (dashed lines).*

reached. T_c increases with pressure consistent with previous measurements of U_6Fe[110, 117], although $H_{c2}(0)$ reaches a maximum at ∼0.2 GPa before falling at further pressures. In similar samples of slightly lower quality (RRR∼7.4) measurements along the a-axis indicated H_{c2} and T_c both peaked at ∼1.2 GPa, as can be seen in Figure 6.17[110]. However for these measurements there were no data points across the low pressure range below ∼1.2 GPa so potentially H_{c2} may have peaked at lower pressures as we observe. Indeed the very large increase of H_{c2}, extending it even further beyond the orbital limit, is quite anomalous and occurred under only a small application of pressure indicating there may be very drastic changes occurring at minimal pressures. Regardless, there is no upturn

in $H_{c2}(T)$ at low temperatures indicative of FFLO formation.

A small kink is apparent in the ∼0.53 GPa curve for H_{c2} & H_P at ∼1.87 K, yet this data point is somewhat suspect as it was measured on the low temperature setup beyond the well controlled 1 K upper limit. In this regime up to ∼1.98 K temperature stability was poor, as well as the thermometer calibration likely worsening as has been mentioned in Section 6.2.3. Indeed the measured T_c values for pressure steps P2 & P3 likely underestimate the true T_c as they have only been measured on the low temperature setup, as opposed to the other pressure steps. A final high temperature measurement (P4 ∼0.136 GPa) conducted while depressurising the cell confirms as much by measuring a noticeably higher T_c than the similar pressure P2 ∼0.2 GPa, as can be seen in Figure 6.17. Increase of T_c with pressure has been attributed to CDW suppression in U-based systems[111] and our measurements agree with the general low pressure increase seen in literature[110, 117]; however, we were unable to establish a maximum T_c due to lack of pressures investigated. Thus it remains to be seen whether our sample exhibits a maximum T_c within the limits established previously, as shown in Figure 6.17.

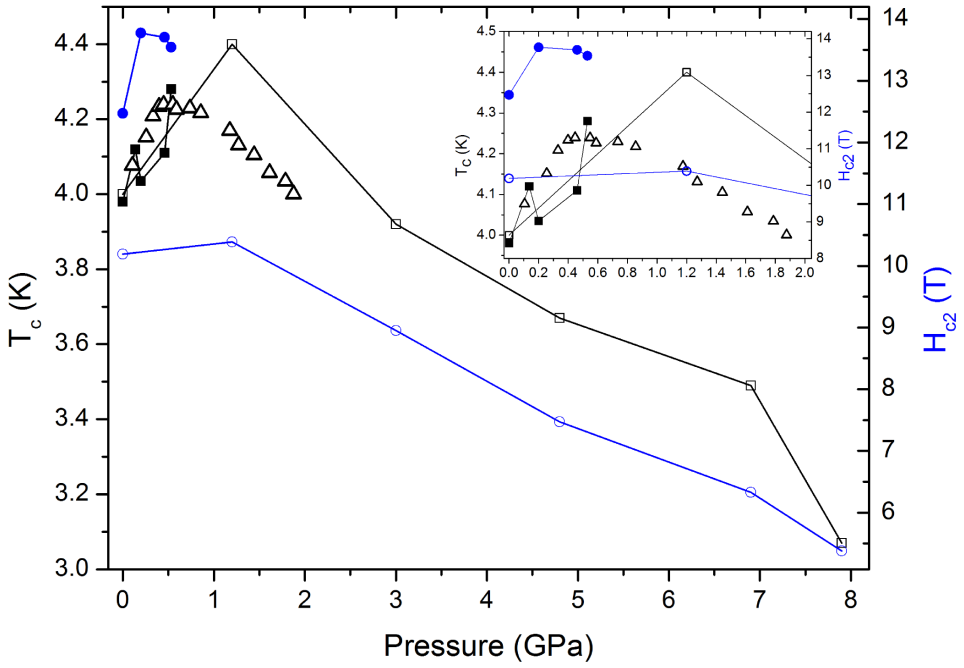

Figure 6.17 *Pressure dependent measurements of H_{c2} (blue curves, right axis) and T_c (black curves, left axis). Filled squares and circles represent T_c and H_{c2} respectively determined along the c-axis by our AC susceptibility measurements. Open squares and circles represent likewise data determined by resistive methods along the a-axis[110]. Open triangles are T_c values of a polycrystalline sample from literature[117]. Inset features zoomed in low pressure region.*

Barring the anomalous initial maximum, H_{c2} is tending to fall as the pressure rises. Such behaviour is indicative of Pauli paramagnetism and approach toward the Pauli limit as the pressure increases. Indeed measurements along the a-axis corroborate this trend with the highest pressures achieved (∼7.9 GPa) falling within the Pauli limit[110]. The zero-temperature reduced field h(0) helps provide an indication of this and can be calculated by

$$h(0) = \frac{H_{c2}(0)}{T_c \left.\frac{dH_{c2}}{dT}\right|_{T_c}} \tag{6.3}$$

As we only have sufficient data at the highest and lowest pressures h(0) can only be calculated for these and are listed in Table 6.2 along with relevant parameters at the other pressure steps. h(0) appears to grow strongly with pressure and is greater than the BCS values (0.72 and 0.69 in the clean and dirty limits respectively) at all pressures, as has been established for U_6Fe previously. Indeed at 0.53 GPa h(0) is even higher than the maximum value observed along the a-axis under pressure by Whitley (h(0) = 0.89 at 7.9 GPa)[110]. Such high h(0) values are an indication of upward curvature of the critical field, although Whitley was able to satisfactorily fit his H_{c2} data to a two-band superconductivity model rather than attributing this to formation of an FFLO state. However, the a-axis h(0) continually grew with pressure and thus may continue to do so along the c-axis as well, which potentially could give rise to an upturn in H_{c2} indicative of FFLO formation. We also see the ratio $H_{c2}(0)/H_{c2}^P$ initially increases and then falls with pressure further indicating approach of the Pauli limit.

Pressure (GPa)	T_c (K)	$H_{c2}(0)$ (T)	$T_c \left.\frac{dH_{c2}}{dT}\right\|_{T_c}$ (T)	h(0)	$\frac{H_{c2}(0)}{H_{c2}^P}$	ξ (Å)
0.1 x 10^{-3}	3.98	12.47	15.20	0.820	1.703	46.5
0.136	4.12	-	14.72	-	-	47.3
0.20	4.035*	13.77	-	-	1.855*	-
0.46	4.11*	13.7	-	-	1.811*	-
0.53	4.28	13.54	13.55	0.999	1.719	49.3

Table 6.2 *Values determined from $H_{c2}(T)$ curves under various pressures (low temperature values listed). Reduced field h(0) determined with Equation 6.3 and coherence length ξ determined with Equation 6.4.* * *Values suspect due to likely underestimation of true T_c from poor thermometer calibration on low temperature setup.*

It is also possible to deduce the coherence length using Ginzburg-Landau theory from

$$\xi = \sqrt{\frac{\phi_0}{2\pi} \frac{1}{T_c \left.\frac{dH_{c2}}{dT}\right|_{T_c}}} \tag{6.4}$$

Where ϕ_0 is the flux quantum. ξ appears to be increasing with pressure very slowly, a trend which was also confirmed in measurements along the a-axis[110]. Potentially increased ξ may play a role in the enhanced pinning observed as this represents the effective size of flux lines. Flux lines of larger dimension would have a higher probability of being captured by nearby pinning sites, however this is merely speculation.

6.5 Conclusions

Calibrated AC susceptibility measurements have been conducted on U_6Fe along the c-axis under pressure utilising our constructed susceptometer in a piston cylinder cell. Clear identification of the upper critical field H_{c2} is evident in these measurements, along with weak collective pinning and the peak effect developing across the temperature range. An enhancement of pinning under pressure is observed. $H_{c2}(T)$ curves are plotted for several applied pressures up to $\sim$0.53 GPa (at base temperature), yet no upturn is observed to provide any indication of the sought after FFLO state. T_c increases with pressure implying the CDW is being suppressed, as in similar systems, yet a maximum was not identified due to lack of pressure points. The reduced field h(0) appears to grow with pressure and yields a very strong value at $\sim$0.53 GPa, indicative of improved upward curvature of the critical field. Similar behaviour has previously been observed along the a-axis and attributed to two-band superconductivity[110], however if such an increase were to continue with pressure it may provide evidence for FFLO formation. Thus further studies to higher pressure should be conducted along the c-axis in order to investigate this possibility.

Notably $H_{c2}(0)$ exhibits an anomalously high increase under very small pressures ($\sim$0.20 GPa) before falling with increased pressure, indicating approach toward the Pauli limit. Similar behaviour has previously been observed for $H_{c2}(0)$ along the a-axis yet not as pronounced[110]. Thus, there appears to be curious $H_{c2}(0)$ behaviour at low pressures implying potentially drastic changes. Further investigation into H_{c2} development in this low pressure regime is warranted along both the c- & a-axis to determine the precise behaviour.

Chapter 7

Conclusions and Future Work

In this thesis we have outlined the design and construction of calibratable susceptometers capable of performing AC susceptibility measurements to the same accuracy as SQUID magnetometers, but within piston cylinder pressure cells. AC susceptibility allows measurement of the time dependent magnetisation and dynamics of a system, making it a useful tool for probing thermodynamic phase transitions, relaxation processes, and losses in a number of materials. Coupled with pressure as a parameter for tuning through multiple phases of a material we were able to investigate a variety of properties and interesting phenomena, such as superconductivity. Thus, our susceptometers have been employed to study the AC susceptibility response of several systems under pressure.

7.1 Electrostatic Doping of $La_{2-x}Sr_xCuO_4$

Susceptometers were implemented in electric double layer capacitor (EDLC) devices in order to investigate the effect of pressure on electrostatic doping of the synthesised superconducting cuprate $La_{1.9}Sr_{0.1}CuO_4$. Utilising modest voltages, shift of the superconducting transition temperature from T_c ∼23.6 K up to a maximum T_c ∼42.8 K was achieved consistent with optimal chemical doping, along with alteration of the normal state response, at ambient pressure. However devices failed to perform reproducibly which has been attributed to poor sealing resulting in a loss of the ionic liquid dielectric. Furthermore,

recent experimental evidence in literature has called into question the validity of electrostatic doping which may instead be attributable to electrochemical reactions, providing another possible reason for lack of repeatability. Due to these issues and time constraints further measurements under pressure were not performed. However implementing EDLC devices within a pressure cell will likely remedy this sealing issue and provide a consistent setup in which to investigate the response under pressure. Thus, reproducible electrostatic doping should be possible and remains as future work to be completed. A careful voltage study of electrostatic doping in the absence of dielectric leakage may help to preclude the possibility of electrochemical reactions, yet this remains to be seen. Additionally a voltage dependent background is evident which may be due to the response of the ionic liquid (which provides an appreciable contribution to the AC signal) or potentially electrochemical reaction of $La_{1.9}Sr_{0.1}CuO_4$ with the ionic liquid. Thus, a voltage study of the ionic liquid response with bare electrodes in an EDLC should be conducted in order to determine the origin of this background.

7.2 Ionic Liquid Glass Transition Mapping

Intended use of EDLC devices under pressure utilising the ionic liquid DEME-TFSI as the pressure transmitting medium necessitated mapping of its glass transition temperature. Effective device operation relies on ion mobility to allow formation of EDLs, thus voltage bias is generally altered 40 - 60 K above the glass transition in order to ensure this. Utilising temperature dependent measurements of expansivity with a sensitive strain gauge and leakage current between plates immersed in DEME-TFSI the shift of the glass transition under pressure was investigated. A pressure-temperature phase diagram of the glass transition, as well as the rubber phase immediately preceding it, was constructed from these measurements up to 0.95 GPa. The highest T_g $\sim$257 K was observed at this pressure along with indications for onset of the rubber phase near room temperature. Our data thus provides an indication of the appropriate temperature to apply voltage bias change under pressure to ensure EDL formation. The magnitude of the leakage current also remained unchanged in the rubber phase, even as it shifted across the temperature range, indicating ion mobility is the same within this regime under pressure. Due to this unchanged ion mobility, the same wait time after bias change used at ambient pressure can still be employed to ensure adequate device operation under pressure.

7.3 Single Chain Magnet $[Co(NCS)_2(pyridine)_2]_n$

Single chain magnets (SCM) are 1D polymeric chains exhibiting superparamagnetism with slow magnetic relaxation and have promising applications for high-density memory storage. To date minimal investigation of these materials under pressure has been performed, yet results suggest key properties may be improved. Thus, the susceptometer was employed in a piston cylinder cell to investigate development of the relaxation time and energy barrier to spin reversal in the SCM $[Co(NCS)_2(pyridine)_2]_n$ under pressure.

Initially SCM behaviour appeared to be improved at low pressures with an increase of peak intensity and the onset temperature observed in AC susceptibility measurements, indicative of improved spin alignment along the chain. However at a threshold pressure of 0.44 GPa the susceptibility falls, as well as the peak temperature reducing with increased pressure. Additionally a distinct asymmetry develops in χ' at this pressure which is attributed to coexistence of the SCM with a new high pressure phase, independently observed in crystallographic measurements by the Murrie group[109]. At 0.60 GPa the asymmetry resolves into two distinct peaks attributable to each phase, with indications of the relative phase composition shifting with pressure. Independent AC susceptibility measurements performed by the Murrie group confirm the reproducibility of this behaviour and indicate full conversion to the new phase at high pressure (1.3 GPa)[109]. Pressure induced changes are fully reversible. Frequency dependent measurements fitted well to thermally activated Arrhenius laws indicating the characteristic spin flipping time τ_0 increases by several orders of magnitude before plateauing. However simultaneously the spin reversal activation energy E_a falls, which implies pressure is not conducive to longer relaxation times or improved SCM behaviour for applications. It should be noted however that the phase coexistence may be obscuring these results due to the possibility of closely overlapping peaks in the broad χ'' signal. Thus, AC susceptibility measurements should be performed to higher pressures where only the new phase is present in order to determine its characteristic peak behaviour, and allow separation of individual phases within the coexistence regime.

Furthermore, the new phase should be characterised at high pressures in order to determine if it exhibits more favourable SCM properties. Indeed at 0.60 GPa, where the new phase is most evident, an increase of E_a with a still relatively large τ_0 is observed implying the most promising SCM behaviour for applications.

7.4 U_6Fe AC Susceptibility

U_6Fe is a heavy fermion superconductor exhibiting large H_{c2} values, exceeding both the orbital and Pauli limits, and a confirmed charge density wave (CDW). These properties make it a promising candidate for inducing the modulated superconductivity of the theorised Fulde-Ferrel-Larkin-Ovchinnikov (FFLO) state; which emerges as a second transition below H_{c2}. Thus, AC susceptibility measurements were performed mapping the upper critical field $H_{c2}(T)$ along the c-axis under various pressures in the hope of suppressing the CDW and forming of an FFLO state.

In addition to determination of H_{c2} AC susceptibility measurements illustrated the presence of weak collective pinning and the peak effect developing across the investigated temperature range. Under pressure an enhancement of this pinning was observed through increased diamagnetism of the peak effect and broadening of the collective pinning regime. T_c also increases with pressure, as observed previously for U_6Fe, indicative of CDW suppression as in similar U based systems; however, a maximum value was not identified due to lack of pressures investigated. Utilising these measurements $H_{c2}(T)$ is mapped up to pressures of $\sim$0.53 GPa. No additional features, beyond those accounted for by weak collective pinning, nor a characteristic upturn expected for development of the FFLO state is observed. However the reduced field h(0) determined from such curves increased along with pressure, reaching a maximum value of 0.999 implying increased upward curvature of the critical field. A similar increase of h(0) along the a-axis has previously been observed, although not to such high values, and was attributed to two-band superconductivity[110]. However if h(0) were to increase further with pressure an upturn indicative of the FFLO state could develop as opposed to merely being consistent with two-band superconductivity. Further measurements should be conducted at higher pressures in order to investigate the marked increase of h(0) along the c-axis and potential development of an FFLO state.

In general the zero temperature critical field $H_{c2}(0)$ falls with pressure indicative of approach toward the Pauli limit, however an anomalously large increase is initially seen at a low pressure of $\sim$0.20 GPa. A similar low pressure increase has also been observed along the a-axis previously although not as marked. Thus, potentially drastic changes may be occurring in this low pressure regime and further measurements at similar pressures should be carried out along both the a- & c-axis in order to investigate this behaviour.

Appendix A

Single Chain Magnet Measurements

		$T_{\chi''peak}$ (K) at each Pressure Step							
Frequency (Hz)	τ (ms)	P0	P1	P2	P3	P4	P5	P6	P7
1488	0.107	3.30	3.34	3.97	4.74	4.34	4.28	4.02	3.24
997	0.159	3.25	3.28	3.87	4.60	4.16	4.13	3.89	3.20
498	0.320	3.16	3.18	3.69	4.33	3.92	3.92	3.73	3.11
246.7	0.637	3.02	3.08	3.53	4.05	3.74	3.75	3.61	3.03
40	3.98	2.90	2.92	3.17	3.48	3.28	3.28	3.24	2.85
30	5.31	2.88	2.91	3.13	3.41	3.24	3.20	3.23	2.81
20	7.96	2.82	2.88	3.07	3.33	3.21	3.12	3.15	2.77
10	15.92	2.70	2.85	3.01	3.23	3.05	3.04	3.06	2.63

Table A.1 *χ'' peak temperature at various frequencies for measured pressure steps, corresponding pressures listed in Table 5.1, of the SCM $[Co(NCS)_2(pyridine)_2]_n$. Relaxation time τ determined from frequencies using $\omega\tau = 1$.*

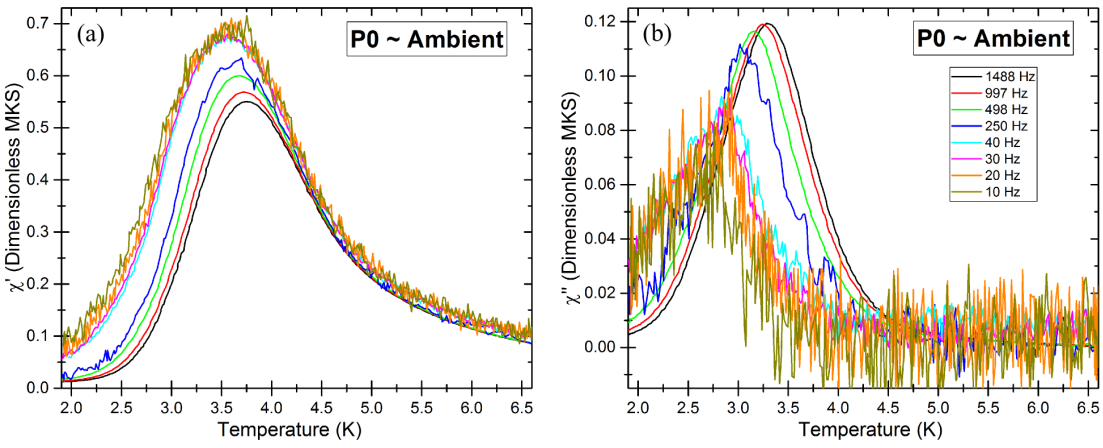

Figure A.1 *Temperature dependent (a) real and (b) imaginary susceptibility measurements of $[Co(NCS)_2(pyridine)_2]_n$ sample under various frequencies (listed, top right) at pressure P0$\sim 1 \times 10^{-3}$ GPa (base temperature values).*

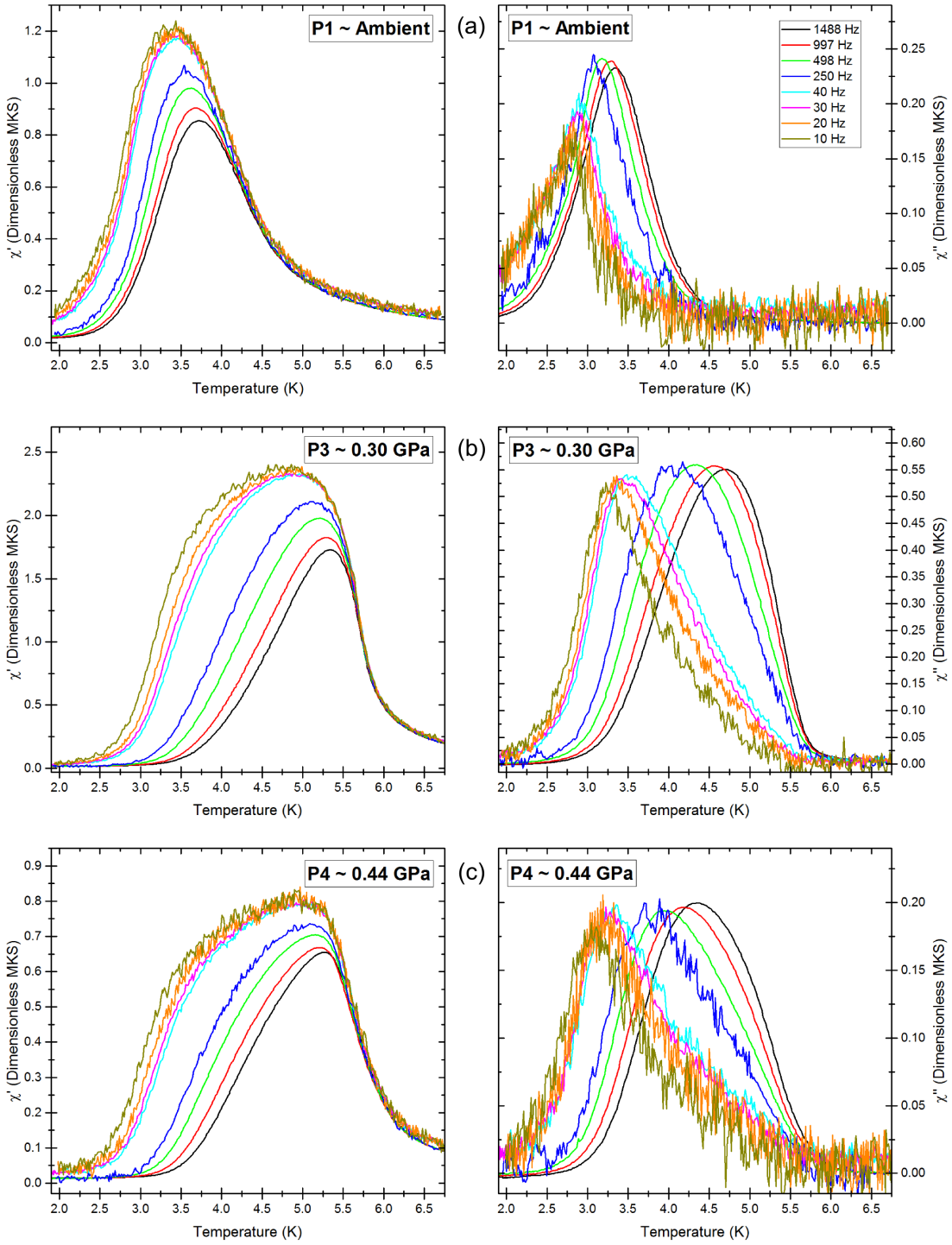

Figure A.2 *Temperature dependent real and imaginary susceptibility measurements of $[Co(NCS)_2(pyridine)_2]_n$ sample under various frequencies (listed, top right) at selected pressures (base temperature values) (a) P1∼1 × 10^{-3} GPa, (b) P3∼0.30 GPa and (c) P4∼0.44 GPa.*

Bibliography

[1] D. M. McCann, M. Misek, K. V. Kamenev, and A. D. Huxley, "Pressure-Temperature Phase Diagram of Ionic Liquid Dielectric DEME-TFSI," *Physics Procedia*, vol. 75, pp. 252–258, 2015. [Online]. Available: http://linkinghub.elsevier.com/retrieve/pii/S1875389215016703

[2] D. Martien, "Introduction to: ac susceptibility," *Quantum Design*, 1994. [Online]. Available: http://scholar.google.com/scholar?hl=en{&}btnG=Search{&}q=intitle:Introduction+to+AC+Susceptibility{#}0

[3] M. Balanda, "AC susceptibility studies of phase transitions and magnetic relaxation: Conventional, molecular and low-dimensional magnets," *Acta Physica Polonica A*, vol. 124, no. 6, pp. 964–976, 2013.

[4] M. Nikolo, "Superconductivity: A guide to alternating current susceptibility measurements and alternating current susceptometer design," *American Journal of Physics*, vol. 63, no. 1, p. 57, 1995. [Online]. Available: http://link.aip.org/link/?AJP/63/57/1{&}Agg=doi

[5] P. Ford and G. Saunders, "What Causes Superconductivity?" in *The Rise of the Superconductors*. CRC Press, 2005, ch. 6, pp. 83–119.

[6] J. Bardeen, L. N. Cooper, and J. R. Schrieffer, "Theory of Superconductivity," *Physical Review*, vol. 108, no. 5, pp. 1175–1204, dec 1957. [Online]. Available: http://prola.aps.org/abstract/PR/v108/i5/p1175{_}1

[7] C. P. J. Poole, H. A. Farach, and R. J. Creswick, *Superconductivity*. Academic Press, 1995.

[8] J. G. Bednorz and K. A. Muller, "Possible High Tc Superconductivity in the Ba-La-Cu-O System," *European Physical Journal B*, vol. 193, pp. 189–193, 1986.

[9] K. Ueno, S. Nakamura, H. Shimotani, A. Ohtomo, N. Kimura, T. Nojima, H. Aoki, Y. Iwasa, and M. Kawasaki, "Electric-field-induced superconductivity in an insulator." *Nature materials*, vol. 7, no. 11, pp. 855–858, nov 2008. [Online]. Available: http://www.ncbi.nlm.nih.gov/pubmed/18849974

[10] P. C. Canfield, "Still alluring and hard to predict at 100," *Nature materials*, vol. 10, no. 4, pp. 259–261, apr 2011. [Online]. Available: http://www.ncbi.nlm.nih.gov/pubmed/21430665

[11] K. Ueno, S. Nakamura, H. Shimotani, H. T. Yuan, N. Kimura, T. Nojima, H. Aoki, Y. Iwasa, and M. Kawasaki, "Discovery of superconductivity in KTaO by electrostatic carrier doping." *Nature nanotechnology*, vol. 6, no. 7, pp. 408–412, jul 2011. [Online]. Available: http://www.ncbi.nlm.nih.gov/pubmed/21602813

[12] R. E. Glover and M. D. Sherrill, "Changes in Superconducting Critical Temperature Produced by Electrostatic Charging," *Physical Review Letters*, vol. 5, no. 6, pp. 248–250, 1960.

[13] K. Prassides, "Condensed matter physics: superconductivity at the double." *Nature nanotechnology*, vol. 6, no. 7, pp. 400–401, jul 2011. [Online]. Available: http://www.ncbi.nlm.nih.gov/pubmed/21731072

[14] C. H. Ahn, "Electrostatic Modulation of Superconductivity in Ultrathin GdBa2Cu3O7-x Films," *Science*, vol. 284, no. 5417, pp. 1152–1155, may 1999. [Online]. Available: http://www.sciencemag.org/cgi/doi/10.1126/science.284.5417.1152

[15] J. T. Ye, S. Inoue, K. Kobayashi, Y. Kasahara, H. T. Yuan, H. Shimotani, and Y. Iwasa, "Liquid-gated interface superconductivity on an atomically flat film." *Nature materials*, vol. 9, no. 2, pp. 125–128, feb 2010. [Online]. Available: http://www.ncbi.nlm.nih.gov/pubmed/19935665

[16] Y. Kasahara, T. Nishijima, T. Sato, Y. Takeuchi, J. Ye, H. Yuan, H. Shimotani, and Y. Iwasa, "Electric-Field-Induced Superconductivity Detected by Magnetization Measurements of an Electric-Double-Layer Capacitor," *Journal of the Physical Society of Japan*, vol. 80, no. 2, p. 023708, feb 2011. [Online]. Available: http://jpsj.ipap.jp/link?JPSJ/80/023708/

[17] C. P. J. Poole, *Handbook of Superconductivity*, C. P. J. Poole, Ed. Academic Press, 2000.

[18] P. Ford and G. Saunders, *The Rise of the Superconductors*. CRC Press, 2005.

[19] N. B. Kopnin, *Theory of Superconductivity*. Aalto University, School of Science and Technology, Department of Applied Physics, 2010.

[20] E. Helfand and N. R. Werthamer, "Temperature and purity dependence of the superconducting critical field, Hc2. II," *Physical Review*, vol. 147, no. 1, pp. 288–294, 1966.

[21] A. M. Clogston, "Upper limit for the critical field in hard superconductors," *Physical Review Letters*, vol. 9, no. 6, pp. 266–267, 1962.

[22] D. Saint-James, G. Sarma, and E. J. Thomas, *Type II Superconductivity.* New York: Pergamon Press, 1969.

[23] C. H. Ahn, J. M. Triscone, and J. Mannhart, "Electric field effect in correlated oxide systems." *Nature*, vol. 424, no. 6952, pp. 1015–1018, aug 2003. [Online]. Available: http://www.ncbi.nlm.nih.gov/pubmed/12944958

[24] N. Reyren, S. Thiel, A. D. Caviglia, L. F. Kourkoutis, G. Hammerl, C. Richter, C. W. Schneider, T. Kopp, A.-S. Rüetschi, D. Jaccard, M. Gabay, D. A. Muller, J. M. Triscone, and J. Mannhart, "Superconducting interfaces between insulating oxides." *Science (New York, N.Y.)*, vol. 317, no. 5842, pp. 1196–1199, aug 2007. [Online]. Available: http://www.ncbi.nlm.nih.gov/pubmed/17673621

[25] H. Yuan, H. Shimotani, A. Tsukazaki, A. Ohtomo, M. Kawasaki, and Y. Iwasa, "High-Density Carrier Accumulation in ZnO Field-Effect Transistors Gated by Electric Double Layers of Ionic Liquids," *Advanced Functional Materials*, vol. 19, no. 7, pp. 1046–1053, apr 2009. [Online]. Available: http://doi.wiley.com/10.1002/adfm.200801633

[26] D. Grahame, "The electrical double layer and the theory of electrocapillarity." *Chemical Reviews*, vol. 41, pp. 441–501, 1947. [Online]. Available: http://pubs.acs.org/doi/abs/10.1021/cr60130a002

[27] A. S. Dhoot, J. D. Yuen, M. Heeney, I. McCulloch, D. Moses, and A. J. Heeger, "Beyond the metal-insulator transition in polymer electrolyte gated polymer field-effect transistors." *Proceedings of the National Academy of Sciences of the United States of America*, vol. 103, no. 32, pp. 11 834–11 837, aug 2006. [Online]. Available: http://www.pubmedcentral.nih.gov/articlerender.fcgi?artid=1567663{&}tool=pmcentrez{&}rendertype=abstract

[28] M. Panzer and C. Frisbie, "High Carrier Density and Metallic Conductivity in Poly(3-hexylthiophene) Achieved by Electrostatic Charge Injection," *Advanced Functional Materials*, vol. 16, no. 8, pp. 1051–1056, may 2006. [Online]. Available: http://doi.wiley.com/10.1002/adfm.200600111

[29] H. Shimotani, H. Asanuma, A. Tsukazaki, A. Ohtomo, M. Kawasaki, and Y. Iwasa, "Insulator-to-metal transition in ZnO by electric double layer gating," *Applied Physics Letters*, vol. 91, no. 8, p. 082106, 2007. [Online]. Available: http://link.aip.org/link/APPLAB/v91/i8/p082106/s1{&}Agg=doi

[30] R. Misra, M. McCarthy, and A. F. Hebard, "Electric field gating with ionic liquids," *Applied Physics Letters*, vol. 90, no. 5, p. 052905, 2007. [Online]. Available: http://link.aip.org/link/APPLAB/v90/i5/p052905/s1{&}Agg=doi

[31] A. T. Bollinger, G. Dubuis, J. Yoon, D. Pavuna, J. Misewich, and I. Božović, "Superconductor-insulator transition in La2-xSrxCuO4 at the pair quantum resistance." *Nature*, vol. 472, no. 7344, pp. 458–460, apr 2011. [Online]. Available: http://www.ncbi.nlm.nih.gov/pubmed/21525929

[32] J. Fan and P. S. Fedkiw, "Electrochemical impedance spectra of full cells: Relation to capacity and capacity-rate of rechargeable Li cells using LiCoO2, LiMn2O4, and LiNiO2 cathodes," *Journal of Power Sources*, vol. 72, no. 2, pp. 165–173, 1998.

[33] D. Qu and H. Shi, "Studies of activated carbons used in double-layer capacitors," *Journal of Power Sources*, vol. 74, pp. 99–107, 1998.

[34] T. Sato, G. Masuda, and K. Takagi, "Electrochemical properties of novel ionic liquids for electric double layer capacitor applications," *Electrochimica Acta*, vol. 49, no. 21, pp. 3603–3611, sep 2004. [Online]. Available: http://linkinghub.elsevier.com/retrieve/pii/S0013468604003469

[35] W. Shi, J. Ye, J. G. Checkelsky, C. Terakura, and Y. Iwasa, "Transport Properties of Polymer Semiconductor Controlled by Ionic Liquid as a Gate Dielectric and a Pressure Medium," *Advanced Functional Materials*, vol. 24, no. 14, pp. 2005–2012, nov 2014. [Online]. Available: http://doi.wiley.com/10.1002/adfm.201302954

[36] Y. Yoshimura, T. Takekiyo, Y. Imai, and H. Abe, "Pressure-Induced Spectral Changes of Room-Temperature Ionic Liquid , N,N-Diethyl-N-methyl-N-(2-methoxyethyl) ammonium Bis(trifluoromethylsulfonyl)imide, [DEME][TFSI]," *Journal of Physical Chemistry C*, vol. 116, pp. 2097–2101, 2012.

[37] K. Kamenev, "Personal Communication," 2013.

[38] R. B. Goldfarb and J. V. Minervini, "Calibration of ac susceptometer for cylindrical specimens," *Review of Scientific Instruments*, vol. 55, no. 5, p. 761, 1984. [Online]. Available: http://scitation.aip.org/content/aip/journal/rsi/55/5/10.1063/1.1137813

[39] "AC Susceptibility Measurements in High-Tc Superconductors," Department of Physics, University of Florida, Tech. Rep., 2012. [Online]. Available: http://www.phys.ufl.edu/courses/phy4803L/group{_}II/high{_}Tc/hightc.pdf

[40] C. Pfleiderer, "Miniature ac susceptometers for use inside clamp type pressure cells," *Review of Scientific Instruments*, vol. 68, no. 3, p. 1532, 1997. [Online]. Available: http://link.aip.org/link/RSINAK/v68/i3/p1532/s1{&}Agg=doi

[41] K.-H. Müller, *Detailed Theory of the Magnetic Response of High-Temperature Ceramic Superconductors*. Boston, MA: Springer US,

1991, pp. 229–250. [Online]. Available: http://dx.doi.org/10.1007/978-1-4899-2379-0{_}10

[42] A. I. Larkin and Y. N. Ovchinnikov, "Pinning in type II superconductors," *Journal of Low Temperature Physics*, vol. 34, no. 3-4, pp. 409–428, 1979.

[43] M. Tinkham, *Introduction to Superconductivity*, 2nd ed. McGraw-Hill, 1996.

[44] J. B. Ketterson and S. N. Song, "Flux Pinning and flux motion," in *Superconductivity*. Cambridge: Cambridge University Press, 1999, pp. 110–139. [Online]. Available: http://ebooks.cambridge.org/ref/id/CBO9781139171090

[45] S. C. Ganguli, H. Singh, G. Saraswat, R. Ganguly, V. Bagwe, P. Shirage, A. Thamizhavel, and P. Raychaudhuri, "Disordering of the vortex lattice through successive destruction of positional and orientational order in a weakly pinned Co0.0075NbSe2 single crystal," *Scientific Reports*, vol. 5, no. April, p. 10613, jun 2015. [Online]. Available: http://www.nature.com/articles/srep10613

[46] N. Lutke-Entrup, R. Blaauwgeers, B. Placais, P. Mathieu, Y. Simon, M. Krusius, S. Kambe, and A. Huxley, "High-frequency vortex dynamics and flux-flow resistivity in UPt3," *Physica B*, vol. 288, pp. 527–528, 2000.

[47] N. Lutke-Entrup, B. Plaçais, P. Mathieu, and Y. Simon, "RF-studies of vortex dynamics in isotropic type-II superconductors," *Physica B*, vol. 255, pp. 75–85, 1998.

[48] C. J. Van Der Beek, V. B. Geshkenbein, and V. M. Vinokur, "Linear and nonlinear ac response in the superconducting mixed state," *Physical Review B*, vol. 48, no. 5, pp. 3393–3403, 1993.

[49] F. Gömöry, "Characterization of high-temperature superconductors by AC susceptibility measurements," *Superconductor Science and Technology*, vol. 10, no. 8, p. 523, 1999. [Online]. Available: http://iopscience.iop.org/0953-2048/10/8/001$\delimiter"026E30F$nhttp://iopscience.iop.org/0953-2048/10/8/001/pdf/0953-2048{_}10{_}8{_}001.pdf

[50] K. Murata, K. Yokogawa, H. Yoshino, S. Klotz, P. Munsch, A. Irizawa, M. Nishiyama, K. Iizuka, T. Nanba, T. Okada, Y. Shiraga, and S. Aoyama, "Pressure transmitting medium Daphne 7474 solidifying at 3.7 GPa at room temperature," *Review of Scientific Instruments*, vol. 79, no. 8, pp. 3–9, 2008.

[51] N. Tateiwa and Y. Haga, "Evaluations of pressure-transmitting media for cryogenic experiments with diamond anvil cell," *Review of Scientific Instruments*, vol. 80, no. 12, pp. 1–9, 2009.

[52] T. Matsumoto, Y. Uwatoko, and M. Hedo, "Fabrication of 4 GPa Class Non Magnetic High Pressure Clamp Cell," *Stress (MPa)*, vol. 1000, p. 500,

2002. [Online]. Available: http://www.nims.go.jp/units/erm/project{_}1/MZMT/matsumoto.files/ACHPR.pdf

[53] L. H. Dmowski and E. Litwin-Staszewska, "The variation of the pressure coefficient of manganin sensors at low temperatures," *Measurement Science and Technology*, vol. 10, no. 5, pp. 343–347, 1999.

[54] D. H. Newhall, "Manganin high-pressure sensors," *Instruments and Control Systems*, 1962.

[55] O. E. Andersson and B. Sundqvist, "Low temperature calibration of Manganin pressure gauges," *Review of Scientific Instruments*, vol. 68, no. 2, p. 1344, 1997. [Online]. Available: http://scitation.aip.org/content/aip/journal/rsi/68/2/10.1063/1.1147868

[56] D. Wohlleben and M. B. Maple, "Application of the faraday method to magnetic measurements under pressure," *Review of Scientific Instruments*, vol. 42, no. 11, pp. 1573–1578, 1971.

[57] A. T. Rowley and A. Myers, "A SQUID-based high pressure magnetic susceptometer," *Journal of Physics E: Scientific Instruments*, vol. 20, p. 146, 1987. [Online]. Available: http://iopscience.iop.org/0022-3735/20/2/006

[58] J. S. Schilling, J. Diederichs, S. Klotz, and R. Sieburger, *Ac Susceptibility Studies of Superconducting Properties Under High Hydrostatic Pressure*. Boston, MA: Springer US, 1991, pp. 107–128. [Online]. Available: http://dx.doi.org/10.1007/978-1-4899-2379-0{_}5

[59] N. Kimura, N. Kabeya, H. Aoki, K. Ohyama, M. Maeda, H. Fujii, M. Kogure, T. Asai, T. Komatsubara, T. Yamamura, and I. Satoh, "Quantum critical point and unusual phase diagram in the itinerant-electron metamagnet UCoAl," *Physical Review B*, vol. 92, no. 3, p. 035106, 2015. [Online]. Available: http://link.aps.org/doi/10.1103/PhysRevB.92.035106

[60] S. Arumugam, N. Manivannan, A. Murugeswari, S. Arumugam, N. Manivannan, and A. Murugeswari, "Simple uniaxial pressure device for ac-susceptibility measurements suitable for closed cycle refrigerator system," *Review of Scientific Instruments*, vol. 78, no. 6, p. 63906, 2007. [Online]. Available: http://dx.doi.org/10.1063/1.2745726

[61] P. L. Alireza and S. R. Julian, "Susceptibility measurements at high pressures using a microcoil system in an anvil cell," *Review of Scientific Instruments*, vol. 74, no. 11, p. 4728, 2003. [Online]. Available: http://scitation.aip.org/content/aip/journal/rsi/74/11/10.1063/1.1614861

[62] T. Stobiecki, "Fundamentals of Magnetism," Krakow, Poland, Tech. Rep., 2004. [Online]. Available: http://goo.gl/IXexpw

[63] R. B. Goldfarb, M. Lelental, and C. A. Thompson, *Alternating-Field Susceptometry and Magnetic Susceptibility of Superconductors*. Boston, MA: Springer US, 1991, pp. 49–80. [Online]. Available: http://dx.doi.org/10.1007/978-1-4899-2379-0{_}3

[64] D. X. Chen, J. A. Brug, and R. B. Goldfarb, "Demagnetizing factors for cylinders," *IEEE Transactions on Magnetics*, vol. 27, no. 4, pp. 3601–3619, 1991.

[65] D. Chen, E. Pardo, and A. Sanchez, "Demagnetizing factors for rectangular ferromagnetic prisms," *Journal of Applied Physics*, vol. 83, no. 1998, pp. 3432–3434, 1998.

[66] D. X. Chen, E. Pardo, and A. Sanchez, "Demagnetizing factors of rectangular prisms and ellipsoids," *IEEE Transactions on Magnetics*, vol. 38, no. 4 II, pp. 1742–1752, 2002.

[67] E. Pardo, D. X. Chen, and A. Sanchez, "Demagnetizing factors for square bars," *IEEE Transactions on Magnetics*, vol. 40, no. 3, pp. 1491–1498, 2004.

[68] C. E. Weir, "Transitions and Phases of Polytetrafluoroethylene (Teflon)," *Journal of Research of the National Bureau of Standards*, vol. 50, no. 2, pp. 95–97, 1953.

[69] Boedeker Plastics Inc., "PEEK (Polyether Ether Ketone) Specifications." [Online]. Available: http://www.boedeker.com/peek{_}p.htm

[70] J. C. Maxwell, "To find M by Elliptic Integrals," in *A Treatise on Electricity and Magnetism Volume 2*, 3rd ed. New York: Dover Publications, 1954, pp. 338–340.

[71] R. Weaver, "Multi-Layer Coil Inductance Calculator," 2014. [Online]. Available: http://electronbunker.ca/InductanceCalcML.html

[72] Z. Popović and B. D. Popović, "Chapter 20 - The Skin Effect," in *Introductory Electromagnetics*. Prentice Hall, 2000.

[73] J. D. Jackson, *Classical Electrodynamics*, 3rd ed. John Wiley& Sons, 1995.

[74] NDT Resource Center, "Depth of Penetration & Current Density," 2016. [Online]. Available: https://www.nde-ed.org/EducationResources/CommunityCollege/EddyCurrents/Physics/depthcurrentdensity.htm

[75] L. Civale, T. K. Worthington, L. Krusin-Elbaum, and F. Holtzberg, *Nonlinear A.C. Susceptibility Response Near the Irreversibility Line*. Boston, MA: Springer US, 1991, pp. 313–332. [Online]. Available: http://dx.doi.org/10.1007/978-1-4899-2379-0{_}15

[76] J. R. Clem, *Ac Losses in Type-II Superconductors*. Boston, MA: Springer US, 1991, pp. 177–211. [Online]. Available: http://dx.doi.org/10.1007/978-1-4899-2379-0{_}8

[77] T. Sato, G. Masuda, and K. Takagi, "Corrigendum to "Electrochemical properties of novel ionic liquids for electric double layer capacitor applications"," *Electrochimica Acta*, vol. 53, no. 14, pp. 4934–4935, 2008.

[78] I. Krossing, J. M. Slattery, C. Daguenet, P. J. Dyson, A. Oleinikova, and H. Weingärtner, "Why are ionic liquids liquid? A simple explanation based on lattice and solvation energies." *Journal of the American Chemical Society*, vol. 128, no. 41, pp. 13 427–34, oct 2006. [Online]. Available: http://www.ncbi.nlm.nih.gov/pubmed/17031955

[79] J. C. Dyre, "Colloquium: The glass transition and elastic models of glass-forming liquids," *Reviews of Modern Physics*, vol. 78, no. 3, pp. 953–972, 2006.

[80] J. Ye, "Personal Communication," 2014.

[81] A. Saleem and S. T. Hussain, "Review the High Temperature Superconductor (HTSC) Cuprates-Properties and Applications," *Journal of Surfaces and Interfaces of Materials*, vol. 1, no. 2, pp. 97–119, 2013. [Online]. Available: http://openurl.ingenta.com/content/xref?genre=article{&}issn=2164-7542{&}volume=1{&}issue=2{&}spage=97

[82] K. M. Shen and J. C. S. Davis, "Cuprate high-Tc superconductors," *Materials Today*, vol. 11, no. 9, pp. 14–21, 2008.

[83] H. Wu, M. Buchholz, C. Trabant, C. Chang, A. Komarek, F. Heigl, M. Zimmermann, M. Cwik, F. Nakamura, M. Braden, and C. Schüßler-Langeheine, "Charge stripe order near the surface of 12-percent doped La2-xSrxCuO4," *Nature Communications*, vol. 3, p. 1023, 2012.

[84] P. M. C. Rourke, I. Mouzopoulou, X. Xu, C. Panagopoulos, Y. Wang, B. Vignolle, C. Proust, E. V. Kurganova, U. Zeitler, Y. Tanabe, T. Adachi, Y. Koike, and N. E. Hussey, "Phase-fluctuating superconductivity in overdoped La2-xSrxCuO4," *Nature Physics*, vol. 7, no. 6, pp. 455–458, 2011.

[85] T. R. Lemberger, I. Hetel, A. Tsukada, M. Naito, and M. Randeria, "Superconductor-to-metal quantum phase transition in overdoped La2-xSrxCuO4," *Physical Review B - Condensed Matter and Materials Physics*, vol. 83, no. 14, pp. 2–5, 2011.

[86] R. Gilardi, "Inelastic and small angle neutron scattering Study of the La2-xSrxCuO4 High-Tc Superconductor in a magnetic field," Ph.D. dissertation, Swiss Federal Institute of Technology, Zurich, 2004.

[87] R. Gilardi, S. Streule, N. Momono, M. Oda, and J. Mesot, "Doping dependence of the vortex glass and sublimation transitions in the high-Tc superconductor La2-xSrxCuO4 as determined from macroscopic measurements," *European Physical Journal B*, vol. 47, no. 2, pp. 231–237, 2005.

[88] A. T. Bollinger, G. Dubuis, J. Yoon, D. Pavuna, J. Misewich, and I. Božović, "Supplementary Information - Superconductor-insulator transition in La2-xSrxCuO4 at the pair quantum resistance." *Nature*, vol. 472, no. 7344, pp. 458–60, apr 2011. [Online]. Available: http://www.ncbi.nlm.nih.gov/pubmed/21525929

[89] J.-C. Park, S.-W. Cho, J.-H. Jeong, and G.-H. Jeong, "Infrared Spectroscopic Evidences for the Superconductivity of La2CuO4-related Compounds : A Superconductivity Probe," *Bulletin of the Korean Chemical Society*, vol. 21, no. 10, pp. 973–979, 2000.

[90] H. C. Bryant, N. L. Adolphi, D. L. Huber, D. L. Fegan, T. C. Monson, T. E. Tessier, and E. R. Flynn, "Magnetic Properties of Nanoparticles Useful for SQUID Relaxometry in Biomedical Applications," *Journal of Magnetism and Magnetic Materials*, vol. 323, no. 6, pp. 767–774, 2011.

[91] M. Nikolo, "Flux creep and activation energies at the grain boundaries of Y-Ba-Cu-O superconductors," *Physical Review B*, vol. 39, no. 10, pp. 6615–6618, 1989.

[92] K. H. Müller, S. J. Collocott, R. Driver, and N. Savvides, "AC susceptibility of granular superconductors," *Superconductor Science and Technology*, vol. 325, pp. 8–11, 1991. [Online]. Available: http://iopscience.iop.org/0953-2048/4/1S/094

[93] J. Jeong, N. Aetukuri, T. Graf, T. D. Schladt, M. G. Samant, and S. S. P. Parkin, "Suppression of Metal-Insulator Transition in VO2 by Electric Field-Induced Oxygen Vacancy Formation," *Science*, vol. 339, no. 6126, pp. 1402–1405, mar 2013. [Online]. Available: http://www.sciencemag.org/cgi/doi/10.1126/science.1230512

[94] T. D. Schladt, T. Graf, N. B. Aetukuri, M. Li, A. Fantini, X. Jiang, M. G. Samant, and S. S. P. Parkin, "Crystal-facet-dependent metallization in electrolyte-gated rutile TiO2 single crystals," *ACS Nano*, vol. 7, no. 9, pp. 8074–8081, 2013.

[95] M. Li, W. Han, X. Jiang, J. Jeong, M. G. Samant, and S. S. P. Parkin, "Suppression of ionic liquid gate-induced metallization of SrTiO 3(001) by oxygen," *Nano Letters*, vol. 13, no. 10, pp. 4675–4678, 2013.

[96] X. Leng, J. Garcia-Barriocanal, J. Kinney, B. Yang, Y. Lee, and A. M. Goldman, "Electrostatic tuning of the superconductor to insulator transition of YBa2Cu3O7-x using ionic liquids," *Journal of Physics: Conference Series*, vol. 449, p. 012009, 2013. [Online]. Available: http://stacks.iop.org/1742-6596/449/i=1/a=012009?key=crossref.edfc5596099abfd5ac66598e6cc9068d

[97] J. Walter, H. Wang, B. Luo, C. D. Frisbie, and C. Leighton, "Electrostatic versus Electrochemical Doping and Control of Ferromagnetism in Ion-Gel-Gated Ultrathin La0.5Sr0.5CoO3-d," *ACS Nano*, 2016. [Online]. Available: http://pubs.acs.org/doi/abs/10.1021/acsnano.6b03403

[98] A. Goldman, "Electrostatic Gating of Ultrathin Films," *Annual Review of Materials Research*, vol. 44, no. 1, pp. 45–63, 2014. [Online]. Available: http://www.annualreviews.org/doi/abs/10.1146/annurev-matsci-070813-113407

[99] R.-M. Wei, F. Cao, J. Li, L. Yang, Y. Han, X.-L. Zhang, Z. Zhang, X.-Y. Wang, and Y. Song, "Single-Chain Magnets Based on Octacyanotungstate with the Highest Energy Barriers for Cyanide Compounds," *Scientific Reports*, vol. 6, no. April, p. 24372, 2016. [Online]. Available: http://www.nature.com/articles/srep24372

[100] M. Mito, N. Shindo, T. Tajiri, H. Deguchi, S. Takagi, H. Miyasaka, M. Yamashita, R. Clérac, and C. Coulon, "Pressure effects on single chain magnets," *Journal of Magnetism and Magnetic Materials*, vol. 272-276, pp. 1118–1119, 2004.

[101] M. Mito, H. Deguchi, T. Tajiri, S. Takagi, M. Yamashita, and H. Miyasaka, "Effect of pressure on single-chain magnets with repeating units of the MnIII-NiII-MnIII trimer," *Physical Review B - Condensed Matter and Materials Physics*, vol. 72, no. 14, pp. 1–9, 2005.

[102] H. Miyasaka, M. Julve, M. Yamashita, and R. Clerac, "Slow dynamics of the magnetization in one-dimensional coordination polymers: Single-chain magnets," *Inorganic Chemistry*, vol. 48, no. 8, pp. 3420–3437, 2009.

[103] L. Bogani, A. Vindigni, R. Sessoli, and D. Gatteschi, "Single chain magnets: where to from here?" *Journal of Materials Chemistry*, vol. 18, no. 40, p. 4750, 2008.

[104] A. Caneschi, D. Gatteschi, N. Lalioti, C. Sangregorio, R. Sessoli, G. Venturi, A. Vindigni, A. Rettori, M. G. Pini, and M. A. Novak, "Cobalt(II)-Nitronyl Nitroxide Chains as Molecular Magnetic Nanowires," *Angewandte Chemie International Edition*, vol. 40, no. 9, pp. 1760–1763, may 2001.

[105] R. J. Glauber, "Time Dependent Statistics of the Ising Model," *Journal of Mathematical Physics*, vol. 4, no. 2, 1963.

[106] J. Boeckmann and C. Näther, "Solid-state transformation of [Co(NCS)2(pyridine)4] into [Co(NCS)2(pyridine)2]n: from CurieWeiss paramagnetism to single chain magnetic behaviour," *Dalton Transactions*, vol. 39, no. 45, p. 11019, 2010. [Online]. Available: http://xlink.rsc.org/?DOI=c0dt00904k

[107] J. A. Mydosh, *Spin glasses: An experimental introduction*. London: Taylor & Francis, 1993.

[108] M. Balanda, M. Rams, S. K. Nayak, Z. Tomkowicz, W. Haase, K. Tomala, and J. V. Yakhmi, "Slow magnetic relaxations in the anisotropic Heisenberg chain compound Mn(III) tetra(ortho-fluorophenyl)porphyrin-tetracyanoethylene," *Physical Review B - Condensed Matter and Materials Physics*, vol. 74, no. 22, pp. 1–9, 2006.

[109] G. Craig, "Personal Communication," 2016.

[110] W. Whitley, "Charge density waves and superconductivity in U6Fe," Ph.D. dissertation, The University of Edinburgh, 2015.

[111] G. H. Lander, E. S. Fisher, and S. D. Bader, "The solid-state properties of uranium. A historical perspective and review," *Advances in Physics*, vol. 43, no. 1, pp. 1–111, 1994. [Online]. Available: http://dx.doi.org/10.1080/00018739400101465

[112] K. N. Yang, M. B. Maple, L. E. Delong, J. G. Huber, and A. Junod, "Low-temperature heat-capacity study of the U6X (X=Mn, Fe, Co, Ni) compounds," *Physical Review B*, vol. 39, no. 1, pp. 151–166, 1989.

[113] B. D. White, J. D. Thompson, and M. B. Maple, "Unconventional superconductivity in heavy-fermion compounds," *Physica C: Superconductivity and its Applications*, vol. 514, pp. 246–278, 2015. [Online]. Available: http://dx.doi.org/10.1016/j.physc.2015.02.044

[114] C. W. Kimball, P. P. Vaishnava, A. Dwight, J. D. Jorgenson, and F. Y. Fradin, "Phonon Anomalies and Local Atomic Displacements in the Exchange-Enhanced Superconductor U6Fe," *Physical Review B*, vol. 32, no. 7, pp. 4419–4425, 1985.

[115] E. Yamamoto, M. Hedo, Y. Inada, T. Ishida, Y. Haga, and Y. Onuki, "Single Crystal Growth and the Upper Critical Field of the Superconductor U6Fe," *Journal of the Physical Society of Japan*, vol. 65, no. 4, pp. 1034–1037, 1996.

[116] N. R. Werthamer, E. Helfand, and P. C. Hohenberg, "Temperature and Purity Dependence of the Superconducting Critical Field, Hc2. III. Electron Spin and Spin-Orbit Effects," *Physical Review*, vol. 147, no. 1, pp. 295–302, 1966.

[117] L. De Long and K. Gschneidner Jr, "High Pressure Phase Stability of U6X (X = Mn, Fe, Co, Ni) Compounds," *Physica B*, vol. 163, pp. 158–162, 1990.

[118] J. Als-Nielsen and D. McMorrow., *Elements of Modern X-ray Physics*. John Wiley & Sons, 2011.

[119] L. E. De Long, G. W. Crabtree, L. N. Hall, H. Kierstead, H. Aoki, S. K. Dhar, K. a. Gschneidner, and A. Junod, "Normal and superconducting state properties of U6Fe at low temperatures and high magnetic fields," *Physica B+C*, vol. 135, no. 1, pp.

81–85, 1985. [Online]. Available: http://www.sciencedirect.com/science/article/pii/0378436385904413$\delimiter"026E30F$npapers2://publication/uuid/E4E2ED95-91DC-4F97-8707-27BE9D5EE7F6

[120] P. Fulde and R. A. Ferrell, "Superconductivity in a strong spin-exchange field," *Physical Review*, vol. 135, no. 3A, p. A550, 1964.

[121] A. I. Larkin and Y. N. Ovchinnikov, "Inhomogeneous State of Superconductors." *Soviet Physics JETP-USSR*, vol. 20, no. 3, p. 762, 1965.

[122] Y. Matsuda and H. Shimahara, "Fulde-Ferrell-Larkin-Ovchinnikov State in Heavy Fermion Superconductors," *Journal of the Physical Society of Japan*, vol. 76, no. 5, pp. 1–16, 2007.

[123] L. W. Gruenberg and L. Gunther, "Fulde-Ferrell Effect in Type-II Superconductors," *Physical Review Letters*, vol. 16, no. 22, pp. 996–998, 1966.

[124] A. Ardavan, S. Brown, S. Kagoshima, K. Kanoda, K. Kuroki, H. Mori, M. Ogata, S. Uji, and J. Wosnitza, "Recent topics of organic superconductors," *Journal of the Physical Society of Japan*, vol. 81, no. 1, pp. 1–27, 2012.

[125] C. Pfleiderer, "Superconducting phases of f-electron compounds," *Reviews of Modern Physics*, vol. 81, no. 4, pp. 1551–1624, 2009. [Online]. Available: http://link.aps.org/doi/10.1103/RevModPhys.81.1551

[126] G. Pasquini, P. Levy, L. Civale, G. Nieva, and H. Lanza, "Linear response in the AC susceptibility of vortices in YBa2Cu3O7 crystals with columnar defects," *Physica C: Superconductivity*, vol. 274, pp. 165–172, 1997.

[127] "Rox Ruthenium Oxide RTD Installation, Model RX-102B-CB," Lake Shore Cryotronics Inc., Tech. Rep., 2015. [Online]. Available: http://www.lakeshore.com/Documents/F010-07-00.pdf

[128] "Appendix D: Sensor Calibration Accuracies," Lake Shore Cryotronics Inc., Tech. Rep., 2015. [Online]. Available: http://www.lakeshore.com/Documents/LSTC{_}appendixD{_}l.pdf

[129] A. Campbell, "The response of pinned flux vortices to low-frequency fields," *Journal of Physics C: Solid State Physics*, vol. 2, p. 1492, 1969. [Online]. Available: http://iopscience.iop.org/0022-3719/2/8/318

[130] A. V. Silhanek, S. Raedts, M. J. Van Bael, and V. V. Moshchalkov, "Dynamic regimes in films with a periodic array of antidots," *European Physical Journal B*, vol. 37, no. 1, pp. 19–24, 2004.

Physics Procedia

Volume 75, 2015, Pages 252–258

20th International Conference on Magnetism

Pressure-Temperature Phase Diagram of Ionic Liquid Dielectric DEME-TFSI

Duncan M. McCann[1,4], Martin Misek[2,4], Konstantin V. Kamenev[3,4], and Andrew D. Huxley[1,4]

[1] School of Physics and Astronomy, University of Edinburgh, Edinburgh, United Kingdom
D.McCann@ed.ac.uk

[2] Institute of Physics v.v.i, Academy of Sciences of the Czech Republic, Prague, Czech Republic
Misek@fzu.cz

[3] School of Engineering, University of Edinburgh, Edinburgh, United Kingdom
K.Kamenev@ed.ac.uk

[4] Centre for Science at Extreme Conditions, University of Edinburgh, Edinburgh, United Kingdom
A.Huxley@ed.ac.uk

Abstract

Ionic liquids have proven highly effective as dielectrics in Electric Double Layer (EDL) devices for electrostatic doping in a range of materials. DEME-TFSI in particular is a commonly used dielectric due to its high ionic conductivity and low glass transition temperature of 182 K. Application of pressure provides a dual tuning parameter in tandem with the electric field yet progress is hampered by the lack of an accurate pressure-temperature phase diagram for DEME-TFSI. We present results on expansivity and leakage current measurements of the ionic liquid dielectric DEME-TFSI to provide a phase diagram mapping the glass transition temperature up to 0.6 GPa. This should allow the effective operation of EDL devices using DEME-TFSI under pressure.

Keywords: DEME-TFSI, ionic liquid, pressure, phase, glass transition

1 Introduction

Ionic liquids are highly polar binary salts with low melting temperatures that have gained much attention in recent years for their use in Electric Double Layer (EDL) devices. EDL devices provide a means to electrostatically dope various materials and continuously tune through their phase diagrams permitting a dramatic switching between material properties by applying potentials of only a few volts. Ionic liquids exhibit high dielectric constants and chemical compatibility with many materials compared to most electrolytes thus making them an ideal dielectric for EDL devices[1]. As such they have been shown to maximise the achievable carrier densities in EDL's[2] in order to induce metal-insulator transitions [3] as well as superconductivity in a range of materials[4, 5].

Selection and peer-review under responsibility of the Scientific Programme Committee of ICM 2015

doi:10.1016/j.phpro.2015.12.031

N,N-diethyl-N-methyl-N-(2-methoxyethyl)ammonium bis(trifl uoromethanesulfonyl)imide (DEME-TFSI) in particular is a commonly used ionic liquid dielectric for EDL devices due to its large electrochemical potential window and a low glass transition at 182 K[6, 7, 8] where the mobility of ions falls to zero[3]. No known crystal phase has been observed[6]. Tuning of material properties using an EDL device relies on ion mobility and thus it is important to ensure parameters are altered above any glass or solid phase transition.

Pressure is also a common tuning parameter for material properties and potentially could increase the versatility of EDL devices. To date there has been some research into the use of pressure with electrostatic doping[9] and on DEME-TFSI's structure[8] yet no definitive mapping of the glass transition shift. Effective function of EDL devices under pressure will rely on accurate tracking of the glass transition to ensure parameters are always altered whilst the dielectric is in its liquid state. In this paper we aim to present results on the mapping of this glass transition with pressure through measurements of the expansivity of DEME-TFSI along with the leakage current across it when used as a dielectric.

2 Experimental Details

Measurements were carried out by filling a standard piston cylinder pressure cell (maximum pressure 1.1 GPa) with the ionic liquid DEME-TFSI as the pressure medium. DEME-TFSI is dried prior to use under a vacuum line pressure of $\sim$5 x 10^{-3} mbar at $\sim$120°C for 24 hours to reduce water content and prevent electrolysis under voltage application[6, 7]. As ionic liquid dielectric properties cannot be measured by conventional means due to their high ionic conductivity[10] we instead opted to measure the expansivity of the liquid as it undergoes the glass transition and the leakage current between fixed plates immersed within it. Many materials upon undergoing a liquid-glass transition experience a sudden change in their expansivity[11] which should be detectable with a sensitive pressure gauge. A thermally cycled manganin gauge, primarily used to track the pressure[12], is employed in conjunction with a sensitive KYOWA KFL-02-120-C1-11 strain gauge in the piston cell as a means of detecting this change associated with the glass transition. Platinum plates of area 50 mm^2, separated $\sim$100 μm apart by insulating plastic spacers, were chosen for immersion in the ionic liquid in order to avoid electrochemical reaction on application of voltage. A constant 2 V are applied between the plates whilst the small leakage current through the ionic liquid is measured by a Keithley 6517A Electrometer. A low voltage must be applied in order to remain within the potential window for DEME-TFSI and prevent oxidation/reduction reactions[6, 7]. Measurements are taken at each applied pressure whilst the cell is cooled and warmed on a cold finger closed cycle cryostat.

3 Results & Discussion

3.1 Expansivity Measurements

The change in expansivity of DEME-TFSI is measured by monitoring the temperature dependent resistance of a manganin gauge and sensitive strain gauge immersed in the ionic liquid within the pressure cell. At ambient pressure a small discontinuity in the manganin gauges resistance is detected as it is cooled or warmed within the cryostat at 176.4 $\pm$ 2.0 K. Strain gauges are specially designed to measure the stress and strain of a material as it undergoes expansion or contraction with temperature change, as such it also exhibits a similar, but more

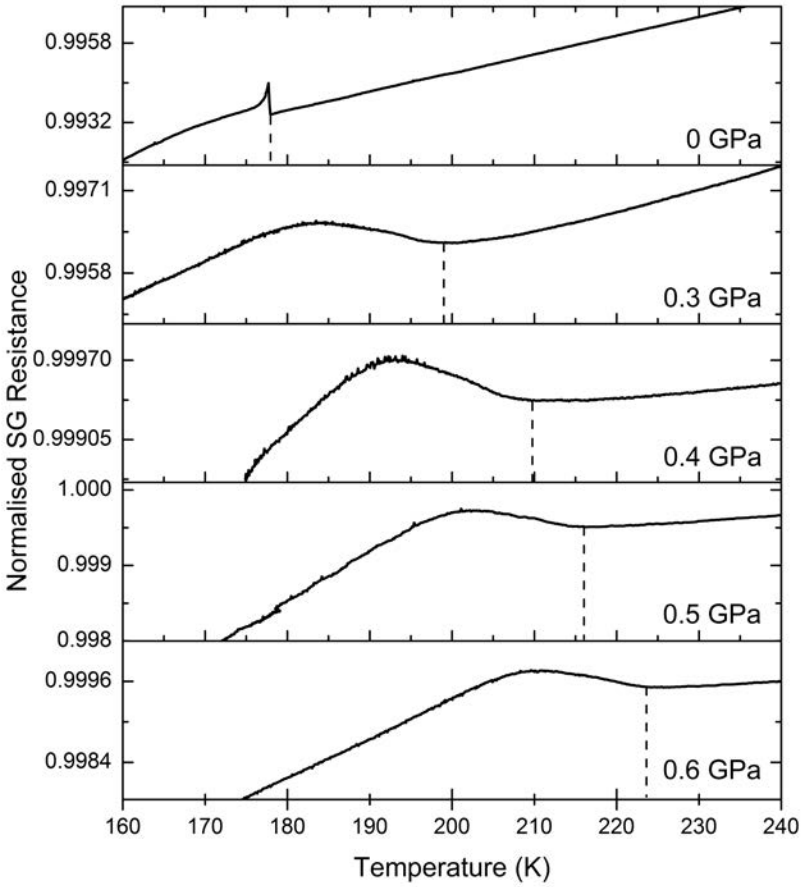

Figure 1: Temperature dependent normalised strain gauge resistance at various pressures. Dashed lines indicate proposed onset of glass transition in DEME-TFSI and approximate room temperature applied pressures are listed.

greatly pronounced, discontinuity at 179.0 ± 3.1 K visible in Figure 1. These values are approximately consistent with the observed glass transition temperature of DEME-TFSI at 182 K [6, 7, 8] indicating that these discontinuities are indeed associated with this phase change.

Further measurements are conducted at a range of pressures after the pressure cell has been sealed and loaded. The discontinuity previously seen in the manganin gauge became indistinguishable from noise at the following pressure steps and thus we were unable to determine the glass transition temperature using this gauge. However due to the sensitive nature of the strain gauge we were still able to observe and track the glass transition temperature which shows steady increase with pressure as can be seen in Figure 1. Interestingly under pressure the change in expansivity detected by the strain gauge is no longer a sharp discontinuity but rather a broad peak disrupting the approximate linearity of the resistance with temperature. Potentially this feature could be due to the pressure within the cell falling with temperature, as

is often seen with the slow contraction of any pressure medium, essentially resulting in the glass transition being shifted across a larger temperature regime thereby spreading out the sharp discontinuity. Another possibility is that upon transitioning into the glass phase the pressure application is no longer hydrostatic resulting in a pressure gradient across the DEME-TFSI. If large enough not all of the DEME-TFSI may remain in the glass phase until lower temperatures are reached thus resulting in a less defined transition zone. Regardless of the loss of the sharp discontinuity the onset of this broad peak is still indicative of a change in expansivity thus we take this to be our estimate for onset of the glass phase transition as shown by the dashed vertical lines in Figure 1.

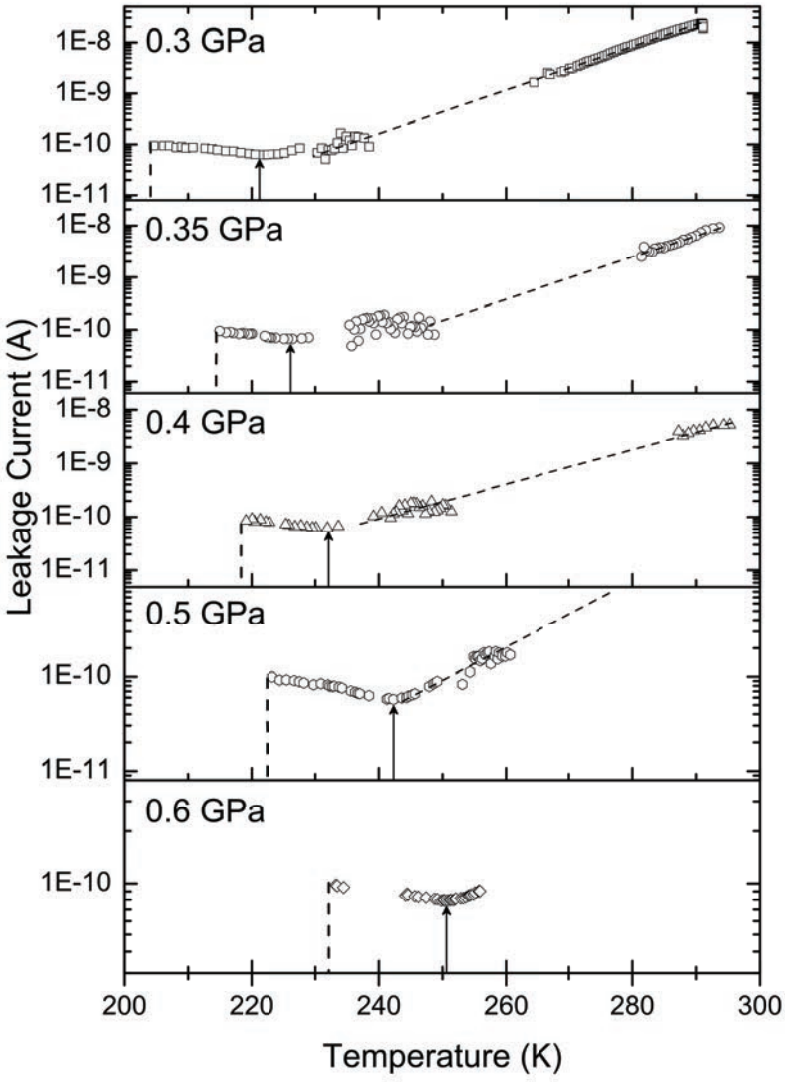

Figure 2: Leakage current across platinum plates immersed in DEME-TFSI at various pressures. Vertical dashed lines indicate proposed onset of glass transition, arrows the weak minimum for rubber phase extent and approximate room temperature applied pressures are listed.

3.2 Leakage Current Measurements

The ionic conductivity of DEME-TFSI quickly falls as it is cooled which can be observed by the rapidly decreasing leakage current between plates immersed within it[3]. As shown in Figure 2 at approximately 0.3 GPa of pressure we see just such an exponential decrease until it plateaus at a stable value. This plateau is consistent with previous measurements of the leakage current where DEME-TFSI experiences a rubber phase between its liquid-glass transition and ion mobility begins to slow[3]. There appears to be a weak minimum of the leakage current at the edge of this plateau, indicated by arrows in Figure 2, that could be taken to correspond to the limit of the rubber phase. At 204 K there is a sharp cutoff where it is believed the ion mobility suddenly slows to such an extent on approaching the glass phase that measurements exceed the limits of our instrumentation ($I < 1 \times 10^{-12}$ A) and as such we have taken this to be our measure of the glass transition.

Figure 2 illustrates how the cutoff, weak minimum and plateau region are all shifted to higher temperatures as the pressure is increased indicating the glass transition and rubber phase migration is consistent with the expansivity shifts observed in section 3.1. Dashed lines indicate extrapolation of stable high temperature data down to the plateau as measurements in this intermediate region were too erratic to provide meaningful data due to the temperature falling too quickly. Interestingly the leakage current in the rubber phase remains constant at approximately 1×10^{-10} A implying that ion mobility is independent of pressure.

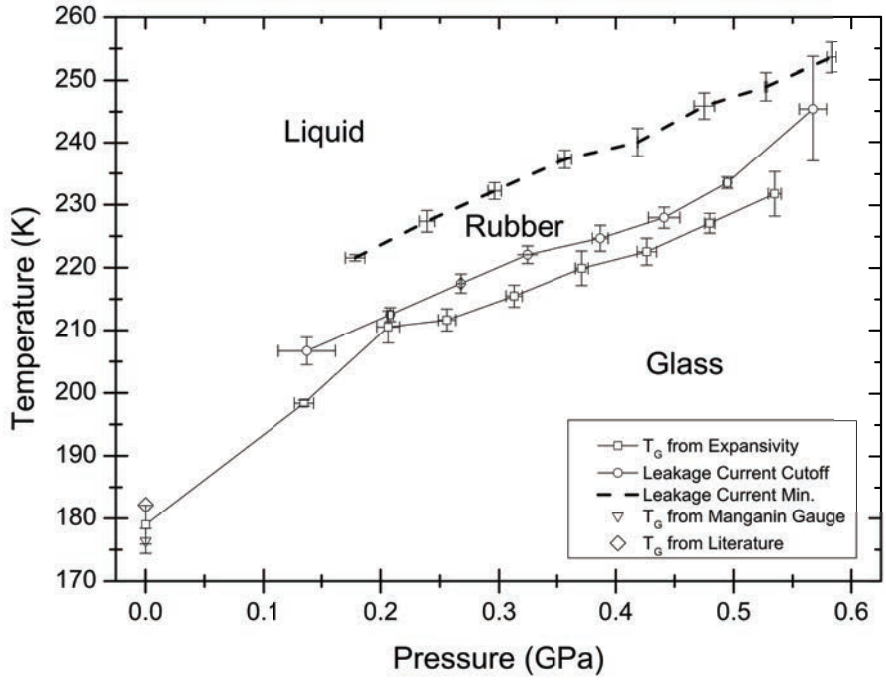

Figure 3: DEME-TFSI temperature-pressure phase diagram as determined from leakage current and expansivity measurements under pressure. Pressure at each temperature determined using manganin gauge[12]. Dashed line indicates proposed onset of rubber phase between liquid-glass transition. Included is ambient pressure glass transition from literature[6, 7].

3.3 Phase Diagram

Figure 3 shows the glass transition temperatures determined by averaging multiple thermal cycles of expansivity and leakage current measurements at each pressure. Rather than using room temperature applied pressures, as in Figures 1 & 2, values at each observed glass transition temperature were determined using the manganin gauge[12] to provide the most accurate pressure experienced by DEME-TFSI at this point.

The estimate of the glass transition temperature from leakage current measurements appears to be consistently higher than that determined from the strain gauge. In all likelihood this is due to the fact that ion mobility slows whilst DEME-TFSI is in the rubber phase[3]. Thus the expansivity measure from the strain gauge provides the most accurate estimate of the glass transition temperature whilst the leakage current cutoff helps indicate the lower regime of the rubber phase immediately above it rising in tandem with increased pressure.

Previous measurements of the leakage current in an EDL device have suggested that this rubber phase is present at room temperature for pressures in excess of 0.59 GPa[9]. Considering the weak minimum in our leakage current measurements to mark the extent of the rubber phase we have plotted this on our phase diagram and would estimate a value of around 255 K at 0.6 GPa, which is nearing room temperature.

4 Conclusions

Through expansivity and leakage current measurements we have mapped the glass transition and shift of the rubber phase of DEME-TFSI up to applied pressures of 0.6 GPa to create a pressure-temperature phase diagram. Effective application of EDL devices at ambient pressure generally requires change of bias at 40 - 60 K above the glass temperature to ensure ion mobility and a set wait time for equilibrium to be established[3]. Our data shows that this should be done at increasing temperature with pressure. We also note that the leakage current measured in the rubber phase is almost independent of pressure. Thus mobility of the ions appears to remain unchanged with pressure implying that the same wait time for equilibrium on change of bias at ambient pressure can be applied at other pressures.

5 Acknowledgements

We would like to acknowledge funding support from EPSRC grants EP/L015110, EP/J00099X and EP/I031014.

References

[1] Rajiv Misra, Mitchell McCarthy, and Arthur F. Hebard. Electric field gating with ionic liquids. *Applied Physics Letters*, 90(5):052905, 2007.

[2] Kosmas Prassides. Condensed matter physics: superconductivity at the double. *Nature nanotechnology*, 6(7):400–401, July 2011.

[3] Hongtao Yuan, Hidekazu Shimotani, Atsushi Tsukazaki, Akira Ohtomo, Masashi Kawasaki, and Yoshihiro Iwasa. High-Density Carrier Accumulation in ZnO Field-Effect Transistors Gated by Electric Double Layers of Ionic Liquids. *Advanced Functional Materials*, 19(7):1046–1053, April 2009.

[4] J T Ye, S Inoue, K Kobayashi, Y Kasahara, H T Yuan, H Shimotani, and Y Iwasa. Liquid-gated interface superconductivity on an atomically flat film. *Nature materials*, 9(2):125–128, February 2010.

[5] K Ueno, S Nakamura, H Shimotani, H T Yuan, N Kimura, T Nojima, H Aoki, Y Iwasa, and M Kawasaki. Discovery of superconductivity in KTaO by electrostatic carrier doping. *Nature nanotechnology*, 6(7):408–412, July 2011.

[6] Takaya Sato, Gen Masuda, and Kentaro Takagi. Electrochemical properties of novel ionic liquids for electric double layer capacitor applications. *Electrochimica Acta*, 49(21):3603–3611, September 2004.

[7] Takaya Sato, Gen Masuda, and Kentaro Takagi. Corrigendum to "Electrochemical properties of novel ionic liquids for electric double layer capacitor applications" [Electrochim. Acta 49 (2004) 3603-3611] (DOI:10.1016/j.electacta.2004.03.030). *Electrochimica Acta*, 53(14):4934–4935, 2008.

[8] Yukihiro Yoshimura, Takahiro Takekiyo, Yusuke Imai, and Hiroshi Abe. Pressure-Induced Spectral Changes of Room-Temperature Ionic Liquid , N,N-Diethyl-N-methyl-N-(2-methoxyethyl) ammonium Bis(trifluoromethylsulfonyl)imide, [DEME][TFSI]. *Journal of Physical Chemistry C*, 116:2097–2101, 2012.

[9] Wu Shi, Jianting Ye, Joseph G. Checkelsky, Chieko Terakura, and Yoshihiro Iwasa. Transport Properties of Polymer Semiconductor Controlled by Ionic Liquid as a Gate Dielectric and a Pressure Medium. *Advanced Functional Materials*, 24(14):2005–2012, November 2014.

[10] Ingo Krossing, John M Slattery, Corinne Daguenet, Paul J Dyson, Alla Oleinikova, and Hermann Weingärtner. Why are ionic liquids liquid? A simple explanation based on lattice and solvation energies. *Journal of the American Chemical Society*, 128(41):13427–34, October 2006.

[11] Jeppe C. Dyre. Colloquium: The glass transition and elastic models of glass-forming liquids. *Reviews of Modern Physics*, 78(3):953–972, 2006.

[12] L H Dmowski and E Litwin-Staszewska. The variation of the pressure coefficient of manganin sensors at low temperatures. *Measurement Science and Technology*, 10(5):343–347, 1999.